CHARACTERISATION OF THE PERFORMANCE OF AN ABSORBABLE MAGNESIUM STENT BY EXPERIMENTAL AND NUMERICAL ANALYSIS

A thesis submitted for the award of PhD

Emmet Galvin, BEng MSc

Supervisors:

Dr. Bryan MacDonald

Dr. Caítriona Lally

School of Mechanical and Manufacturing Engineering

Dublin City University

September, 2014

Declaration

I hereby certify that this material, which I now submit for assessment on the programme of study leading to the award of Doctor of Philosophy (PhD) is entirely my own work, that I have exercised reasonable care to ensure that the work is original, and does not to the best of my knowledge breach any law of copyright, and has not been taken from the work of others save and to the extent that such work has been cited and acknowledged within the text of my work.

Signed: _____

Student ID No.: 98573900

Date: 18th September, 2014

Acknowledgements

I would like to thank my supervisors Dr. Bryan MacDonald and Dr. Tríona Lally for all their guidance and support throughout the project. This research could not have been achieved without the help of Christy Cummins at Vasorum Ltd. I would also like to thank Liam, Jim, Chris, Michael, and Keith for their technical support. I would especially like to thank my family and friends for their support and encouragement.

Publications and Presentations Resulting from this Study

Papers

Galvin, E., Cummins, C., Yoshihara, S., MacDonald, B., Lally, C. 2014. Experimental testing of an absorbable magnesium stent demonstrates the critical influence of deployment strain on corrosion behaviour. Journal of the Mechanical Behaviour of Biomedical Materials, In Review.

Galvin, E., Morshed, M.M., Cummins, C., Daniels, S., Lally, C., MacDonald, B.J., 2013. Surface Modification of Absorbable Magnesium Stents by Reactive Ion Etching. Journal of Plasma Chemistry and Processing. 33(6), 1137-1152

Conferences and Abstracts

Galvin E., Cummins, C., Colombo, A., Lally, C., MacDonald, B.J., "In Vitro Corrosion Testing of Absorbable Magnesium Stents", Proceedings of the 28th International Manufacturing Conference, Dublin City University, September 2011.

Galvin, E., Cummins, C, Coleman, J., Mathews, D., Colombo, A., Lally, C., MacDonald, B.J., "An Experimental and Numerical Analysis of a Bioabsorbable Magnesium Alloy Cardiovascular Stent", Proceedings of the 26th International Manufacturing Conference, Trinity College Dublin, September 2009.

Galvin, E., MacDonald, B.J., "Explicit & Implicit Finite Element Analysis of a Bioabsorbable Magnesium Alloy Cardiovascular Stent", Proceedings of the Northern Ireland Biomedical Engineering Society Spring Conference, April 2009.

Galvin, E., MacDonald, B.J., "Experimental and Numerical Analysis of a Bioabsorbable Magnesium Alloy Cardiovascular Stent", Bioengineering In Ireland 15 Conference, Castletroy Park Hotel, Limerick, January 2009.

Galvin, E., MacDonald, B.J., "Finite Element Simulation of the Deployment of a Magnesium Cardiovascular Stent", Proceedings of the 25th International Manufacturing Conference, Dublin Institute of Technology, September 2008.

List of Figures

v

List of Tables

Nomenclature

General

AFM   Atomic force microscopy

BAS   Bioabsorbable stent

BMS   Bare-metal stent

CABG   Coronary artery bypass graft

CAD   Coronary artery disease

CDM   Continuum damage modelling

CTO   Chronic total occlusion

DB   Dogboning

DES   Drug-eluting stent

EC   Endothelial cell

EDX   Energy dispersive x-ray spectrometry

ELR   Elastic longitudinal recoil

ERR   Elastic radial recoil

FE/FEM   Finite element/Finite element method

FS   Foreshortening

IH   Intimal hyperplasia

ISR   In-stent restenosis

MCA   Mock coronary artery

MI   Myocardial infarction

PCI   Percutaneous coronary intervention

PS   Plastic strain

PTCA   Percutaneous transluminal coronary angioplasty

RE   Rare-earth

RIE   Reactive ion etching

SBF   Simulated body fluid

SEM   Scanning electron microscope

SER   Stent expansion ratio

SMC   Smooth muscle cell

ST/LST   Stent thrombosis/Late stent thrombosis

TVR   Target vessel revascularisation

Material Properties

		Unit
E	Young's modulus	GPa
UTS	Ultimate tensile strength	MPa
ε_f	Failure strain	-
ε_u	Strain at UTS	-
σ_y	Yield stress (0.2% offset)	MPa

Corrosion Modelling

		Unit
δ_U	Material characteristic length	mm
κ_e	Element exposure parameter	-
D	Damage parameter	-
k_u	Corrosion kinetic parameter	h^{-1}
L_e	FE characteristic length	mm
t	Simulation time	h
t_{max}	Maximum solution time	h
Δ_t	Time-step	h
ε_{p1}	First principal plastic strain	-
φ_e	Plastic strain parameter	-

Contents

Abstract

Characterisation of the Performance of an Absorbable Magnesium Stent by Experimental and Numerical Analysis

Emmet Galvin

Magnesium stents are a promising candidate in the emerging field of bioabsorbable stents and could obviate many of the limitations of current permanent stent platforms such as stent thrombosis and in-stent restenosis. In this study, viable magnesium stents were manufactured from WE43 magnesium alloy precursor tubes by a combination of laser cutting and chemical and plasma-based surface treatments. The mechanical and corrosion performance of the stent was elucidated via experiments. It was shown that the plastic strain that is induced in the stent struts during the deployment procedure has a critical influence in directing both the kinetics and the nature of subsequent corrosion processes in the alloy. The deployment and scaffolding characteristics of the stent were determined and contrasted with those of a commercial stainless steel stent. The magnesium stent was shown to support significantly higher levels of cyclic strain amplitude which plays a crucial role in reducing in-stent restenosis. This study provided new insights into the performance of a current magnesium stent design and material and demonstrated the influence of deployment induced corrosion on the long-term scaffolding ability of the stent. A finite element based phenomenological corrosion model was developed and calibrated based on the results of the corrosion experiments. A plastic strain parameter was introduced in the modelling framework to account for the effects of plastic strain on corrosion behaviour. The model was found to be capable of predicting the experimentally observed mass loss profile and the temporal corrosion-induced reduction in the radial stiffness of the stent.

1. Introduction

1.1   Coronary Artery Disease and Stenting

Coronary artery disease (CAD) is the largest cause of mortality in the western world and is responsible for over seven million deaths worldwide each year (Go et al., 2013). The pathogenesis of CAD involves the formation of stenotic lesions (plaque) in the vessel walls leading to narrowing and hardening of the coronary arteries (Yutani et al., 1999). These lesions may decrease the lumen of the artery and the resulting restriction in blood supply (ischemia) can lead to myocardial infarction (MI).

The treatment of CAD often involves the deployment of an endovascular stent at the stenosis in order to restore patency and prevent arterial recoil (Lally et al., 2006). However, stenting inflicts injury in the intimal and medial layer of the arterial wall which can induce a partial re-blocking of the artery known as restenosis (Scott, 2006). In-stent restenosis (ISR) results in the formation of intimal hyperplasia (IH) around the stent struts and represents a major limitation to the success of current stent procedures (Dangas et al., 2010). Bare-metal stents (BMS), which have typically been produced from corrosion-resistant materials such as stainless steel (316L) and cobalt chromium, are associated with complications such as elevated rates of ISR (~25%) and late stent thrombosis (LST) (<1%) (Kandzari et al., 2013; Stone et al., 2004).

In order to overcome these limitations, drug-eluting stents (DES) were developed. DES normally consist of a BMS platform with a drug-eluting coating that is intended to reduce IH (Gogas et al., 2014). Although DES have demonstrated lower rates of ISR (~3%) and target vessel revascularisation (TVR) (<10%) compared to BMS, stent thrombosis (ST) (<1%) and ISR remain a significant limitation (Dangas et al., 2013; Kandzari et al., 2013). Permanent BMS and DES have other major limitations such as restrictions to non-invasive imaging and future

revascularisation procedures, long term disruption of native haemodynamics and vasomotor function, chronic inflammation and delayed endothelialisation (Sammel et al., 2013). DES patients require longer dual antiplatelet therapy (DAPT) courses (~3 months) compared to BMS (~1 month) in order to minimise the risk of LST (Kim et al., 2009; Nishinari et al., 2013). Variations in ST, TVR and ISR outcomes have been observed among existing stent platforms but the optimum treatment strategy after stenting has yet to be determined (Dangas et al., 2010; Hoffmann et al., 2004). Hence, a new generation of bioabsorbable stents (BAS), which are gradually absorbed in the body, is attracting significant interest (Gogas et al., 2012; Haude et al., 2013; Nishio et al., 2012; Zhang et al., 2013).

1.2   Bioabsorbable Stents

There are a number of limitations associated with current BAS including relatively large strut thicknesses (~150 µm) and crossing profiles (~1.4 mm) (Gogas et al., 2014), limited extensibility and a higher risk of strut fracture (Zhang et al., 2013). Several polymer BAS have been proposed (Gogas et al., 2012; Nishio et al., 2012) but they have yet to achieve the mechanical and surface properties of current BMS and DES (Jabara et al., 2009). Other concerns with polymers include toxicity and endarteritis (Palmerini et al., 2014). Compared to polymers, metals generally have superior mechanical properties for coronary stents. The potential of iron (Moravej et al., 2010a, 2010b; Peuster et al., 2006, 2001) and iron-manganese alloys (Hermawan et al., 2010a, 2008) has been studied, though the corrosion rate of iron appears too slow for coronary BAS (Peuster et al., 2006, 2001) and unwanted degradation products are retained in the arterial wall (Pierson et al., 2011).

Recently, absorbable magnesium stents based on the WE43 alloy have shown promise in clinical trials (Erbel et al., 2007; Haude et al., 2013) and, could potentially obviate many of the limitations of traditional permanent stents. However,

limitations associated with current magnesium stents include relatively high rates of late lumen loss due to excessive IH formation and premature loss of scaffolding (Erbel et al., 2007; Haude et al., 2013). Accordingly, the widespread adoption of magnesium stents depends on further developments in the technology such as characterisation and optimisation of materials and stent designs, and improved understanding of the adsorption of magnesium in vascular tissues (Hermawan et al., 2010; Kitabata et al., 2014; Zhang et al., 2013).

To date, stents based on WE43 derivatives represent the only magnesium platform to go through clinical trials for coronary stents (Haude et al. 2013; Erbel et al. 2007). Despite this, only a limited amount of data regarding their mechanical and corrosion performance characteristics has been reported in animal (Di Mario et al., 2004; Heublein et al., 2003; Waksman et al., 2006) and clinical (Bosiers et al., 2009; Erbel et al., 2007; Haude et al., 2013) trials. There is little information available in the literature with regard to the manufacture of magnesium stents (Demir et al., 2012; Di Mario et al., 2004; Hassel et al., 2006; Wu et al., 2012). Fibre laser cutting and surface treatment of balloon-expandable AZ31 stents has been described (Demir et al., 2012; Wu et al., 2012); though no such study has been reported for WE43. Also, few studies have reported mechanical and corrosion performance data for WE43 precursor tubes (Pachla et al., 2012; Witte et al., 2008).

When investigating the performance of metallic stents, it is desirable to conduct testing on the stent or on a sample of the precursor tube in the final form and finish, due to the influence of materials processing, size effects and surface treatments on mechanical and corrosion behaviour (Connolley et al., 2005; Jain et al., 2008). It is noted that few experimental studies have been reported to this end for magnesium stents, with the study of Wu et al. (Wu et al., 2012), on an AZ31 stent, being the most pertinent to date. Many of the existing studies employ specimens that were prepared using materials processing and surface treatments

4

that differed from those of coronary stents (Bowen et al., 2013; Coy et al., 2010; Grogan et al., 2011; Kannan et al., 2008; Zhang et al., 2010). Furthermore, while a number of studies have examined the effects of mechanical loading on the corrosion of magnesium for near-constant (Grogan et al., 2011) and non-constant (Kannan et al., 2008; Winzer et al., 2008) loads, the influence of the loading that is induced during stent deployment on corrosion behaviour has not been extensively studied.

A number of experimental studies have provided correlations between the magnitude of specimen stress and corrosion behaviour in magnesium alloys (Dietzel et al., 2010; Kannan et al., 2008; Winzer et al., 2008). However, plastic strain, and the accompanying deformation-induced changes in electrochemical behaviour have been shown to play a crucial role in the micro-galvanic corrosion processes that are observed in magnesium alloys (Snir et al., 2012; Wittke et al., 2014). Since the stent deployment procedure is known to induce large plastic strain in the struts (Murphy et al., 2003), it is hypothesised in this work that deployment-induced plastic strain plays a critical role in directing subsequent corrosion phenomena in magnesium stents and thus effects the scaffolding ability of these devices in the long-term.

In addition to experimental corrosion testing, computational modelling of the corrosion process can provide important insights into the fundamental corrosion processes that lead to the degradation of magnesium stents. To date, only a small number of corrosion models have been developed for absorbable metallic stents, which were based on the finite element method (FEM) and used either a continuum damage mechanics (CDM) approach (Gastaldi et al., 2011; Grogan et al., 2011) or adaptive meshing (Grogan et al., 2014a). Typically, these models adopted a stress-mediated approach to simulate the corrosion of magnesium stent geometries (Gastaldi et al., 2011; Grogan et al., 2014a). However, in this work, a plastic strain mediated phenomenological corrosion model of the corrosion behaviour of a magnesium alloy stent was developed to facilitate prediction of stent behaviour.

While previous studies involved large and computationally-expensive FE models that required high-performance computing capabilities (Gastaldi et al., 2011; Grogan et al., 2014a), the focus of this work was the development of a compact and computationally-efficient corrosion model that facilitated virtual testing of magnesium stents and other implants on a standard desktop computer. Such models provide short solution times which are especially useful in the preliminary stages of stent design where many cycles of design iteration are necessary (Xia et al., 2007). These models may find utility in the design of stents through device evaluation simulations and the optimisation of device geometries for prolonging structural integrity during the absorption process.

1.3   Objectives of this Study

The key aim of this study was the determination of the mechanical and corrosion performance of a WE43 alloy absorbable magnesium stent using a combination of experimental and numerical analysis. The mechanical performance of the stent was determined and compared to that of a commercial 316L stent in terms of a range of deployment, radial stiffness and cyclic strain amplitude metrics. The influence of deployment-induced plastic strain on the subsequent corrosion behaviour of the stent was elucidated. The corrosion rates, the dominant corrosion processes and the temporal corrosion-induced reduction in the mechanical integrity of the stent were revealed. Since the specimens were laser cut from precursor tubes and were prepared using surface treatments suited to processing magnesium stents, it was believed that such an approach provided a more accurate characterisation of the mechanical and corrosion behaviour of the stent than previous experimental studies on magnesium test specimens with processing histories, surface treatments and loading conditions that differed from those of coronary stents.

A finite element (FE) based plastic strain mediated phenomenological

corrosion model, which was capable of modelling the corrosion of a three-dimensional (3-D) stent structure, was developed in order to assess the performance of a corroding magnesium stent. The development of such a model, which was calibrated based on the results of corrosion experiments and solved on a standard desktop computer by means of a computationally-efficient algorithm, provided a fast, convenient and inexpensive preclinical tool for testing the design of stents and other absorbable metallic implants.

In order to achieve the aforementioned goals, the following tasks first needed to be completed (see Figure 1.1);

- A suitable processing route had to be identified by which viable stents could be manufactured from precursor tubes of the WE43 alloy.

- A range of experiments had to be developed so that the mechanical and corrosion performance of stents and other specimens could be determined.

- A corrosion algorithm had to be developed in a suitable computer language for use in a commercial implicit FE software package.
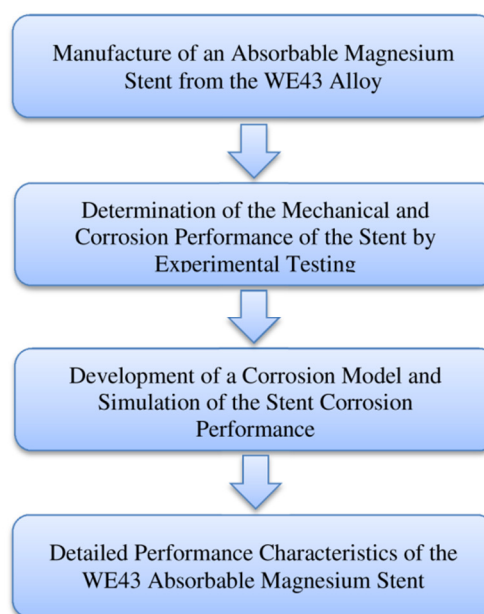
Figure 1.1 Flow chart of the key project steps

2. Literature Review

2.1 Anatomy, Physiology and Biomechanics of Coronary Arteries

The coronary circulation supplies oxygenated blood to the myocardium with the majority of flow occurring in diastole, when the heart is relaxed (Nichols et al., 2005). The left and right coronary arteries (LCA and RCA) originate at the base of the ascending aorta, at the aortic sinuses, where blood pressure is at its greatest in the systemic circuit (Martini, 2006), as shown in Figure 2.1(a).
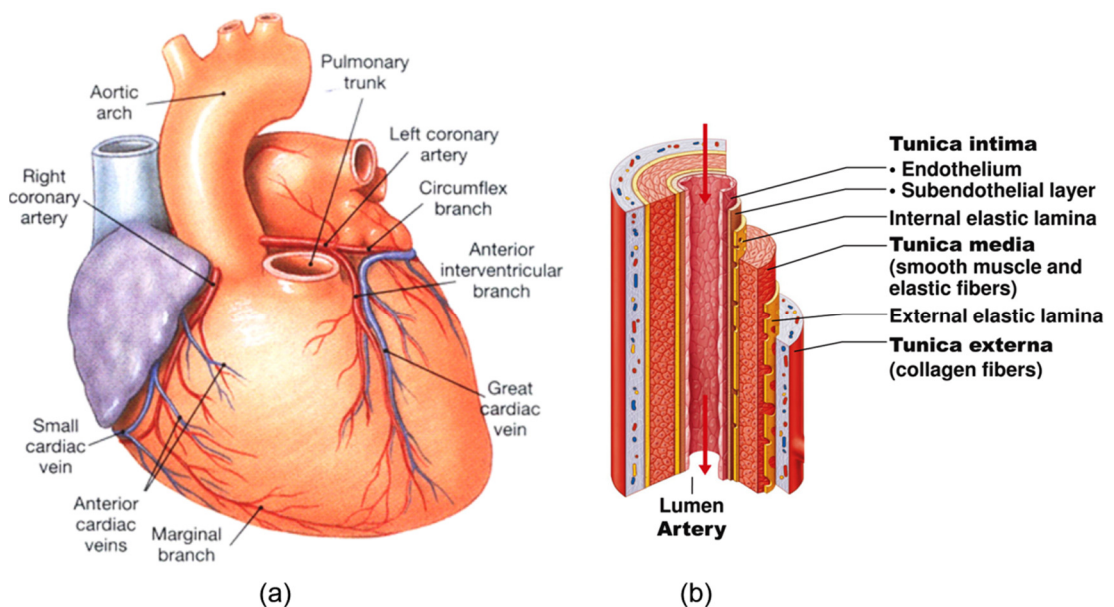
Figure 2.1 (a) Anterior view of the heart showing the coronary circulation (b) schematic of the layers of a coronary artery

The RCA supplies blood mainly to the right atrium, portions of both ventricles and the conducting system of the heart including the sinoatrial and atrioventricular nodes. The LCA supplies the left ventricle, left atrium and interventricular septum. Towards the anterior surface of the heart it gives rise to a circumflex branch (LCX) and the left anterior descending (LAD) artery. The LCX curves around the coronary sulcus where it finally joins small branches of the RCA. The much larger LAD swings

around the pulmonary trunk and runs along the surface within the interventricular sulcus. The LAD supplies small tributaries continuous with those of the posterior descending artery through interconnections known as arterial anastomoses (Martini, 2006). LAD arteries are of central importance in CAD pathophysiology as ISR after stenting is most common in the LAD (Holzapfel et al., 2005).

The wall of a healthy coronary artery consists of three distinct concentric layers; intima, media, and adventitia, as shown in Figure 2.1(b). The intima is the innermost layer and consists of a single layer of endothelial cells (ECs) that grow on the internal elastic lamina (Humphrey, 2002). ECs align with the direction of blood flow and act as a selective barrier between blood constituents and the extravascular space while also preventing thrombosis (Hunt et al., 2002). The intima may also contain a thin layer of sub-endothelial connective tissue and axially-orientated smooth muscle cells (SMCs) (Humphrey, 2002). The media is the thickest and most significant layer in terms of mechanical compliance at physiological pressures and consists of SMCs in an extracellular network of elastin fibres and collagen fibrils as well as an aqueous ground substance (Holzapfel et al., 2000). The media is separated from the adventitia by the external elastic lamina. The adventitia is the outermost layer and consists largely of thick bundles of collagen fibrils with admixed elastin, fibroblasts, and nerves (and in some cases, a network of blood vessels called the *vasa vasorum*) (Holzapfel and Ogden, 2006).

Coronary arteries display both active and passive mechanical behaviour (Fung, 1993). Active behaviour is determined by the contraction of SMCs that are arranged spirally around the vessel wall allowing them to function as control points for blood distribution. The highly non-linear passive mechanical properties of the multi-layered artery are dependent on many factors such as the relative amounts of elastin and collagen present, the age of the artery and the level of disease present (Holzapfel et al., 2005).

2.2 Coronary Artery Disease

CAD (also known as coronary atherosclerosis or ischemic heart disease) is a condition involving the accumulation of plaque (an atheroma or lesion) in the walls of the coronary circulation leading to narrowing and hardening of the arteries (Holzapfel and Ogden, 2006), as shown in Figure 2.2. Low density lipoprotein (LDL) particles accumulate in the intima causing ECs to produce adhesion molecules that latch onto blood monocytes. The monocytes mature into active macrophages which ingest modified lipoprotein particles, ending up as fat-laden foam cells. SMCs proliferate and migrate to the intima promoting extracellular matrix accumulation in the growing atherosclerotic plaque (Zohdi et al., 2004). As the atheroma develops it increases in volume and may occlude the lumen of the artery thus restricting the blood supply to the myocardium leading to myocardial ischaemia. The mismatch in the mechanical properties of the vessel wall and the stiffer atheroma may also lead to rupture or detachment of the atheroma, creating a downstream clot (embolism) in the blood flow (Holzapfel et al., 2004).

Risk factors for CAD include hyperlipidaemia, tobacco smoking, obesity, diabetes mellitus, hypertension, psychosocial and dietary factors, physical inactivity and a genetic disposition (Yusuf et al., 2004). The risk of CAD increases progressively with adult age and with the level of systolic blood pressures (Lewington et al., 2003). CAD may be treated by a number of interventional techniques including coronary artery bypass grafting (CABG), atherectomy, laser vaporisation techniques, percutaneous transluminal coronary angioplasty (PTCA) and stent deployment (Topol, 2008). CABG involves diverting the blocked blood flow through an alternative path using a vein or artery from elsewhere in the body or a prosthetic vessel in order to restore blood flow to the effected cardiac muscle. Specific advantages of CABG include the ability to revascularise chronic total occlusions (CTOs) and the ability to treat anatomic subsets that are not

approachable with stents (Topol, 2008). However, the CABG procedure is highly-invasive and requires a considerable recovery period. It normally requires the heart to be stopped and therefore a cardiopulmonary bypass module is required. Although CABG has a low death rate it has associated complications and so is more commonly used for high-grade stenosis or occlusion (Drenth et al., 2002).
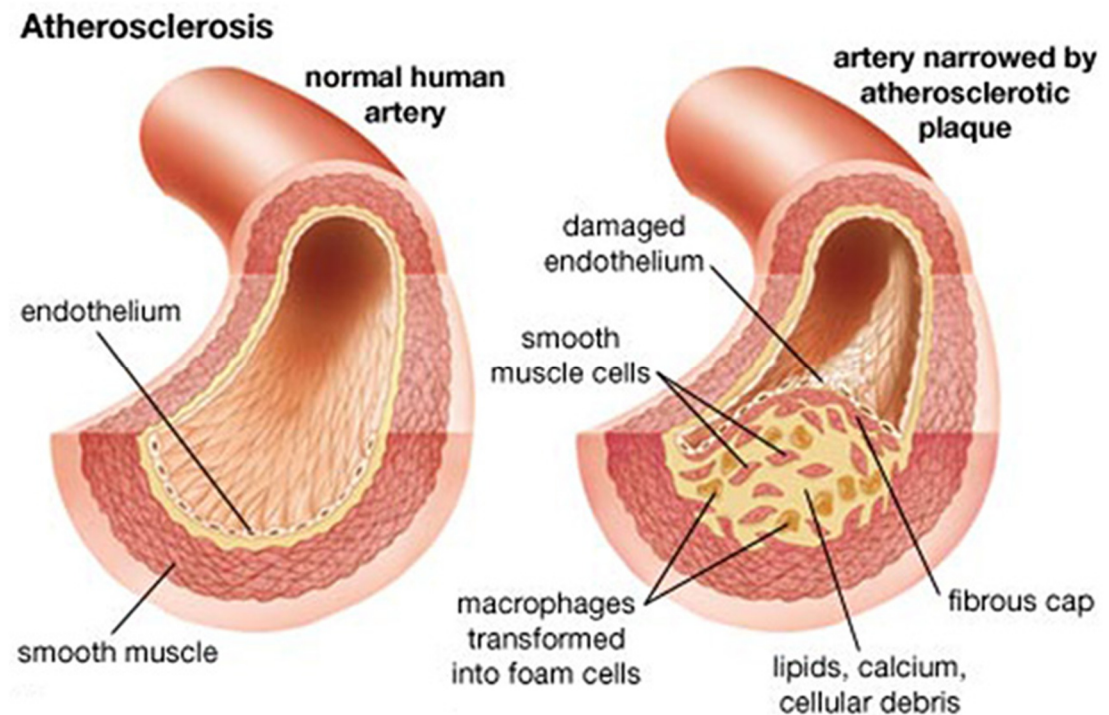
Figure 2.2 Schematic representation of the process of atherosclerosis

PTCA, also known as balloon angioplasty, involves making a small incision in the femoral artery and guiding a balloon catheter to the blockage site in the coronary arteries (Agema et al., 2004). The balloon is expanded thereby pushing the atheromatous plaque into the arterial wall, thus restoring vessel patency. Although PTCA is non-invasive, it is associated with high rates of restenosis (30-60%) due to elastic recoil of the arterial wall and/or the formation of IH (Mercado et al., 2001; Topol, 2008). Therefore, PTCA is often combined with stent implantation in order to reduce the incidence of restenosis (Serruys et al., 1994; Svilaas et al., 2007).

2.2.1 Restenosis

Restenosis is the re-blocking of a stented arterial segment causing a reduction in luminal size and a restriction in blood flow. It primarily involves the formation of a neointimal layer that occurs as a result of an exaggerated healing response prompted by vascular injury (EC denudation, vessel wall stretching and sometimes plaque rupture) consequent to high pressure (10-20 bar) balloon expanded stent implantation (Kraitzer et al., 2008), as shown in Figure 2.3.
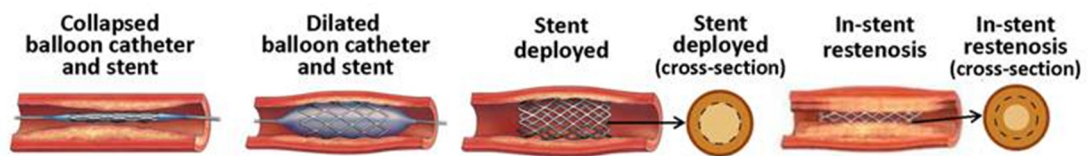
Figure 2.3 Stent restenosis: the re-blockage of a stented artery owing primarily to the formation of neointimal hyperplasia

The biological response to stenting may consists of four phases (Kraitzer et al., 2008; Welt and Rogers, 2002), as shown in Figure 2.4.
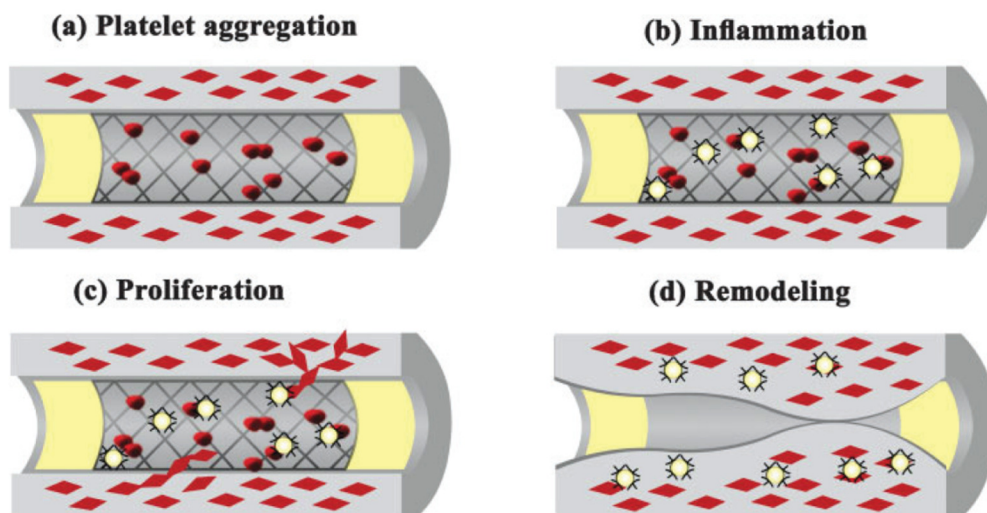
Figure 2.4 Schematic representation of the restenosis process after stent implantation

a) Platelet Aggregation: The arterial injury that occurs during the stenting

procedure (endothelial denudation and medial dissection) causes platelet aggregation and activation, thus initiating an inflammatory cascade and releasing adhesion molecules that trigger thrombus formation. The thrombosis that develops may be a major cause of vessel re-occlusion in the first month after stenting (Edelman and Rogers 1998).

b) Inflammatory phase: Over days to weeks, a variety of white cells may gather at the injury site, secrete factors and influence the healing tissue. The inflammatory phase may persist for months.

c) Proliferation phase: Between one and three months after stent implantation, SMC migration and proliferation and IH formation is the key mechanism of restenosis (Topol, 2008). SMCs migrate from the vessel media (and possibly adventitia) through the fracture of the internal elastic membrane to the intima where they may continue to proliferate and synthesise extra-cellular matrix (ECM); the major component of the restenotic lesion.

d) Late remodelling phase: involves alterations in vessel wall geometry through redistribution of cells through processes such as selective cell proliferation/apoptosis, or matrix synthesis/degradation (Hunt et al., 2002) in order to adapt to the new strain environment imposed by the stent. Initial deformation consists of elastic recoil following balloon deflation. Later, geometric remodelling occurs as the artery shrinks, owing to collagen deposition and fibrosis. Although remodelling in a BMS and DES stented vessel is relatively small, the arterial wall may be squeezed through the stent strut gaps from without. The artery opposes the strain imposed by the stent struts through increased collagen deposition, marked destruction of elastin, and persistent inflammation (Edelman and Rogers 1998). As the amount of scar develops, blood flow is gradually reduced.

The classic binary definition of restenosis is an angiographically-measured obstruction of 50% diameter stenosis or more at the site of a previously treated coronary vessel (Briguori et al., 2000). When the lumen diameter is reduced to 50% or less, coronary flow reserves become impeded. Late loss is a continuous angiographic measure of lumen deterioration and is usually calculated by subtracting the minimum lumen diameter (MLD) at follow-up from the post-procedural MLD (irrespective of the locations of MLD measurements). Late loss measurements in stented segments offer a surrogate marker of IH. Target vessel revascularisation (TVR) is defined as any repeat percutaneous coronary intervention (PCI) of the treated coronary segment or CABG of the target vessel. ISR can be characterised as focal (≤10mm long), diffuse (>10mm), proliferative (>10mm and extending outside the stent) or total occlusion (Dangas et al., 2010).

The nature of restenosis appears to be related to the stent platform used (Sangiorgi et al., 2007). Restenosis with sirolimus-eluting stents is mostly focal (>90%) and located at the stent edges, whereas diffuse or total occlusion accounts for about 50% of restenosis cases after implantation of polymer-coated paclitaxel-eluting stents (Topol, 2008). Studies have shown that many factors associated with the stent deployment procedure also contribute to restenosis outcomes, such as procedural complications (Castagna et al., 2001), stent-induced injury or stretch which is a function of maximum balloon pressure (Arakawa et al., 1998; Hoffmann et al., 2004; Schwartz et al., 1992) and the stent-to-artery ratio. Stent design variables also influence the biologic response to stent implantation (Hara et al., 2006), such as the number of struts (Briguori et al. 2002), strut thickness and profile (ideally <75 μm) (Kastrati et al., 2001) (Palmaz, Benson et al. 1999), the release of toxic metals (e.g. Ni, Mo) (Köster et al. 2000; Saito et al. 2009) and haemodynamic factors (Duraiswamy et al., 2007). The largest alteration of shear stress in the blood occurs at the entry and exit segment of stents where IH is often focused (LaDisa 2006).

Stenting introduces significant and chronic alterations in the biomechanical environment of the cells within the local coronary arterial wall. The levels of stresses and strains are elevated compared to normal physiological conditions and these levels have been used as determinants in ISR development (Arakawa et al. 1998; Zahedmanesh et al. 2010). The proliferative vascular response in the restenosis process is exacerbated by the persistent stimuli of rigid metallic struts within the arterial wall (Topol, 2008). Vessel stiffness is increased by the presence of the expanded stent. Consequently, the cyclic strain environment in the artery is changed from a low-mean, high-amplitude strain environment to a high-mean, low-amplitude strain environment (Vernhet et al., 2000), as shown in Figure 2.5. In a stented artery the mean strain can increase by as much as 20-50% and the cyclic strain amplitude can fall as low as 1-2% (Vernhet et al., 2001, 2000). Cyclic strain amplitude is an important regulator of SMC growth capacity within a stented artery (Colombo et al. 2012). Therefore, compliant stent designs that allow cyclic strain amplitude levels to remain close to the normal physiological range (5-8%) (Draney et al., 2002; Vernhet et al., 2000), and thus maintain the anti-proliferative effect of cyclic strain on SMCs, could offer an effective strategy to reduce the rates of ISR.
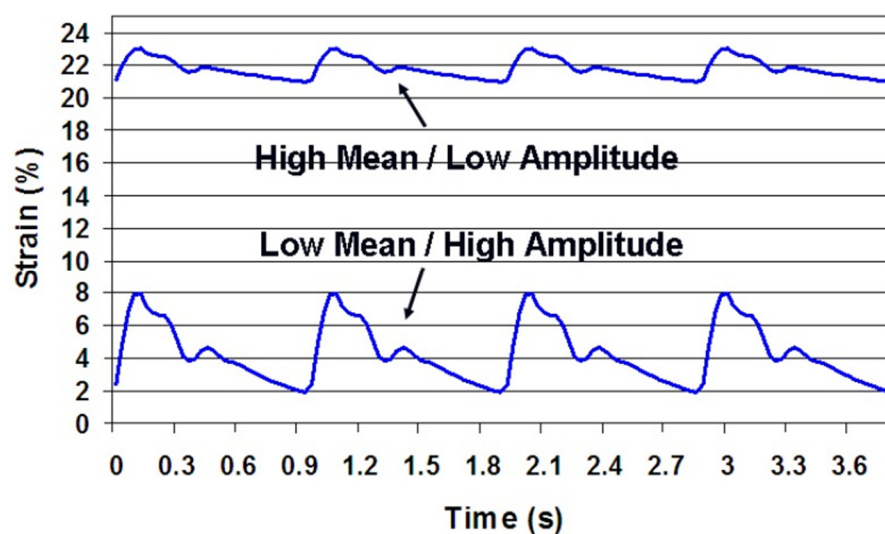
Figure 2.5 Influence of stenting on the cyclic strain environment in the local coronary artery

2.3 Coronary Stents

Coronary intravascular stents are cylindrical mesh structures which are expanded at the site of stenosis in order to scaffold the vessel walls and prevent elastic arterial recoil (Lally et al., 2006). Coronary stents are traditionally manufactured from materials such as stainless steel (316L), cobalt chromium, tantalum, titanium, nitinol or polymers (Sangiorgi et al., 2007). Stent deployment is normally achieved by expanding an angioplasty balloon (pressure >16 bar) onto which the stent has been crimped. Alternatively, deployment may be achieved by releasing a self-expanding stent or a coiled stent from a restraining sheath. Stents are used to mechanically support the vessel wall, to treat balloon or atherectomy device-induced coronary dissections, and to minimise post-procedure vessel recoil and late negative vascular remodelling (Savage et al., 1994; Topol, 2008). The stent diameter is normally selected to approximate a 1.1:1 ratio compared to the angiographically normal adjacent vessel, while stent length should cover the entire lesion length (Topol, 2008). Advantages of stent procedures include relatively mild morbidity, fast reperfusion and rapid stabilisation of patients with MI. Limitations of stents include the inability to treat a CTO (Topol, 2008).

2.3.1 Bare-Metal Stents

The results of a number of clinical trials reported that bare-metal stents (BMS) reduced ISR rates from 35% with PTCA to 19% (Kandzari et al., 2002; Mercado et al., 2001). However, ISR and ST remain a major limitation of BMS implantation. In general, an event that occurs within 30 days of stenting is called an early stent thrombosis (EST). An event that occurs more than 30 days and 12 months after stent implantation is called a late stent thrombosis (LST), and a very late thrombosis (VLST), respectively. Studies have shown that LST is uncommon with BMS, and that events have a mean time of 2.4 to 3.6 months. Although the incidence of ST is low with BMS (<2% of cases) there is a high risk of MI or even death (Ong et al.,

2005). In order to address the complications associated with using BMS, new types of drug-eluting stents (DES) were developed.

2.3.2 Drug-Eluting Stents

Typically, DES are composed of three principal components: the stent backbone (often a BMS platform), the pharmacologic agent (typically anti-proliferative drugs such as sirolimus, paclitaxel, taxus, zotarolimus or everolimus) which is intended to reduce IH and sometimes other effects, and a polymer designed to mediate abluminal drug release over a two-to-four week period (Bailey 2009) in order to reduce ISR (Garg & Serruys, 2010). Several clinical trials (CYPHER, RAVEL, SIRIUS, TAXUS, ENDEAVOUR, and SPIRIT) have been performed that demonstrate the ability of DES to significantly reduce ISR, LST and TVR rates (typically <3%, <1% and <10% respectively) compared to BMS (Dangas et al., 2013; Kandzari et al., 2013). Despite these improvements, limitations remain with regard to the safety and efficacy of DES in terms of late adverse clinical events, such as LST and ISR. The suggested mechanisms for ISR and ST with DES include in-stent neo-atherosclerosis, neointimal hyperplasia, persistent endarteritis, uncovered struts, stent malapposition (Colombo and Latib 2008), strut fracture (Alqahtani et al., 2013; Aoki et al., 2007; Lim et al., 2008) and the persistent presence of the device (Sammel et al., 2013). Patients implanted with DES normally require DAPT for about 3 months in order to minimise the risk of ST (Kim et al., 2009; Nishinari et al., 2013); though a number of side-effects are associated with DAPT (Albaladejo and Samama, 2010). Many experts suggest that continued development of permanent stents (BMS and DES) is not likely to eliminate these problems and therefore radical alternatives to conventional stents, such as bioabsorbable stents (BAS), must be developed (Di Mario and Ferrante, 2008).

2.3.3 Bioabsorbable Stents
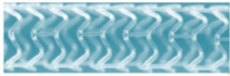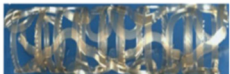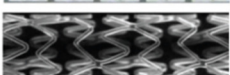
After stent implantation, the local vascular healing response (re-endothelisation,

remodelling etc.) and the majority of cardiac events including ISR normally occurs within six-to-nine months (Edelman and Rogers, 1998), beyond which the utility of permanent stents is unclear (Colombo and Karvouni, 2000; Jabara et al., 2009; O'Riordan, 2006). Permanent stents interfere with normal vessel function and can induce adaptive changes and abnormal reactions in the local tissue (Hoffmann et al., 1996). Owing to the drawbacks of BMS and DES, intravascular stent technology has progressed toward the development of bioabsorbable stents (BAS) that temporarily scaffold the vessel during the initial period of high risk for recoil, and then degrade in the long term (Erne et al., 2006). The gradual loss of mechanical integrity due to the bioabsorption of the stent should reduce the stimuli for endothelial irritation, endarteritis, IH, and ISR (Williams, 2006) while facilitating the restoration of normal local vascular compliance and permitting positive late remodelling (Anis and Karsch, 2006). BAS may help avoid many of the long term problems of permanent stents, such as LST and ISR. BAS do not preclude repeat PCI or surgical revascularisation, may be used repeatedly in a single vessel, may be useful in paediatric patients where growth adaption and repeat PCI is often required and may provide new treatment options for diffuse disease and unstable or vulnerable atherosclerotic plaques (Gundogan et al., 2014). As the degradation of BAS and their polymer coatings is not expected before six months, it is unlikely that the minimum duration of DAPT for coated BAS will differ greatly from current metallic DES (Kim et al., 2009; Nishinari et al., 2013); though uncoated BAS could potentially minimise DAPT to one month or less in line with BMS guidelines (Levine et al., 2011).

Stack et al. developed the first BAS, composed of poly-L-lactide (PLLA) and tested it in animal models (Stack et al., 1988). The Igaki-Tamai stent (Kyoto Medical Planning Co. Ltd, Kyoto, Japan) was the first coronary BAS implanted in humans in 1998. The PLLA stent demonstrated safety and efficacy at 6 months (Tamai et al.,

2000) and in a long-term (>10 years) study (Nishio et al., 2012). Currently, there are more than fourteen BAS available with the majority of these still under preclinical or clinical evaluation, as shown in Figure 2.6. A review of all current BAS platforms is beyond the scope of this work but may be found in (Gundogan et al., 2014; Zhang et al., 2013). Instead, the sections that follow focus on absorbable magnesium stents.

Current BAS technology has a number of shortcomings that limit their application in current clinical practice such as relatively large strut thicknesses and crossing profiles (Gogas et al., 2014), limited extensibility and higher risk of strut fracture (Zhang et al., 2013). BAS pose significant development challenges. The ideal period that a coronary stent needs to remain in place is unknown, though some clinicians suggest six-to-nine months may be sufficient (Colombo and Karvouni, 2000). Also, stent manufacturers are proposing different BAS solutions such as polymeric, bare-metal, hybrid, and drug-eluting BAS platforms. An effective BAS should possess a number of characteristics such as similar or better acute and long term performance compared to current generation metallic DES, adequate radial strength, steerable biodegradation kinetics, minimal or zero inflammatory or thrombotic response with normal endothelial function and non-toxic degradation products that leave no residual substances in arterial tissues (Bailey, 2009; Topol, 2008; Weiß et al., 2009). While PTCA, BMS, and DES are regarded by many as the first, second, and third revolution of interventional cardiology, BAS are being heralded by many as the fourth revolution (Onuma and Serruys, 2011). The global coronary stent market, which had a value of €5.5 billion in 2012, is expected to grow to €7.75 billion by 2016, with BAS projected to account for about €1.3 billion of this annual figure (Transparency Market Research, 2014).

Scaffold	Company	Status	Strut material	Coating material	Drug elution
Igaki-Tamai	Kyoto Medical	CE mark	PLLA	Nil	Nil
Absorb BVS 1.1	Abbott	CE mark	PLLA	PDLLA	Everolimus
DREAMS 1.0 DREAMS 2.0	Biotronik	On clinical studies Under preclinical evaluation	Magnesium Magnesium	PLGA PLLA	Paclitaxel Sirolimus
ReZolve™	REVA Medical	On clinical studies	Poly-tyrosine derived polycarbonate	Nil	Sirolimus
DeSolve™	Elixir	On clinical studies	PLLA	–	Novolimus Myolimus
BTI Ideal™	Xenogenics	On clinical studies	Polymer salicylate + linker	Salicylate + different linker	Nil Sirolimus
ART18Z	ART	On clinical studies	PLLA	Nil	Nil
Amaranth	Amaranth	On clinical studies	PLLA	Nil	Nil
Xinsorb	Huaan Biotech	Preclinical	PAL, PCL, PGA	–	Sirolimus
Acute	OrbusNeich	Preclinical	PLCL, PDLA, PLLA	–	Sirolimus +CD34 antibody
MeRes™	Meril	Preclinical	PLA		Merilimus Sirolimus
FADES	Zorion Medical	Preclinical	PLGA Magnesium	Nil	Nil
Others					
Avatar	S3V	Preclinical	–	–	–
Sahajanand	Sahajanand	Preclinical	–	–	–

Abbreviations: BRS, bioresorbable scaffold; BVS, bioresorbable vascular scaffold; CE, Conformité Européenne; PDLA poly-D, L-lactide acid; PLGA, poly-lactide-co-glycolide; PLLA, poly-L-lactic acid. PLCL, poly-L-lactide-co-ε-caprolactone;

Figure 2.6 Details of current bioabsorbable stents (BAS) platforms (adapted from (Zhang et al., 2013))

Magnesium Stents

The efficacy of an absorbable magnesium stent was first investigated by Heublein et al. who implanted a prototype stent made from the AE21 alloy in porcine coronaries (Heublein et al., 2003). The first absorbable magnesium stent (AMS-1, Biotronik AG) implanted in human coronaries was manufactured from the WE43 alloy, as shown in Figure 2.7(a). However, the corrosion rate and loss of scaffolding was too rapid and

resulted in relatively high rates of late vessel recoil. The absence of an anti-proliferative drug on the AMS-1 also led to high rates of IH and ISR (Erbel et al., 2007). In order to address these limitations, the DREAMS-1 stent (AMS-3, Biotronik AG) had a revised alloy (non-commercial WE43 derivative) and stent design which incorporated a paclitaxel-eluting polylactide-co-glycolide (PLGA) coating, as shown in Figure 2.7(b). Lower recoil and IH were reported and the corrosion profile was extended with restoration of normal vasomotor function reported at six months. The stent was shown to be safe and demonstrated modest efficacy with regard to late recoil and TVR rates (Haude et al., 2013). A number of design iterations were made to the DREAMS-2 stent including the use of tantalum markers on a revised stent design and a sirolimus-eluting PLA coating, as shown in Figure 2.7(c).
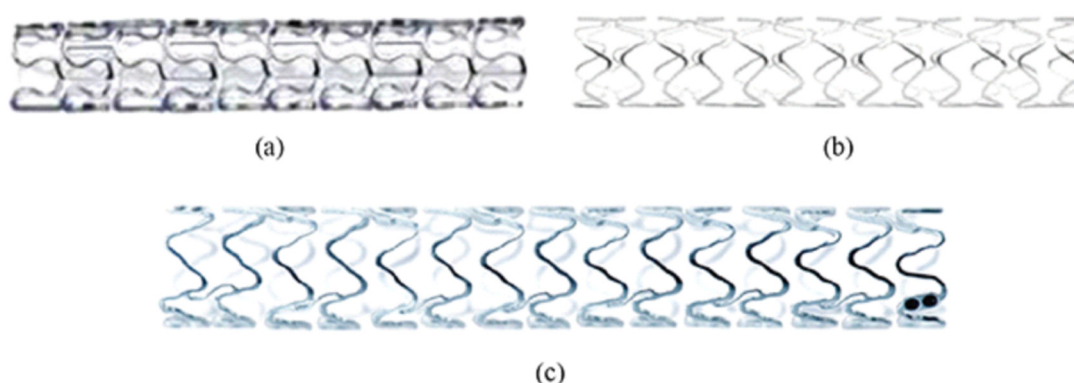
Figure 2.7 Magnesium coronary stent platforms manufactured by Biotronik AG: (a) AMS-1, (b) DREAMS-1 and (c) DREAMS-2

Compared to DREAMS-1, DREAMS-2 showed increased flexibility, larger deployment diameter capability, improved endothelialisation and reduced inflammation in preclinical trials (Guy, 2013). A PLGA coating that used a mixture of 85% lactide and 15% glycolide provided the lowest intimal area at 28 days and 180 days, and the highest endothelialisation score at 28 days in a porcine model (Wittchow et al., 2013). The alloy used in DREAMS-2 (WE43 derivative) degraded (0.036-0.072 mg cm^{-2} day^{-1}) into a magnesium-rich compound containing a large

amount of oxygen, most likely in the form of magnesium carbonate ($MgCO_3$) and $Mg(OH)_2$ after 28 days in a porcine artery model, as shown in Figure 2.8. These compounds were converted into a soft and gel-like amorphous calcium phosphate product after 90-to-180 days implantation. The accumulation of calcium products in the arterial wall may be of concern as it could potentially act as a precursor to atherosclerotic plaque which is calcium-rich (Holzapfel et al., 2004); though this requires further investigation. The performance of DREAMS-2 is being assessed in the BIOSOLVE-II trial which commenced in late 2013.
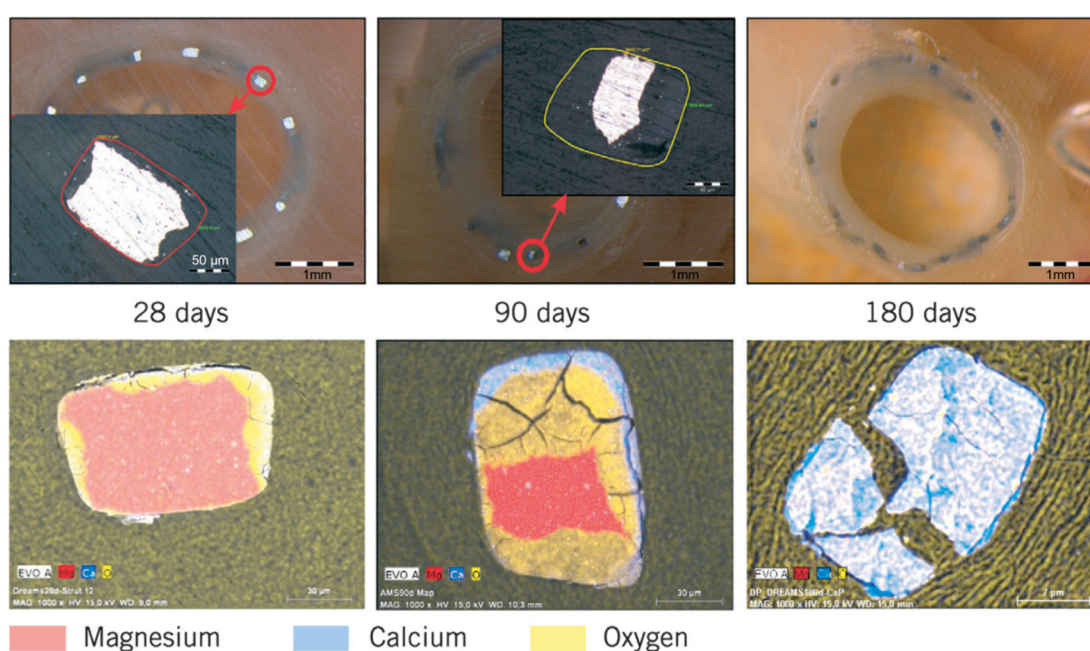
Figure 2.8 SEM images and EDX mapping of DREAMS-2 degradation products after 28, 90 and 180 days implantation in porcine coronary arteries (Wittchow et al., 2013)

Investigations are on-going to assess the utility of various other magnesium alloy systems for stent applications such as Mg-Y-Zn (Hänzi et al., 2010), Mg-Zn-Zr (Hong et al., 2013), Mg-Zn-Mn (Fang et al., 2013) Mg-Zn-Y-Nd (Wu et al., 2012), Mg-Nd (Seitz et al., 2012) and Mg-Li (Zhou et al., 2013), amongst others. The ZMED stent (Zorion Medical, IN, USA) is a wire-form, balloon-expandable fully-absorbable drug-eluting BAS composed of a (RE-free) proprietary magnesium alloy. Preclinical studies showed that the device was completely absorbed with minimal

inflammatory tissue response within ninety days. Further preclinical evaluations are needed before a first-in-human study which will begin in early 2015 (Zorion Medical, 2014). Other companies with absorbable magnesium stent programs include Medtronic Inc. MN, USA (magnesium alloy stent with sirolimus coating), Boston Scientific Corporations MA, USA (magnesium alloy) and QualiMed Innovative Medizinprodukte GmbH, Winsen, Germany (magnesium alloy and polymer hybrid).

The aforementioned trials have shown that magnesium stents are safe and feasible within small study groups and for simple lesion types. Despite this, only a limited amount of data regarding their mechanical and corrosion performance characteristics has been reported in animal (Di Mario et al., 2004; Heublein et al., 2003; Waksman et al., 2006) and clinical (Bosiers et al., 2009; Erbel et al., 2007; Haude et al., 2013) trials. Therefore, studies that can reveal the mechanical and corrosion performance of magnesium stents are needed. Further, the elucidation of the biomechanical environment that is supported by magnesium stents may prove crucial in helping to solve the problem of ISR owing to the influence of cyclic strain amplitude and stent radial stiffness on the development of restenosis (Colombo et al., 2012; Vernhet et al., 2001).

WE43 was selected for this study as it was used in multiple generations of the Biotronik AMS platform (AMS-1 to AMS-4) and currently represents the only magnesium stent platform to successfully go through clinical trials for coronary (Haude et al. 2013; Waksman et al. 2009; Erbel et al. 2007) and peripheral (Bosiers et al. 2005; Bosiers et al. 2009) applications. However, limitations associated with current magnesium stents include low mechanical properties compared to commercial BMS and DES, relatively high rates of late lumen loss due to excessive IH formation and premature loss of scaffolding (Erbel et al., 2007; Haude et al., 2013), and biocompatibility concerns associated with alloying elements that may remain in vascular tissues after stent degradation (Feyerabend et al., 2010).

These limitations can be addressed in future through the development of high-purity magnesium alloys (particularly with minimal impurities such as Fe, Cu, Ni and Si) alloyed with high-purity hardeners (non-misch metal) and alloying elements (such as Zn, Nd, Zr, Y) that are biocompatible and safely eliminated from arterial tissues following device degradation (Li and Zheng, 2013). Ultra-fine or nano-crystalline magnesium alloys offer significantly improved mechanical and corrosion performance and may be obtained by a number of severe plastic deformation (SPD) techniques that are the subject of on-going research and development (Zheng et al., 2014). Further improvements in corrosion performance and stent biocompatibility (improved endothelialisation, reduced inflammation and IH, ISR and ST rates) will be achievable through surface modification techniques, such as surface treatments and coating and drug elution strategies specific to magnesium alloys (Hornberger et al., 2012).

2.4 Magnesium and Magnesium Alloys

Magnesium is essential to human health and is involved in numerous metabolic reactions and biological mechanisms (Hruby and McKeown, 2013). Magnesium deficiency is common in industrialised nations and can increase our susceptibility to many illnesses, including CAD and stroke (Hartwig, 2001). Oral magnesium supplementation can improve endothelial health (Fuentes et al., 2006), offer a modest reduction in CAD risk (Mathers and Beckstrand, 2009) and can aid skeletal growth and development. The risk of hypermagnesemia is low as the kidneys very efficiently excrete excess magnesium (Birrer and Shallash, 2002). Absorbable magnesium implants were first explored in the early twentieth century but were later abandoned due to the inherent rapid corrosion and evolution of hydrogen (H_2) gas subcutaneously (Witte, 2010). Recent progress in magnesium metallurgy, further understanding of corrosion processes, and the development of corrosion protection techniques has seen a burgeoning interest in magnesium biomaterials (Song, 2011).

Magnesium alloys possess many physical and chemical properties that make them highly-suited for use in coronary stents such as low thrombogenicity and high biocompatibility (Erbel et al., 2007), suitable mechanical properties (Zheng et al., 2014) favourable corrosion kinetics (Kirkland et al., 2010) and zero magnetisation (MRI and CT compatible) (Staiger et al., 2006). The metabolic conversion of magnesium to its chloride, oxide, sulphate, and phosphate salts is well tolerated *in vivo* and the resulting by-products are not retained in the arterial wall (Bowen et al., 2014). Intravenous administration of magnesium has been shown to be safe and acts as a systemic and coronary vasodilator (Fuentes et al., 2006). *In vitro* testing involving human cells has shown that magnesium can control SMC proliferation and stimulate ECs (Sternberg et al., 2011). Extensive preclinical testing has shown that bare-metal and drug-eluting magnesium-based absorbable stents are both safe and feasible (Erbel et al., 2007; Haude et al., 2013).

Although the mechanical properties of pure magnesium are too low for load-bearing implants such as stents, the strength, ductility and corrosion resistance of magnesium can be significantly improved by developing high-purity alloys (Zainal Abidin et al., 2013) and by using alloying elements which aid precipitation and solid-solution hardening (Yang et al., 2008). Micro-alloying with RE elements such as Y, Zr, Nd and Ce produces ductile alloys with high fatigue strength and fine microstructural features that can restrict grain growth during solidification and pin grain boundaries during later thermo-mechanical processing (Song, 2011). Therefore, RE alloys such as WE43 are of particular utility in stent manufacturing where the material is repeatedly subjected to thermo-mechanical processing steps such as tube drawing and stress-relief by annealing (T-5 and T-6 heat treatments) (Hänzi et al., 2010)), and in-service where the stent is subject to cyclic loading under the influence of pulsatile blood flow in the coronary artery (Hänzi, Gerber et al. 2010).

2.4.1 The WE43 Alloy

WE43 typically contains (by weight %) approximately 93% magnesium, 3.7-4.3% yttrium (Y), >0.4% zirconium (Zr), with the remainder (2.4-4.4%) consisting of RE elements, principally Neodymium (Nd) (2.0-2.5%) and heavy RE elements such as Ytterbium (Yb), Erbium (Er), Dysprosium (Dy) and Gadolinium (Gd) (Magnesium Elektron, 2007). Zr is a potent grain-refining agent in magnesium alloys and contributes to strengthening due to the formation of fine grains by grain boundary strengthening (Avedesian and Baker, 1999). Y and Nd are used mainly to increase strength and service temperature, and to improve creep and corrosion resistance (Zhang et al., 2009). Y is commonly added to magnesium alloys in the form of Y-rich misch metal which contains impurities (such as Fe, Ni and Si) that may be detrimental to corrosion performance (Song and Atrens, 2003). Moreover, Y-rich misch metal contains approximately 20% by weight of other RE elements (such as Nd, La, Dy, Ho, Er, Tm, Yb and Lu) (Zhang et al., 2009). The effects of these RE elements *in vivo* is not completely understood though *in vitro* studies involving human SMCs suggest that some RE elements may have cytotoxic effects and negative influences on inflammatory reactions (Drynda et al., 2009; Feyerabend et al., 2010).

One of the notable features of Mg-Y alloys is that they exhibit both solution and age-strengthening effects; these being strongly linked to the solubility of Y in α-Mg matrix and the volume of intermetallic phases (Zhao et al., 2011). The Mg-Y and Mg-Zr phase diagrams are shown in Figure 2.9(a) and (b), respectively. From these phase diagrams it can be seen that a small change in composition can result in different phases and hence different material properties occurring. Therefore, control of the composition is important. The process of grain refinement using Zr may be described with reference to the phase diagram shown in Figure 2.9(b). For alloys such as WE43 which are saturated with Zr in the liquid phase, cooling allows some

26

precipitation of α-Zr particles as the freezing temperature is approached. At the peritectic temperature (~654°C), suspended Zr particles can form nuclei for the peritectic reaction with Zr-saturated Mg liquid to produce solid α-Mg with high Zr content. Owing to the close similarity in Mg and Zr lattice parameters, on final solidification a relatively homogenous distribution of fine hexagonal grains forms which reflects the growth mode of the two components. As maximum solubility of Zr is necessary for obtaining the highest grain refinement, some elements which form stable high melting point compounds with Zr should ideally be removed and not be present in Mg-Zr alloys such as Al, Si, Fe, Ni, Mn Sn, Co and Sb (Friedrich and Mordike, 2006).
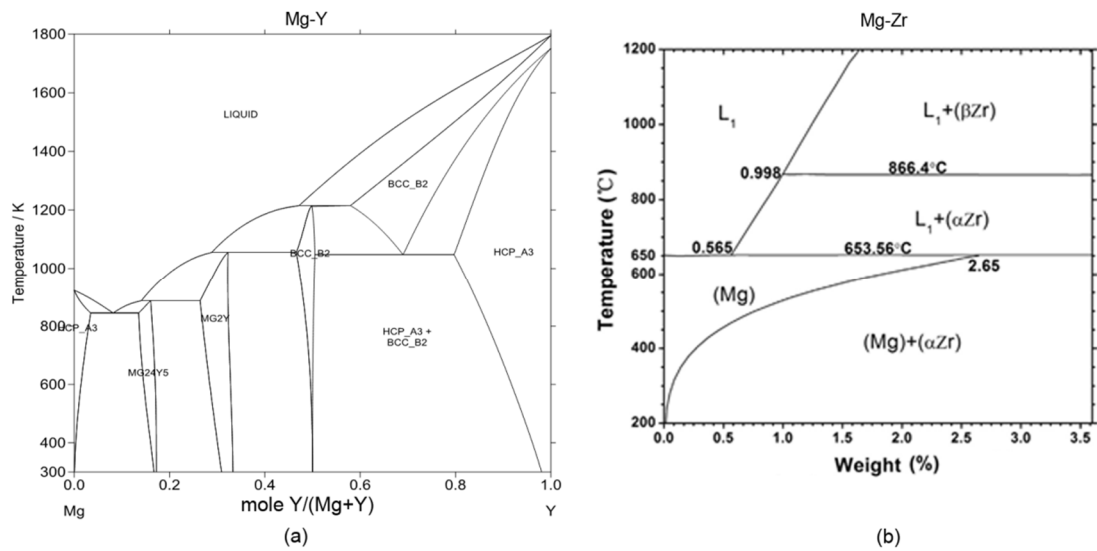
Figure 2.9 Phase diagrams (a) Mg-Y (b) Mg-Zr (Li et al., 2013; Zhao et al., 2011)

The microstructure of wrought and heat-treated WE43 normally consists of recrystallised grains with a large volume fraction of precipitates within the α-magnesium matrix. Typically, the precipitates present include (1) $Mg_{12}(RE,Y)$ polyhedral precipitates located within the matrix at grain boundaries, (2) spherical Zr-rich and cubic Y-rich precipitates, both containing Fe and Si impurities and (3) needle-like β-phase precipitates, as shown in Figure 2.10 (Coy et al., 2010). The relative Volta potential differences between micro-constituent phases and the α-

27

magnesium matrix indicate the corresponding role of the micro-constituent phases in potential galvanic interactions. In the case of WE43, Zr-rich precipitates exhibit greater volta potential differences (+180 mV) when compared to Y-rich precipitates in the presence of Fe (0.2 at.%) (+90 mV), $Mg_{12}(Nd,Y)$ (+25 mV) and β-phase precipitates (+15 mV) (Coy et al., 2010).
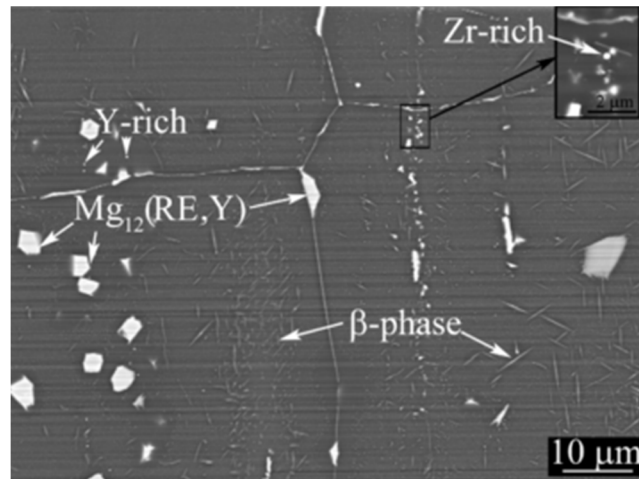
Figure 2.10 Backscattered scanning electron micrograph of wrought WE43 alloy (Coy et al., 2010)

2.4.2 Mechanical Properties of Magnesium Alloys

A useful review of the mechanical properties of many current absorbable magnesium alloys was presented by Li and Zheng (Li and Zheng, 2013). Studies have reported moderate to strong asymmetry in the mechanical properties (ratio of yield stress in tension and compression) of magnesium alloy tubes with consistently lower properties observed in compression when compared to tension (Gunde et al., 2011; Vedani et al., 2012). This has been attributed to the crystallographic texture of samples and to the occurrence of preferred {10–12} <10–11> twinning in compression. Heat treatment provides an effective method to reduce asymmetry, which is advantageous with respect to the fatigue behaviour of stents where the lower of the tensile or compressive yield stress value determines the fatigue strength (Frey et al., 2005). A number of studies have reported mechanical

properties for extruded WE43 derived from heat-treated bulk test specimens (Gu and Zheng, 2010; Magnesium Elektron, 2007; Witte et al., 2008). However, bulk specimens have very different materials processing histories to stents and the presence of size effects means that the mechanical behaviour may not capture the true behaviour of the device (Connolley et al., 2005; Murphy et al., 2003; Savage et al., 2004; Wiersma and Taylor, 2004). The processing of magnesium alloy stent precursor tubes has been described in a number of studies (Fang et al., 2013; Ge et al., 2013, 2011; Hassel et al., 2006). To date, few studies have reported mechanical property data for stent precursor tubes of the WE43 alloy (Witte et al., 2008) or other magnesium alloys (Hassel et al., 2006; Kutniy et al., 2009); though the surface treatments used in these studies differed to those used for coronary stents. Generally, these studies did not report on the geometry of the specimens used and either employed no surface finishing or simple mechanical polishing of specimens. The mechanical properties for WE43 reported in these studies is summarised in Table 2.1. Material property data that is derived from WE43 precursor tubes and from specimens with similar size scale and surface treatments as coronary stents are necessary. As well as revealing the true mechanical behaviour of finished WE43 stent strut materials, such experimental data would serve as input in future computational models of magnesium stent performance.

Specimen type	Elastic modulus, E (GPa)	Yield strength (MPa)	Ultimate tensile strength, UTS, (MPa)	Failure strain, (%)	Source
Bulk (extruded, T5 heat treated)	44	195-198	277-280	10-17	(Gu and Zheng, 2010; Magnesium Elektron, 2007; Witte et al., 2008)
Precursor tube	-	170	260	25	(Witte et al., 2008)

Table 2.1 Available data for the mechanical properties of WE43 specimens

2.4.3 Corrosion of Magnesium Alloys

Magnesium is one of the most anodic metals having a standard electrode potential

of -2.37 V. Therefore, with magnesium there is often a high chance of galvanic corrosion relative to other metal elements (Song, 2011). The corrosion processes and reaction kinetics of magnesium alloys depend on parameters including composition of the alloy, metallurgical treatment, surface treatment, composition of the interacting electrolytes, chemistry and biology of the environment, and the transport and metabolic phenomena associated with the reactants and the corrosion products (Bowen et al., 2012). The body electrolyte contains many anions (mainly chloride, phosphate, and bicarbonate ions), cations (mainly Na^+, K^+, Ca^{2+} and Mg^{2+}), organic substances and dissolved gases such as oxygen (Ratner et al., 1996). The high corrosion rates of magnesium alloys *in vivo* and in simulated body fluid (SBF) are generally attributed to the influence of aggressive ions such as chlorides, phosphates, sulphates and carbonates (Xin et al., 2008). Magnesium surfaces do not naturally passivate in aqueous chloride-containing solutions at physiological pH levels (Song, 2011) and so accelerated corrosion can be expected (Zhao et al., 2008). The corrosion attack in aqueous environments often involves galvanic coupling between anodic and cathodic areas that result in preferential dissolution of the (anodic) magnesium matrix (alpha (α) phase) and cathodic reduction of water (Zeng et al., 2006). The chemical process associated with the attack can be summarised as follows:

$$\text{Anodic reaction:} \ Mg \rightarrow Mg^{2+} + 2e^- \qquad (3.1)$$

$$\text{Cathodic reaction:} \ 2H_2O + 2e^- \rightarrow H_{2(gas)} + 2OH^- \qquad (3.2)$$

$$\text{Combined reaction:} \ Mg + 2H_2O \rightarrow Mg(OH)_{2(solid)} + H_{2(gas)} \qquad (3.3)$$
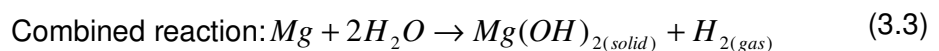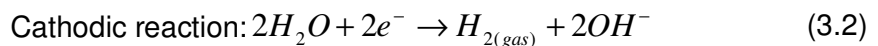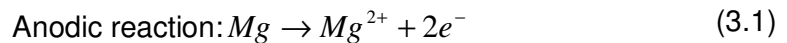
Generally, the dissolution rate of the α-phase exceeds the formation rate for the magnesium hydroxide ($Mg(OH)_2$) surface layer and so corrosion is not easily self-inhibited. Chlorides can transform the partially protective $Mg(OH)_2$ into soluble

MgCl$_2$, thus accelerating magnesium dissolution. The evolved H$_2$ gas causes further detachment of the surface layer and increases the surface alkalinity (Kainer, 2003).

Several studies have shown that magnesium alloys with fine-grained microstructures exhibit significantly higher corrosion resistance in chloride-containing environments as compared to coarse-grained microstructures (Alvarez-Lopez et al., 2010; Amira et al., 2008; Argade et al., 2012; Kannan, 2010; Song et al., 1999). This has been attributed to the higher fraction of continuous β-phase that is more finely distributed around finer α-grains and acts as a barrier to galvanic corrosion (Song et al., 1999). Fine-grained microstructures show lower porosity, higher polarisation resistance and the most positive pitting potentials and re-passivation potentials (Argade et al., 2012). The corrosion products (mainly magnesium oxide (MgO)) formed on the surface of fine-grained alloys are more protective against the action of chloride ions (Alvarez-Lopez et al., 2010). A one order of magnitude decrease in corrosion rate was observed between a coarse-grained (70 µm) and fine-grained (~0.7 µm) Mg-Y-RE alloy (Argade et al., 2012). Crystallographic orientation in magnesium alloys has a strong influence on surface processes such as corrosion, dissolution and oxidation (Song and Xu, 2012). The influence of crystallographic orientation was shown to be about 10% of the total corrosion depth for pure magnesium (Liu et al., 2008). Also, the highest corrosion resistance was observed for grains near (0001) orientation which are commonly found on the processed surfaces of precursor tubes.

A comprehensive discussion of all corrosion processes affecting magnesium alloys is outside the scope of this work but can be found in (Atrens et al., 2011; Song and Atrens, 1999). The main corrosion processes expected to influence the behaviour of magnesium alloy stents *in vivo* (Gastaldi et al., 2011) are discussed here, including micro-galvanic and localised (pitting and filiform) corrosion, inter-granular corrosion (IGC), stress corrosion cracking (SCC) and fatigue corrosion.

Micro-galvanic Corrosion

The non-uniformity in the composition, microstructure, and crystalline orientation of magnesium alloys can induce various chemical and electrochemical activities within the material resulting in micro-galvanic corrosion which leads to dissolution and thinning of the metal (Coy et al., 2010). Some areas, grains, phases, particles and impurities may act as anodes while others act as cathodes, as shown in Figure 2.11(a). Magnesium is susceptible to corrosion owing to galvanic activity among its primary constituents namely, primary α, eutectic α and β-phases, as shown in Figure 2.11(b). The magnesium α-matrix is an anode and is preferentially dissolved due to its lower content of alloying elements (Kalb et al., 2012) leading to undermining and fallout of the secondary phase particles, as shown in Figure 2.11(c).
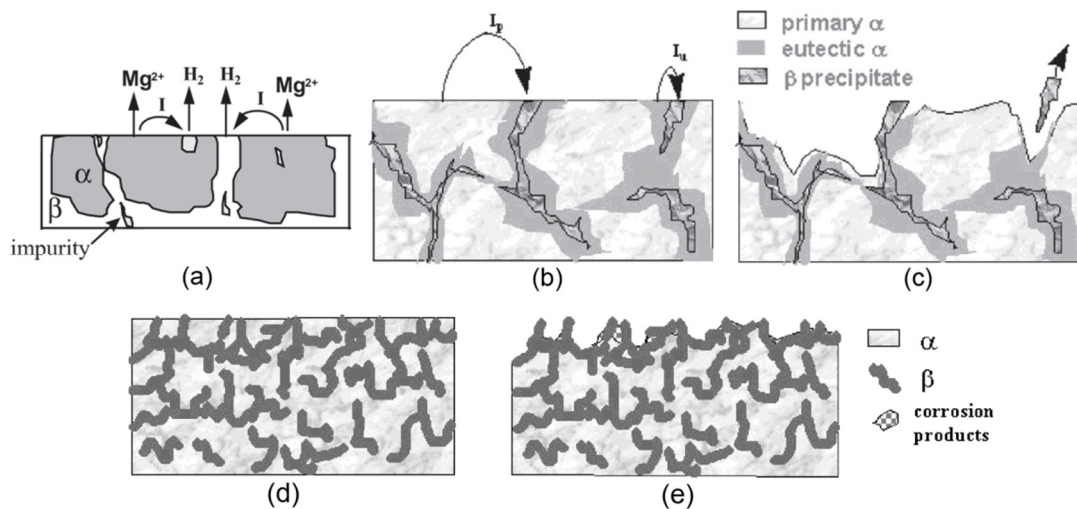
Figure 2.11 (a) Galvanic corrosion (internal) in magnesium alloys. (b) Galvanic activity among the primary α, eutectic α and β-phases and (c) the resulting morphology. (e) a continuous β-phase inhibits corrosion and (f) the resulting morphology

The β-phase serves as a galvanic cathode and accelerates the corrosion of the α-phase if the volume fraction of β-phase is small. However for a high volume fraction, a continuous β-phase can act as a barrier to inhibit corrosion (Atrens et al.,

2011), as shown in Figure 2.11(d and e). Galvanic corrosion processes at grains and grain boundaries can also be accelerated by deformation (plastic strain) in metal parts (Krawiec et al., 2012). In the case of a deformed stent strut, the tensile side of the strut may be anodic with respect to the compression side, leading to increased galvanic corrosion (Ratner et al., 1996).

Localised Corrosion

Pitting Corrosion: Pitting corrosion is a localised electrochemical reaction that leads to the formation of small pits on the affected surface. It can be initiated on stent surfaces by several processes such as damage of the passive film, localised plastic yielding during crimping and expansion, the production of stents with improperly polished surfaces, particle inclusions, inhomogeneous crystallinity or crystal defects causing dislocations to emerge on the surface and nonhomogeneous environments containing aggressive chemicals, such as chloride, causing localised dissolution of the passive film (Song, 2011). Pitting corrosion tends to initiate at irregular pits that spread laterally over the whole surface but may not form deep pits owing to the self-limiting nature of localised corrosion in magnesium (Song and Atrens, 2007).

Filiform Corrosion: Filiform corrosion is instigated by an active corrosion cell that migrates across the metal surface; the head is the anode and the tail is the cathode (Song and Atrens, 1999). Filiform corrosion does not occur on uncoated pure magnesium though it has been reported for anodized and coated magnesium materials (Lamaka et al., 2008) as well as for alloys with relatively resistant surface oxides (Lunder et al., 1994) such as the AZ series.

Inter-Granular Corrosion (IGC)

The grain boundaries are preferred sites at which precipitation and segregation of the β-phase occurs in magnesium alloys (Zeng et al., 2006). Magnesium alloys

rarely exhibit inter-crystalline attack because the grain boundary phases are invariably cathodic to the grain interior; instead, corrosion is normally concentrated in the area adjoining the grain boundary and may proceed until the grain is undercut and falls out (Song, 1999). IGC with rapid material dissolution and grain detachment has been reported for WE43 owing to selective attack of eutectic shaped Nd-based compounds at grain boundaries which act as anodic sites due to their low electrochemical potential with respect to grain areas (Valente, 2001). Additions of Zr may also lead to IGC in WE43 (Song, 2011).

Stress Corrosion Cracking

Stress corrosion cracking (SCC) results from a combination of static stress (either applied or residual) and a corrosive environment (as opposed to corrosion-fatigue where loading is dynamic) (Ratner et al., 1996). With magnesium alloys, corrosion may be initiated at a microscopic crack tip that does not re-passivate (Winzer et al., 2007). This leads to brittleness at the tip of the crack, because the H_2 gas evolved during the corrosion process is absorbed (Winzer et al., 2005b). Incremental crack growth may then occur resulting in implant failure. SCC is more marked in wrought, rather than cast magnesium alloys and is mainly transgranular in nature. SCC does not occur in pure magnesium and only occurs in Zr-containing alloys such as WE43 as stresses approach the yield stress (Song and Atrens, 1999).

Fatigue Corrosion

Stents are subject to cyclic (fatigue) mechanical loading due to the pulsatile nature of blood flow. The resulting strain, abrasion or wear may continuously rupture the surface passivation layer thereby reducing the corrosion resistance of the exposed material, thus increasing the number of metallic ions released (Ratner et al., 1996). Further, if a crack is present, anodic dissolution may occur at the tip of a crack. Corrosion fatigue is highly-significant as there is no limiting stress (endurance limit)

below which corrosion-induced cracking will not occur. In their study on WE43, Gu et al. (Gu et al., 2010) showed that the fatigue strength of samples in air was significantly reduced in static SBF and further reduced in dynamic SBF. Under the influence of cyclic loading the corrosion rate of specimens was shown to increase and a toughness fracture mode was identified where a crack initiated at a corrosion pit and propagated through the material.

2.4.4 Influence of Stent Manufacture on Magnesium Alloys

To date, a detailed study of the influence of laser cutting on the performance of WE43 stents has not been reported. The laser cutting of magnesium alloys requires the use of an inert shield gas (e.g. Ar or Nitrogen) rather than the use of O_2 which results in the formation of a refractory layer of MgO in the kerf which reduces cutting efficiency (Demir et al., 2013). Laser processing has been shown to increase the mechanical properties and reduce the micro-hardness of WE43 by influencing factors such as solid–solution strengthening, dislocations, second phase particles and geometrical constraints posed by grain boundaries that obstruct dislocation motion (Santhanakrishnan et al., 2013). A number of studies report significant increases in the corrosion resistance of magnesium alloys owing to the influence of the rapid heating and cooling induced in the HAZ during laser processing (Abbas et al., 2005; Guo et al., 2005; Liu et al., 2005). This has been attributed to morphological changes in the material microstructure such as significant grain refinement and the redistribution of intermetallic phases (Abbas et al., 2005). Higher concentrations of alloying elements on the machined surface, which aid the formation of more protective oxide films, have been reported for laser-processed magnesium alloys (Liu et al., 2005). Laser cutting stents from magnesium precursor tubes exposes higher index crystal planes of lower corrosion resistance (Liu et al., 2008). Hence, in the absence of sufficient surface treatment and HAZ removal, reduced corrosion resistance might be expected on these surfaces.

There are numerous surface treatment techniques available for the surface modification of magnesium alloy implants (Hornberger et al., 2012; Ma et al., 2014; Zheng et al., 2014). Chemical etching is often used with magnesium alloys in order to replace the native oxide layer with a more passive and corrosion resistant oxide layer (conversion coating) of lower porosity and lower surface roughness (Nwaogu et al., 2009). The chemical conversion layers, which are formed in a complex interaction of metal dissolution and precipitation in the aqueous solution, mainly consist of magnesium phosphate, MgO, $Mg(OH)_2$ and mixtures of other metal oxides and hydroxides, which arise from the dissolved ions in the bath (Gray-Munro et al., 2009). As the layers are grown *in situ*, adhesion to the substrate is good and the surfaces obtained facilitate the adherence of any subsequently deposited coating (Hornberger et al., 2012). In the case of AZ31 stents, chemical etching in a nitric acid solution has been used to remove the heat-affected zone (HAZ), dross and spatter that were formed on surfaces during laser cutting (Demir et al., 2012). Gray-Munro et al. described chemical etching in phosphoric acid solution in order to form a non-toxic coating on AZ31 specimens (Gray-Munro et al., 2009). The increased corrosion resistance observed was attributed to improved surface uniformity and crystallinity of the protective $Mg(OH)_2$ and magnesium phosphate layer that was produced by etching. Zhou et al. described the formation of a magnesium phosphate coating on an AZ91D specimen in three main phases: (1) corrosion of the magnesium matrix, (2) mass transposition in the liquid phase and the metal-solution interface, and (3) formation and growth of crystal nucleus (Zhou et al., 2008). Layer growth was attributed mainly to formation of $Mg(OH)_2$ at the substrate-layer interface by anodic reaction and dissolution mainly of the magnesium matrix material.

In medical device manufacturing, gas plasma processes offer useful surface modification (Yang et al., 2010) and sterilisation (Halfmann et al., 2007) techniques for devices with complex shapes, such as coronary stents. Plasma etching can be

used to remove manufacturing residues, foreign materials and bio-burden and offers a clean, safe and environmentally-friendly alternative to traditional wet chemical processes. Materials are removed from the surface by chemical reactions (to form volatile products) and physical sputtering using inert gases such as argon or neon. Due to the low energy of the gas plasma, layers of atoms are gradually removed from the surface without significantly modifying the microstructure of the substrate material (Yang et al., 2010). It has been shown that O_2 plasma processing of biomaterials leads to increased surface wettability (Yi et al., 2004) and enhanced adhesion properties for any subsequently deposited coating (Nakamura et al., 1996) which are of particular utility in the manufacture of coronary stents.

2.5   Computational Modelling of Magnesium Stents

The deployment of magnesium alloy stents by simple pressure and displacement loads have been simulated in a number of FE studies (Sabir et al., 2012; Wang et al., 2009). Grogan et al. (Grogan et al., 2012) compared the mechanical performance of magnesium, iron, 316L and Co-Cr stents, based on multiple stent platforms and predicted a higher fracture risk for magnesium stents owing to the lower plasticity of the material. Computational models based on crystal plasticity theory have been used to predict the influence of size effects in stent struts and highlight the improvement in deformation performance of magnesium stents for decreasing material grain size (Grogan et al., 2013). Similar model have been used to investigate the failure risk and load-bearing capacity of magnesium stent struts undergoing plastic deformations typical of stent expansion (Grogan et al., 2014b).

Wu et al. (Wu et al., 2010) applied an iterative morphing procedure in order to reduce the predicted concentrations of stress and strain in a 2-D RUC strut model during a stent deployment simulation. This procedure was combined with the corrosion model of Gastaldi et al. (Gastaldi et al., 2011) in a shape optimisation

study of a 3-D stent structure in order to identify a stent design that displayed lower mass loss and hence a prolonged scaffolding profile. The model was validated based on preliminary corrosion experiments that involved the optimised AZ31 stent design (Wu et al., 2012). A similar shape optimisation model was reported by Li et al. (Li et al., 2014) where model validation was based on experimental corrosion testing of unfurled stent geometries cut from AZ31 sheets. Although not discussed here, a number of corrosion models have also been developed and applied in computational studies of magnesium stents. This is discussed in section 2.5.1.

With the exception of the crystal plasticity models described above, many of the aforementioned computational studies employ FE modelling based on continuum plasticity theory where the material model parameters were derived from mechanical testing of specimens that did not have the same processing history as can be expected for magnesium stents (Gastaldi et al., 2011; Grogan et al., 2012, 2011; Wu et al., 2011, 2010). Therefore, improvements in the predictive capabilities of future FE models, based on continuum plasticity theory, may be obtained through the use of mechanical properties derived from specimens of precursor tube that have surface treatments similar to magnesium stents.

2.5.1 Corrosion Modelling

Several numerical models for external galvanic corrosion, based on the boundary element method (BEM), in which different galvanic couples are studied have been proposed for fixed (Jia et al., 2006) and moving mesh (Deshpande, 2010; Thamida, 2012) techniques. A mathematical model for micro-galvanic corrosion that accounted for the negative difference effect (NDE) that is observed in magnesium alloys was proposed by Liu and Schlesinger (Liu and Schlesinger, 2009). A numerical model for micro-galvanic corrosion within a binary phase metal alloy was developed by Deshpande (Deshpande, 2011) using the Arbitrary Langrangian

Eulerian (ALE) method. The model used the non-linear polarization behaviour of the alloy phases and tracked the moving boundary of the degrading phase. A mathematical model based on potential theory and calibrated based on *in vivo* corrosion data was used to show that the thickness of the electrolyte influenced the galvanic corrosion of magnesium (Montoya et al., 2014). A macroscale corrosion damage internal state variable (ISV) model that captured the effects of general corrosion, pit nucleation, pit growth, pit coalescence, and intergranular corrosion was developed by (Walton et al., 2014) and applied to the AZ31 magnesium alloy. Models of other corrosion processes have been developed and applied to magnesium alloys such as stress corrosion cracking (SCC) (Dietzel et al., 2010) fatigue cracking (Xue et al., 2007) and crevice corrosion (Sun et al., 2014).

Many of the aforementioned modelling approaches focus on specific corrosion processes that are not easily applicable to coronary stents due to the difficulty of establishing the model parameters by experimental calibration procedures, as well as the high computational costs associated with 3-D geometries. Therefore, a number of alternative models been developed specifically for modelling the corrosion of absorbable metallic stents. As numerical modelling of the various complex phenomena affecting the corrosion performance of metallic stents *in vivo* represents a significant challenge and as such this represents a relatively new field of research, only a small number of phenomenological (Gastaldi et al., 2011) and physical (Grogan et al., 2014a) corrosion models have been developed and applied to magnesium stents.

A phenomenological corrosion model was developed by Gastaldi et al. (Gastaldi et al., 2011) using the CDM approach and implemented within a FE framework in order to account for the effects of stress corrosion and uniform micro-galvanic corrosion processes on the behaviour of a 3-D magnesium alloy stent geometry. The model was calibrated from experimental corrosion studies performed

on mechanically polished cylindrical specimens of extruded magnesium alloys (AZ31, AZ61, AZ80, ZK60 and ZM21). The same corrosion model was later calibrated from experimental studies performed on specimens that were cut from magnesium alloy sheets and extruded bars and used to perform optimisation studies for magnesium stents in which outputs such as stress, strain, acute and corrosion-induced stent recoil and mass loss were examined (Wu et al., 2011, 2010). In a combined experimental and numerical study, Wu et al. (Wu et al., 2012) produced an AZ31 stent and compared experimentally observed elastic recoil and mass loss with those predicted by the corrosion model.

Grogan et al (Grogan et al., 2011) added an element-specific pitting corrosion parameter to the damage law developed previously by Gastaldi et al. (Gastaldi et al., 2011) in order to incorporate the effects of heterogeneous or pitting corrosion in the modelling framework. The model was calibrated based on corrosion experiments involving mechanically polished AZ31 foil specimens and was used to predict the corrosion-induced recoil and mass loss of an AZ31 stent that was deployed in an idealised coronary artery model.

A physical corrosion model, based on the FEM and adaptive meshing, was developed by Grogan et al. (Grogan et al., 2014a) to model the diffusion-controlled corrosion of a 3-D (pure magnesium) stent strut section. The study was predicated on a transport-controlled process, based on the assumption that metallic ion transport, particularly diffusion, was slower than the electrochemical reaction rate for the stent surrounded by layers of corrosion product and tissue in the body. The model predicted that the mass loss rate was proportional to the saturation concentration of magnesium ions in solution. The diffusivity of the surrounding environment was also shown to influence the corrosion rate.

The aforementioned corrosion models of magnesium stent performance

(Gastaldi et al., 2011; Grogan et al., 2011) involve stress-mediated corrosion processes. However, since the stent deployment procedure is known to induce large plastic strain (20-30%) (Murphy et al., 2003) corrosion models that explore the interaction of plastic strain and plastic damage with corrosion damage are required. Indeed, this has been recognised as one of the current challenges in degradable material modelling (Gastaldi et al., 2011). Further, these corrosion models were calibrated from corrosion experiments that used magnesium specimens that had materials processing, surface treatments, and loading regimes that were dissimilar to those of coronary stents which are all known to bear a significant influence on the mechanical and corrosion behaviour of magnesium materials (Gastaldi et al., 2011; Grogan et al., 2011). This is also true of many of the experimental studies of the corrosion performance of absorbable magnesium materials and devices that are currently available in the literature (Bowen et al., 2013; Coy et al., 2010; Grogan et al., 2011; Kannan et al., 2008; Zhang et al., 2010). Therefore, mechanical and corrosion experiments that use specimens with appropriate processing and loading histories relevant to magnesium stents are required in order to reveal the true behaviour of these devices. Such an approach should provide improvements in the quality of the experimental data obtained. Such data would also prove useful in the calibration and validation of numerical corrosion models of magnesium stent behaviour.

2.6   Summary

The optimum treatment strategy to resolve the problem of ISR following stenting with BMS and DES platforms has yet to be determined. Emerging strategies include bioabsorbable stents (BAS) which provide temporary arterial scaffolding and are absorbed in the body after six-to-thirty six months (Zhang et al., 2013). BAS materials under investigation include polymers and absorbable metals, such as iron and magnesium. Absorbable magnesium stents have shown promise in extensive

clinical trials (Erbel et al., 2007; Haude et al., 2013). However, these trials typically involved small patient cohorts and simple lesions and therefore performance comparison with commercially-available stents is difficult. Only limited performance data has been reported for magnesium stents in general and in particular for WE43 alloy stents which, to date, represent the only magnesium stent platform to go through coronary trials. It is known that the stent deployment characteristics, radial stiffness, and cyclic strain amplitude in a stented artery segment influence ISR outcomes (Colombo et al., 2009; Sangiorgi et al., 2007; Topol, 2008). As yet, these performance characteristics have not been reported for WE43 stents.

Ideally, *in vitro* performance assessment should be conducted on the finished stent or on samples of the precursor tube in the final form and finish owing to the influence of processing, surface treatment and size effects on device behaviour (Connolley et al., 2005; Murphy et al., 2003; Savage et al., 2004; Wiersma and Taylor, 2004). It is noted that while a number of experimental studies have reported on the mechanical and corrosion performance of magnesium test specimens (Bowen et al., 2013; Coy et al., 2010; Grogan et al., 2011; Kannan et al., 2008; Zhang et al., 2010) and simplified unfurled stent geometries that were cut from sheets (Li et al., 2014; Wu et al., 2010), few studies have employed finished magnesium stents as specimens (Wu et al., 2012) and no such studies have been reported for WE43 stents. Many of the experimental studies of absorbable magnesium materials in the literature employed specimens that had materials processing, surface treatments and loading regimes that differed to those of coronary stents (Bowen et al., 2013; Coy et al., 2010; Grogan et al., 2011; Kannan et al., 2008; Zhang et al., 2010); Therefore, the mechanical and corrosion behaviour of these specimens may not be representative of finished magnesium stents. Only a limited about of information regarding the mechanical and corrosion behaviour of WE43 stent precursor tubes is available (Witte et al., 2008). Fibre laser cutting and

surface treatment of balloon-expandable stents has been reported for the AZ31 alloy (Demir et al., 2012; Wu et al., 2012); though no such study has been reported for WE43.

While a number of studies have investigated the effects of mechanical loading on the corrosion of magnesium specimens for near-constant loads (Grogan et al., 2011) and non-constant loads (Kannan et al., 2008; Winzer et al., 2008), the influence of the stent deployment procedure on the corrosion performance of magnesium stents has not been extensively investigated. A number of experimental studies have attempted to correlate the magnitude of stress in the magnesium specimen to corrosion behaviour and have subsequently developed stress-mediated corrosion models of magnesium stent performance (Gastaldi et al., 2011; Grogan et al., 2011). Plastic strain, and the accompanying deformation-induced changes in electrochemical measurements in magnesium alloys have been shown to have a significant effect on galvanic corrosion processes, which are prominent in magnesium alloys (Snir et al., 2012; Wittke et al., 2014).

Since the stent deployment procedure is known to induce large plastic strain (20-30%) in stent struts (Murphy et al., 2003), we hypothesise that the plastic strain that is induced in magnesium stents during the deployment procedure plays a critical role in directing subsequent corrosion phenomena in the stent and therefore, has an influence on the scaffolding ability of the stent in the long-term. Therefore, in this work, plastic strain levels consistent with the deployment procedure were induced the stents and specimens produced and the resulting effects on the mechanical and corrosion performance of the specimens were explored in experiments. The data were also used in the development and calibration of a plastic strain mediated phenomenological corrosion model capable of simulating the corrosion behaviour of magnesium alloy stents.

3. Materials and Methods

3.1   Summary

Absorbable magnesium stents were laser cut from precursor tubes of the WE43 alloy. Surface treatments were performed using a combination of chemical etching and plasma etching processes. The manufacture and surface treatment of the WE43 stents used in this study is discussed in detail in (Galvin et al., 2013).

The mechanical performance of the magnesium stent was compared to that of a commercially-available 316L stent in three separate tests that determined stent deployment, radial strength and cyclic strain amplitude metrics.

The corrosion behaviour of stent and dogbone specimens was determined via immersion corrosion experiments performed in SBF under pseudo-physiological conditions. The influence of the deployment procedure on the corrosion behaviour of the stent was investigated in terms of temporal mass loss and corrosion-induced loss of mechanical integrity.

A corrosion algorithm was written in ANSYS parametric design language (APDL) and was developed for use with the ANSYS Implicit FE code. The corrosion model, which was calibrated from the experimental data, was used to simulate the corrosion performance of the magnesium stent. The results predicted by the model were compared to those observed experimentally.

3.2 Stent Manufacture

3.2.1 Laser Cutting

Coronary stents were manufactured from stent precursor tubes of the WE43 magnesium alloy. An initial compositional analysis of the tube was performed to confirm that the content of magnesium and the three main alloying elements (Y, Zr and Nd) was consistent with that specified by the manufacturer of WE43 (Magnesium Elektron, 2007), as shown in Appendix A.1. The tubes had an outer diameter of 2.1 mm and a wall thickness of 0.15 mm. The stent design was approximated from published images of the Biotronik AMS-1 platform (Di Mario et al., 2004). The unfurled stent geometry was first modelled in a computer-aided design software package (SolidWorks Corp., MA. U.S.A), as shown in Figure 3.1(a).
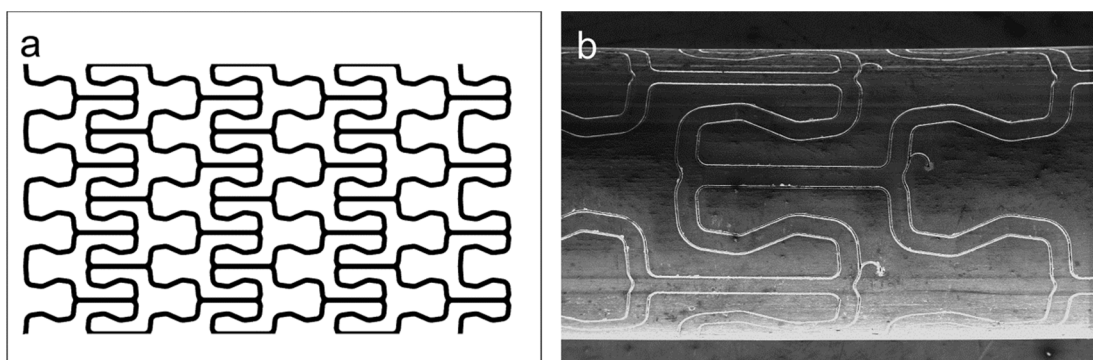
Figure 3.1 (a) Two-dimensional CAD model of the unfurled stent geometry (b) SEM image of a tube in which the stent pattern was machined

The computer-aided design data were then used to produce a computer numerical control (CNC) program that defined all cutting paths necessary to sculpt the stent by pulsed fibre laser machining (Starcut Tube, Rofin Baasel, UK Ltd.). The laser beam had a wavelength of 1070 ± 5 nm and diameter of 13 µm. Nitrogen was employed as an inert shield gas. A SEM image of a tube, in which the stent pattern was machined, is shown in Figure 3.1(b).

Figure 3.2(a) shows the stent after laser cutting with the sections of waste material removed. A significant amount of dross and spatter adherence was observed on the inner surface of the struts, as shown in Figure 3.2(b). This dross was subsequently removed by a combination of chemical and plasma etching processes. The finished stent had a length of 11.94 mm and an outer diameter of 2.09 mm. The thickness of struts in the radial and longitudinal direction was 140 μm and 120 μm, respectively. The average stent mass was 4.5 mg. The total surface area of the stent was 78 mm^2, as estimated from the computer model.
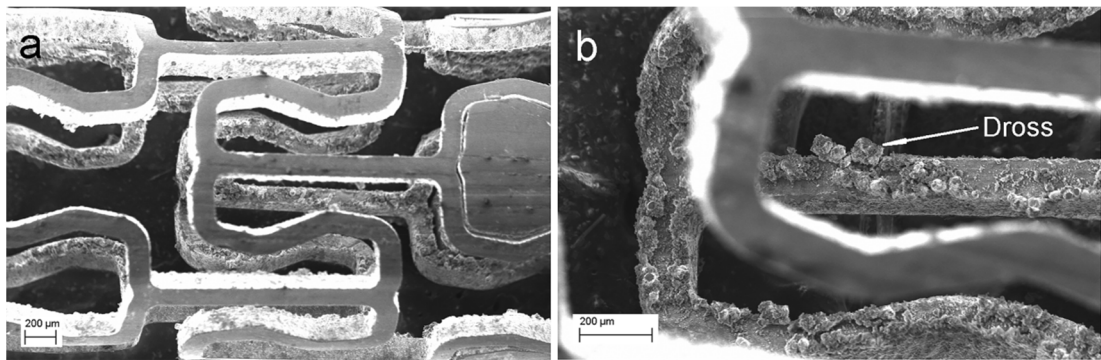
Figure 3.2 (a) Machined stent remaining after the inner sections had fallen out (b) dross that formed on the inner surfaces as a result of laser cutting process

3.2.2 Chemical Etching

A chemical etching process was employed to remove the bulk dross, spatter and heat-affected zone (HAZ) that were formed during laser cutting. This process also rounded-off strut edges and improved the surface finish and stent deployment characteristics. The stents were chemically etched in 85.2% phosphoric acid (P6560, Sigma Aldrich) at 55°C for 20 seconds and then neutralised immediately by immersion in sodium hydroxide solution (100g/L, S8045, Sigma Aldrich) for 30 seconds at 20°C. The stents were sonicated in ultrapure H$_2$O for 2 minutes, followed by alcohol for a further 2 minutes. Specimens were dried for 2 hours in a cleanroom environment (class 100) using a glass drying oven (B-585, BUCHI Labortechnik AG) at an air temperature of 25°C (Morshed et al., 2011).

3.2.3 Plasma Etching

In order to remove residues remaining from the chemical etching process the stents were placed in the chamber of a reactive ion etching (RIE) instrument (PlasmaLab 80 Plus, Oxford Instruments). A schematic diagram of the experimental setup used for the plasma etching process is shown in Figure 3.3.
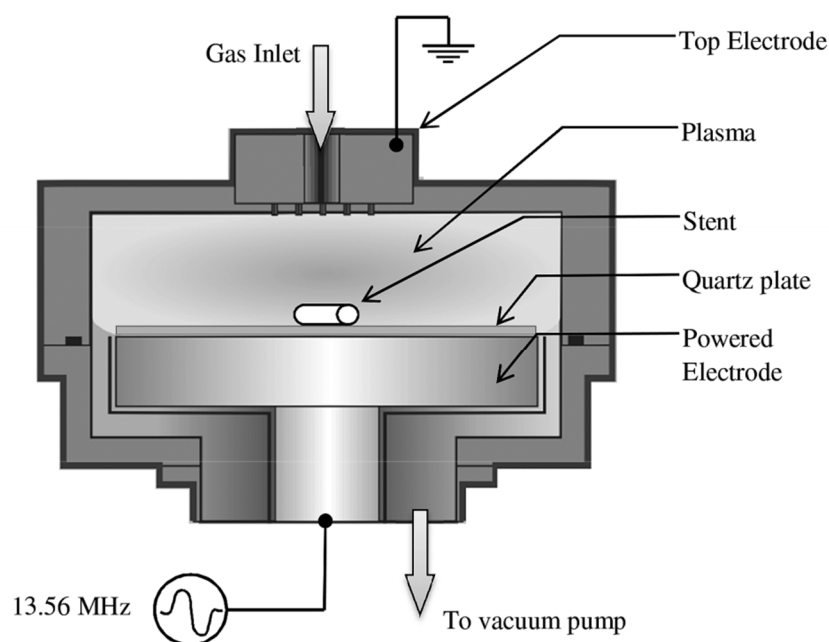
Figure 3.3 Schematic diagram of the experimental setup used for the plasma etching process

As RIE acts mainly as a "line-of-sight" process, etching was performed in three stages where the specimens were manually rotated in increments of 120° on a quartz plate in order to minimise shadowing effects. A capacitively-coupled plasma was generated by a 13.56 MHz radio-frequency (RF) power source. The RF-powered electrode was made from stainless steel and had an outer diameter of 240 mm. The grounded electrode was made from stainless steel and acted as a showerhead to supply the process gases. The distance between the powered and grounded electrodes was 46 mm. Plasma etching was performed in two separate

process steps using two different process gases. In the first step, the surfaces of the stents were plasma etched in a mixture of 90% argon (Ar) and 10% oxygen (O_2) gas for a total of 10 minutes. The comparatively heavy Ar ions removed material by a micro-sandblast effect upon striking the substrate (Chu et al., 2002). In the second step, the stents were cleaned and sterilised in 100% O_2 gas for a further 10 minutes. O_2 plasma reacts with molecules deposited on the substrate breaking them down and turning them into volatile compounds (Chu et al., 2002). In both cases the process conditions were kept constant where the chamber pressure was 100 mTorr, the power was 250 W and the flow of gas was 100 sccm. A bias voltage of ~495 V was recorded.

3.2.4 Surface Characterisation

Specimens of the WE43 tube having a length of 10 mm were laser cut, then degreased by sonication in alcohol and finally placed in a glass drying oven for 2 hours at 25°C. The tube specimens were subjected to the same chemical and plasma etching processes that were used to produce the stents. Specimens were prepared in three different conditions, namely as-received, chemically etched and plasma etched. Scanning electron microscopy (SEM), Atomic Force microscopy (AFM) and Energy Dispersive X-ray Spectrometry (EDX) analyses were performed on the tube specimens in order to characterise the morphology, roughness and chemical composition of surfaces for the three different conditions.

EDX Analysis

Prior to EDX analysis all specimens were sputter-coated with a thin film of carbon in order to render them conductive. EDX analysis was performed using an INCA Energy 350 XT microanalysis system (Oxford Instruments) in conjunction with a SEM (Leo 440 Stereo Scan, Leica Cambridge Ltd). The vacuum in the chamber was 2.0×10^{-6} mbar. The beam current and spot size of the electron gun was set to 1.0

nA and 520 nm, respectively. The working distance between the specimen and electron gun was maintained between 8.5 and 9 mm and the collection time for the EDX detector was 120 seconds. Quantitative EDX analysis was performed using the INCA Microanalysis Suite (v4.09) software package. Background correction was performed using the background modelling method where the detector background spectrum was subtracted from the observed spectral distribution by mathematical filtering using a top hat function. The intensity of spectral peaks corresponding to specimen elements were measured and compared to standards measured under known operating conditions by the software. Intensity ratios (k values) were calculated and converted into chemical concentration (weight %) for the elements detected within the specimen.

Surface Roughness Analysis

The surface texture of treated and untreated specimens was scanned using high resolution contact mode AFM (Nano-R™ O-020, Pacific Nanotechnology). A cantilever AFM tip (SICON-10P, Applied NanoStructures Inc.) was drawn along the outer surface of each specimen in the longitudinal direction. Three randomly selected regions, measuring 80 μm x 80 μm, were scanned on each specimen. The scan rate and number of lines in each scan were kept constant at 0.5 Hz and 256, respectively. The surface roughness parameter (Sa) was calculated without a filtering process using the SPM Cockpit™ (V3.3.383) software package according to the formula listed in ASME B46.1. A one-way analysis of variance (ANOVA) was used to test for differences among the surface roughness values (Sa) of the three specimen groups (as-received, chemically etched and plasma etched).

3.3   Mechanical Testing

Mechanical testing was carried out in order to determine deployment and cyclic strain amplitude metrics for the stent. A commercially-available generic modular

316L stent design (outer diameter (OD) = 3.5 mm, length = 9 mm, strut thickness = 0.09 mm) was also tested for comparison, as shown in Figure 3.4(b). Prior to deployment, each WE43 stent was mounted (uncrimped) on a 3.5 x 18 mm angioplasty balloon. The 316L stents were already crimped to the balloon (3.5 x 18 mm) on their delivery system when supplied. Stent performance was assessed in three different bench tests as described below. The tests were captured by videoextensometer and calibrated image sequences were used to calculate stent performance metrics. In each one of the three tests, three WE43 stents (n=3) and three 316L stents (n=3) were used.

Non-uniform deployment may be encountered with manually crimped stents (Morton et al., 2004) and was likely to occur with the WE43 stent due to its highly-compliant nature. Therefore, in this work, all WE3 stents were expanded without manual crimping to the angioplasty balloon in order to ensure a uniform deployed stent configuration. The crimping process induces significant compressive loading and deformation in stents and is known to change the subsequent stress-strain behaviour of the strut material during the deployment procedure, resulting from the tension-compression reversal behaviour (Bauschinger Effect) (Oberhofer et al., 2006). Thus, compared to uncrimped stents, crimped magnesium stents would likely exhibit slightly reduced mechanical properties and altered fatigue and corrosion behaviour owing to the influence of material deformation and residual compressive stresses (Zeng et al., 2008). The use of crimping machines may be necessary with magnesium stents in order to reduce asymmetries in the deployed configuration which have been associated with increased vascular injury and higher rates of IH and ISR (Schulz et al., 2000). In a preliminary FE study carried out in this work, a crossing profile of 1.3 mm was predicted for the WE43 stent which was comparable with that observed for the Biotronik AMS-1 (1.2 mm) (Di Mario et al., 2004).

Test 1: Free Expansion

Stents were freely expanded to a maximum balloon pressure (15 atm) and then permitted to undergo elastic recoil. Expansion behaviour was quantified through the determination of a pressure-diameter curve where the balloon pressure and the corresponding stent OD were tracked during the free expansion procedure. The stent diameter was calculated from the average of eight separate OD measurements made along the length of the stent, as shown in Figure 3.4(a). In order to account for differences in the strut thickness of the two stent types, stent performance metrics were calculated using stent ID data. This was derived from the OD measurements by subtracting the strut thickness in the radial direction.
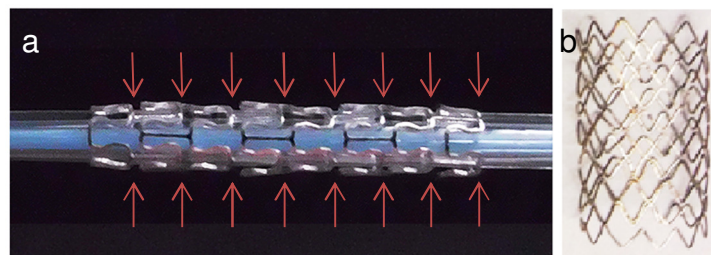
Figure 3.4 Free expansion of stents (a) Location of 8 stent OD measurements taken using a videoextensometer during bench testing (b) 316L stent

Test 2: Expansion in Mock Coronary Arteries

Stents were expanded inside mock coronary arteries (MCAs) that were prepared using a technique described in an earlier work (Colombo et al., 2010). The MCAs had an inner diameter of 3 mm and a wall thickness of 0.4 mm. A pre-stretch ratio of 1.1 was applied to each MCA using a custom fixture fitted with a linear translation stage and micrometer thereby mimicking the arterial tethering observed *in vivo*. Elastic longitudinal recoil (ELR), foreshortening (FS) and dogboning (DB) metrics were calculated using previously described formulae (Migliavacca et al., 2002). Elastic radial recoil (ERR) was calculated by determining the average recoil at eight

separate locations along the stent length, as shown in Figure 3.4. It was not possible to accurately measure the stent ID or OD by visualisation owing to the opacity of the MCA material. Therefore, ERR was calculated from measurements of MCA OD.
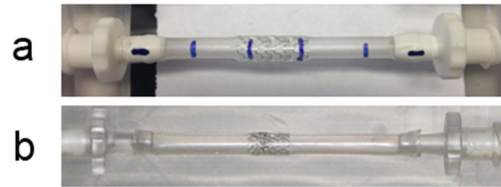
Figure 3.5 Stent expansion in mock coronary arteries (a) WE43 stent (b) 316L stent

Test 3: Cyclic Strain Amplitude

The cyclic strain amplitude supported by expanded stents in MCAs was assessed, as shown in Figure 3.6. A static pressure head was applied to each stented MCA by elevating a tank of non-corrosive solution to a predetermined height. The tank was connected to the stented MCA using silicone tubing and luer lock fittings. Each stented MCA was subjected to three pre-conditioning pressure cycles (0 to 120 mm Hg). The OD of the stented MCA was recorded at eight separate locations while under the influence of three different static pressure loads, namely: 0, 80 and 120 mm Hg. Cyclic strain amplitude was calculated as the % change in the average OD of the stented MCA between a pressure of 80 mm Hg and 120 mm Hg.
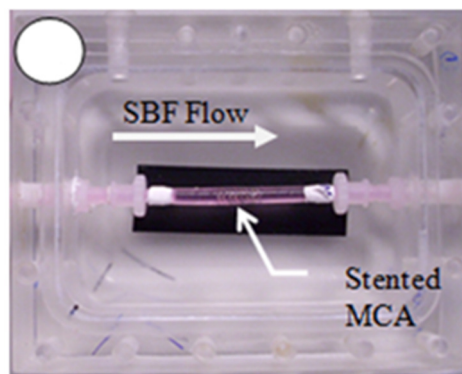
Figure 3.6 Stented mock coronary artery under the influence of static pressure head during the experiment performed to measure cyclic strain amplitude

3.4　Corrosion Experiments

The corrosion behaviour of dogbone and stent specimens was characterised through two independent immersion corrosion experiments performed in SBF, as detailed in Table 3.1. A total of eighty four dogbone specimens and twenty one stents were prepared for corrosion testing by laser cutting and finished using the surface treatments described in section 3.2.

Expt.	Specimen type	Purpose of Expt.	No. of specimens	Analyses/Results
A	Dogbone	Establish the dominant corrosion processes and specimen corrosion rate. Examine the effect of plastic strain on the corrosion process. Determine the effect of corrosion on the specimen mechanical integrity.	Total=84, 28 (PS=0%) 28(PS=2.4%) 28(PS=8.4%)	SEM, EDX, Mass loss, tensile tests
B	Stent	Establish the dominant corrosion processes and stent corrosion rate. Examine the effect of deployment strain on the stent corrosion process. Determine the effect of corrosion on the radial stiffness of the stent.	21 WE43	SEM, PCM, Mass loss, compression tests

Table 3.1 Details of the experiments performed (PCM: phase contrast microscopy)

The main purpose of Experiment A was the determination of the influence of plastic strain on the corrosion behaviour of the alloy. The corrosion rates, the dominant corrosion processes and the temporal corrosion-induced reduction in the mechanical integrity of the specimen were determined. Specimen mass loss was obtained by gravimetric measurements performed using a semi-microbalance having a resolution of 0.01 mg (Sartorius RC210P). The results of a preliminary corrosion experiment indicated a maximum specimen mass loss of almost 100% after 10 days of immersion. Assuming the requirement of having 500 increments (1 increment = 0.01 mg) of measurement available within the expected experimental mass loss range, a specimen gauge region with a mass of approximately 5 mg was deemed suitable. As WE43 had a relative density of 1.84, the corresponding volume

in the specimen gauge region was 2.73 mm^3. The wall thickness of the specimen was the same as that for the finished stent. In accordance with ASTM standard E8, which requires a minimum gauge length (L) to width (W) ratio of four for pin-loaded tensile specimens, an L/W ratio greater than five was selected in this case. Thus, the finished dogbone specimen, which is shown in Figure 3.7(a), had a gauge region with a length of 10.05 mm, (unfurled) width of 1.85 mm, wall thickness of 0.14 mm and a total surface area of 40 mm^2. It is noted that the L/W ratio used in this work is similar or greater to those of previous studies involving tensile testing of sub-size metal specimens (Jain et al., 2008; Raulea and Goijaerts, 2001). Thickness measurements of the gauge region, performed using a SEM, verified that a uniform specimen wall thickness was obtained from the surface treatments. The average roughness (Sa) of outer specimen surfaces was 0.17 μm, as measured using AFM.

In order to investigate the influence of plastic strain on corrosion behaviour, three groups of dogbone specimens were prepared, each subjected to a different magnitude of plastic strain, namely: 0%, 2.7% and 8.4%. Specimens having 0% plastic strain required no deformation. The other specimens were mounted in custom grips in a tensile testing machine (Z005, Zwick Roell) and extended for a time of 10 seconds by either 4% or 10% of their original length using a crosshead speed of 0.5 mm/min, as indicated by the stress-strain curves shown in Figure 3.7(b). At peak extension the direction of crosshead travel was reversed in order to permit elastic recoil of the specimen and the test was terminated when the load cell recorded zero force. In this way, the specimens were subjected to a loading cycle analogous to that induced in stent struts (loading and elastic recoil) during the deployment process. After recoil, the plastic strain (PS) for the specimen groups (mean ± SD) was 2.66 ± 0.03% and 8.38 ± 0.02%; for simplicity these specimen groups were named 2.7% PS and 8.4% PS, respectively. The tab regions on each specimen were coated with an epoxy resin to limit corrosion to the test region.
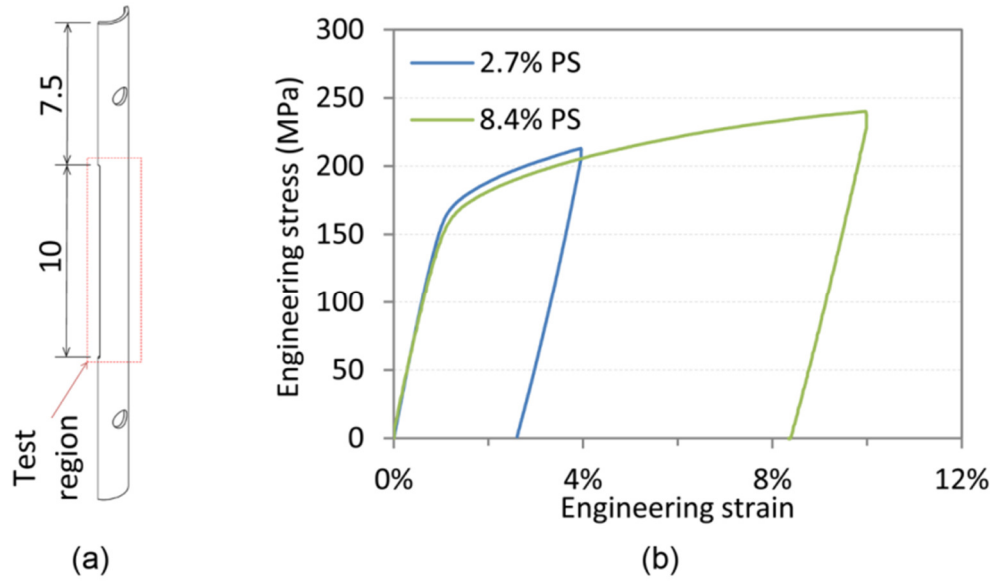
Figure 3.7 (a) The dogbone specimen geometry (b) Representative stress-strain response of dogbone specimens during the application of plastic strain

The main purpose of Experiment B was to determine the corrosion rate for expanded WE43 stents and to determine the influence of corrosion on the radial stiffness of the stent. Each stent was mounted (uncrimped) on a 3.5 x 18 mm angioplasty balloon, freely expanded to a maximum balloon pressure (15 atm) consistent with clinical deployment of magnesium stents (Erbel et al., 2007) and then permitted to undergo elastic recoil.

Prior to corrosion testing, stent and dogbone specimens were stored in a desiccator for 24 hours to ensure consistent oxidisation of all surfaces and then sterilised by exposure to ultraviolet irradiation for 2 hours. Specimens were mounted on a stage (Multiclip, Struers) so that all test region surfaces were exposed to the solution. Each specimen was placed in a separate container with 25 ml Hank's balanced salt solution (H8264, Sigma Aldrich) and the screw cap of the container was left slightly open in order to allow gaseous exchange with the environment. The ratio of solution volume (ml) to exposed specimen surface area (cm^2) was 63:1 and 32:1 for dogbone and stent specimens, respectively; well above the minimum ratio

recommended for magnesium alloys (Yang and Zhang, 2009). Since corrosion phenomena in magnesium alloys are sensitive to variations in environmental conditions such as temperature (Kirkland et al., 2010), solution pH (Ng et al., 2010) and biological contaminants, the corrosion studies were performed under sterile conditions in an incubator (Nuaire NU-5500E) that provided temperature uniformity ($37 \pm 0.2°C$) and a humidified gas environment (5% CO_2 and 95% air) for increased pH buffering capacity.

The pH of the SBF was recorded at regular time intervals (pH 213, Hanna Instruments) and maintained within a physiologically-relevant range of values (6.3– 7.8) as described in previous studies involving similar alloys and solutions (Bowen et al., 2013). Specimens were removed at various intervals of time, cleaned in a solution of 10% chromic acid (27081 Sigma-Aldrich) at 55°C in order to remove corrosion products and weighed using a semi-microbalance. For each interval of time four dogbone specimens (n=4) and three stents (n=3) were used. Corrosion surfaces were imaged under the SEM. The thickness of corroded struts was measured at 30 separate locations under the SEM, from which the mean strut width was calculated. EDX analysis was used to determine the elemental composition of the corrosion products and surfaces. Specimens were imaged in solution using a phase contrast microscope (PCM) (Olympus CK30) in order to observe the evolution of H_2 gas bubbles.

Mechanical strength testing was performed to determine the influence of corrosion on the mechanical integrity of the specimens. For dogbone specimens, uniaxial tensile testing was carried out to failure in one loading cycle using a materials testing machine (Z005, Zwick Roell) with a 5 kN load cell. A pre-load of 0.5 N and a crosshead speed of 0.5 mm/min were used. Tests were terminated when the load dropped below 70% of the maximum load value. Specimen elongation was determined from crosshead travel, rather than from local deformation at the test

region of the specimen. Specimen stresses were calculated based on the original specimen cross-section and so the changes in cross-section due to necking and corrosion were not accounted for; this approach having been used previously in similar studies (Bowen et al., 2012). Engineering stress-strain curves were produced for each specimen. The elastic modulus (E), 0.2% offset yield strength (σ_y) and ultimate tensile strength (UTS) were calculated in accordance with ASTM E111-04 using the TestXpert software package (V11.02). The value of strain at the UTS and at failure was termed the ultimate strain (ε_u) and failure strain (ε_f), respectively. The radial stiffness of stents, defined as the change in resistive force for an applied 10% reduction in stent diameter, was evaluated by compressing freely expanded stents between the platens of a materials testing machine (Zwick Z005) using a 500 N load cell, a preload of 0.02 N and a cross-head speed of 0.2 mm/min. Again, the 316L stent was tested for comparison. Data were normalised for the 316L stent in order to account for the difference in original length between the 316L and WE43 stent and, curves were presented as stent reaction force versus stent compression.

3.5   Corrosion Modelling

A FE based plastic strain mediated phenomenological corrosion model, which was capable of modelling the uniform micro-galvanic corrosion of a 3-D metallic stent structure, was developed in order to assess the performance of a corroding WE43 alloy stent. The model was used to predict the effects of diffusion-controlled corrosion in elastic-plastic metals and, was calibrated through corrosion experiments that established the plastic strain-mediated input corrosion rates for the material of interest. The corrosion model was written in ANSYS parametric design language (APDL), as shown in Appendix A.3 and, was developed for use with the commercial ANSYS Implicit FE code. APDL is a scripting language specific to ANSYS that facilitates automation of common tasks, parameterisation of models and, allows the use of other sophisticated features, such as optimisation techniques (Ansys, 2010).

57

The corrosion model developed represents a modification of the CDM model proposed by Gastaldi et al. (Gastaldi et al., 2011) which allows the effects of corrosion-induced micro-scale geometric discontinuities on overall specimen mechanical integrity to be accounted for, without explicitly modelling their progression. However, in this study, a discrete rather than continuum modelling approach was adopted. A flowchart outlining the operation of the corrosion model is shown in Figure 3.8. After the solution to an initial analysis was obtained (stent deployment and recoil), the results data, which included the magnitude of the first principal plastic strain, ε_{p1}, in each element, was written to arrays in preparation for corrosion simulation. Element connectivity was determined and the elements on the corrosion surface were identified. The material behaviour of each element was initially modelled by a single elastic-plastic material model that was representative of the mechanical properties of the material prior to the onset of corrosion.

The loss of mechanical integrity due to the corrosion process, denoted by the damage parameter, D, was calculated on an element-by-element basis through a modified version of the damage evolution law described by Gastaldi et al (Gastaldi et al., 2011). The temporal value of the damage parameter, D, was calculated over a discrete volume of material governed by the element size, L_e and, over a discrete time-step, Δ_t. When L_e and Δ_t were sufficiently small; the damage parameter at a fixed time, D_e, was given by the relation:

$$D_e = D_{e-1} + \frac{\delta_u}{L_e} k_u \varphi_e \Delta_t \, \kappa_e \qquad (3.4)$$

where δ_U and L_e were respective material and FE model characteristic lengths, in units of mm, and k_u was a corrosion kinetic parameter, in units of h^{-1}, as described previously in (Gastaldi et al., 2011).
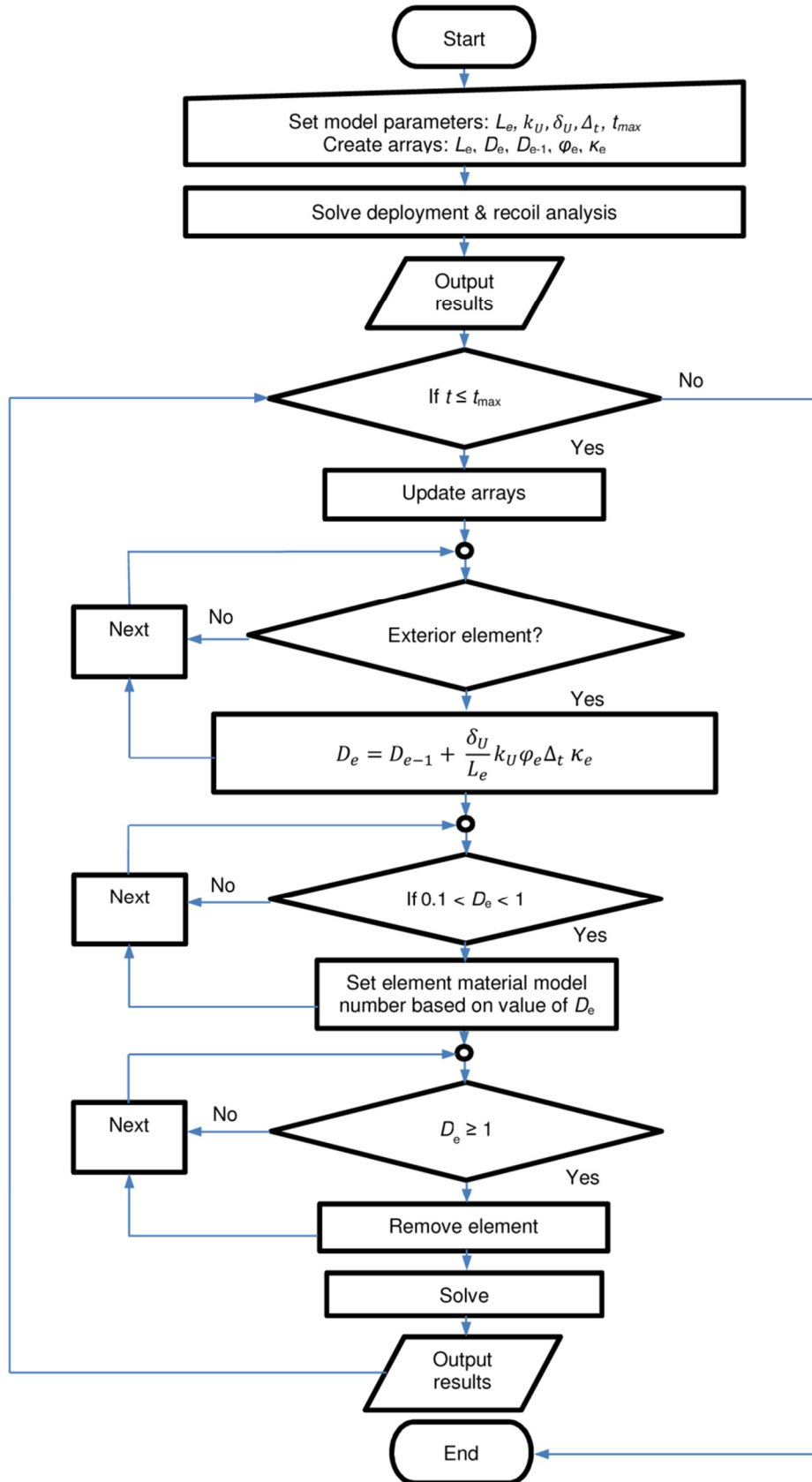
Figure 3.8 Simplified flowchart of the corrosion model process

An element-specific dimensionless plastic strain parameter, φ_e, was introduced in this work in order to account for the effects of plastic strain-induced corrosion in the modelling framework. The value of φ_e for each element was dependent on both the magnitude of elemental ε_{p1} and the simulated corrosion time, t, and was estimated from a table of values that were established in the experimental corrosion tests described in section 3.4.

Depending on the number of element faces (NEF) that were exposed to the corrosion environment, the element damage calculated at each time step was modulated by an element-specific exposure parameter, κ_e. κ_e was a simple scaling parameter that was derived from a linear approximation of the slope of the curve that described the rate of diffusion through a brick element when NEF varied from one to six, as shown in Figure 3.9. κ_e was included in the modelling framework in an attempt to model the rounding of initially sharp strut corners which can be expected for a diffusion-dominated corrosion process (Ulvrová et al., 2012).
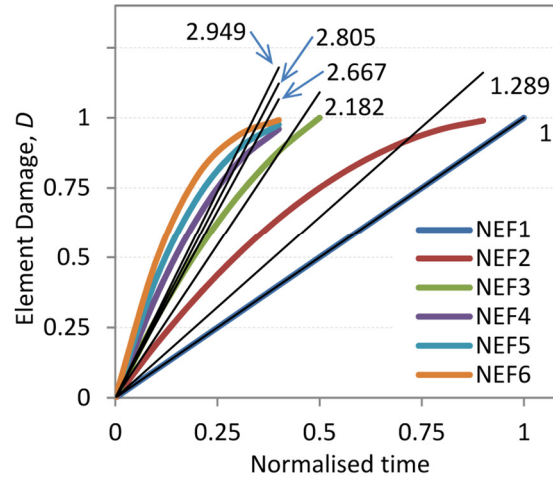
Figure 3.9 The possible values for the element exposure parameter, κ_e, that were used to scale the element damage calculated at each time step

When the damage parameter, D, reached or exceeded certain threshold values, the mechanical integrity of the element was reduced by modifying its

material model. In this way, the gradual corrosion-induced reduction in the mechanical integrity of the elements was modelled. When the damage parameter reached a critical value (D=1), the element was assumed to have completely corroded and was eliminated from the model. The newly exposed element surface beneath the eliminated element became part of the exposed surface and was thus subject to corrosion in the next iteration of the model. The model iterated until the simulated corrosion time, t, reached the user-defined maximum solution time, t_{max}.

3.5.1 Corrosion Model Calibration

The corrosion model was calibrated based on the results of experiment A. As the corrosion-induced material loss observed in the experiments was relatively uniform in both the longitudinal and radial directions of the test region, repetitive and reflective symmetry simplifications were assumed and only a one-quarter slice of the dogbone specimen was modelled, as shown in Figure 3.10(a). A representation of the test region in the specimen, which was modelled as being flat rather than curved, was meshed with enhanced strain formulation brick elements, as shown in Figure 3.10(b). Symmetry boundary constraints were applied to the nodes on the two symmetry edges of the model. Nodes on the upper and lower surfaces of the model were constrained only in the direction of loading which permitted lateral constrictions as would be expected under uniaxial tensile loading. All nodes on the top surface were coupled in the direction of loading to a master node and a force was applied to this master node in order to simulate the tensile test.

In representing the deformation of the material in the FE model, finite deformation kinematics was assumed. The initial mechanical properties were based on those of non-corroded WE43 dogbone specimens with 0% plastic strain, as determined from the uniaxial tensile tests described in section 3.4. Accordingly, elasticity was considered linear and isotropic in terms of finite deformation quantities

61

with E = 13 GPa. Material plasticity was described by a multi-linear isotropic hardening material model, in accordance with previous FE studies which used similar material models (Gastaldi et al., 2011; Wu et al., 2011), with σ_y = 160 MPa, UTS = 245 MPa and ε_u = 0.17. Poisson's ratio had a value of 0.3 (Wu et al., 2010).
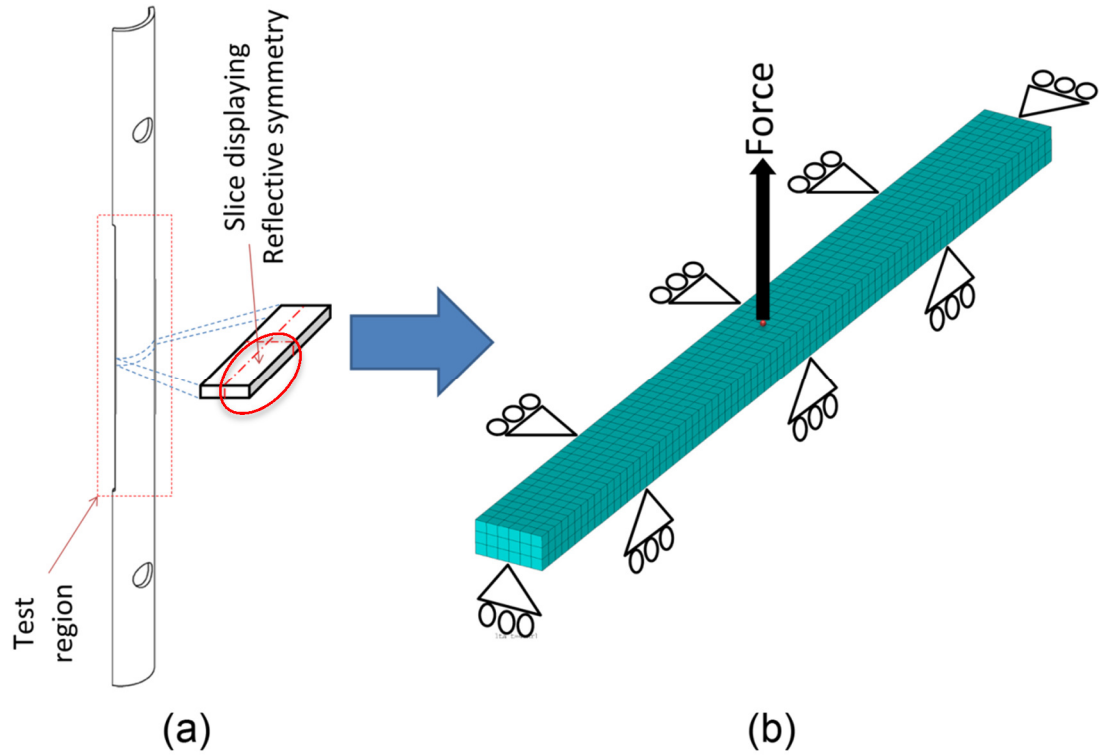
Figure 3.10 (a) slice of dogbone specimen test region exhibiting repetitive and reflective symmetry (b) boundary and loading conditions used for the FE simulations

The material properties of damaged elements were controlled through the evolution of the damage parameter, *D*. The corrosion-induced reduction in the mechanical integrity of the material, observed in the experiments, was characterised in the model by modifying the material model of the elements at certain threshold values of *D*. Ten material models were used to represent the material properties of elements with *D* values ranging from 0 to 1, in increments of 0.1, as shown in Figure 3.11. For the stress-strain curves shown, it was assumed that the reduction in the load-bearing capacity of the element was directly proportional to the mass lost to corrosion. Therefore, the curves were produced by scaling the stress component of

curve for the WE43 material by factors ranging from 0.9 to 0.1 in increments of 0.1.
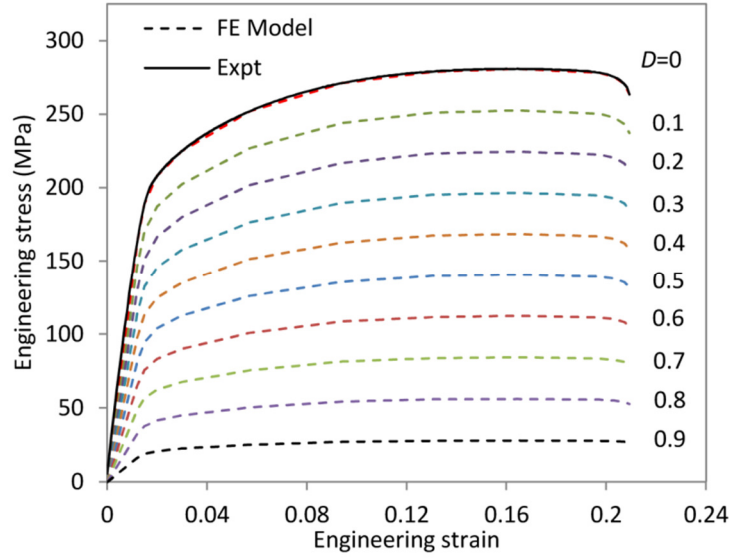
Figure 3.11 FE material model input used to represent the stress-strain properties of elements with D *values ranging from 0 to 0.9*

Experiment A was modelled by simulating tensile loading and elastic recoil of the test region in order to induce the required magnitude of ε_{p1} (0%, 2.7% and 8.4%). Corrosion was then permitted to occur on exposed surfaces in the test region. The rate of mass loss over time was determined based on the average damage value (*D*) over all of the model elements. The maximum force withstood by the model was taken as a measure of loss in mechanical integrity. In calculating the stress-strain response of the model to tensile loading, the engineering stress was calculated based on the original cross-section of the specimen in order to facilitate comparison with the experimentally measured response.

The material characteristic length, δ_U, was given a value of 0.015 mm, consistent with grain sizes observed in metallographic analysis of WE43 tubes. The slope of the mass loss curves from experiment A was used to generate a table of φ_e values for the three plastic strain magnitudes examined, as shown in Table 3.2. By interpolating between the data points in the table, a φ_e value was calculated for each

element based on the magnitude of ε_{p1} in the element and simulated corrosion time.

Time	Plastic strain magnitude		
(h)	0	2.7%	8.4%
0-24	0.368	2.190	5.830
24-48	1.287	1.265	1.264
48-96	1.000	0.632	0.630
96-144	1.035	1.092	1.149
144-192	0.862	1.149	1.093
192-240	0.785	1.095	1.483

Table 3.2 The table of values established in experiment A from which the strain parameter, φ_e, was calculated in the FE corrosion model

In calibrating the FE corrosion model, the values of the independent model parameters k_u, L_e and Δ_t were determined for given values of δ_U, φ_e and κ_e, based on the simulation of experiment A. These values were determined by imposing three conditions. First, the predicted temporal mass loss curves should match that observed in experiment A. Second, the simulated corrosion-induced reduction in specimen mechanical integrity should match that observed experimentally. Third, the model should predict the corrosion rates observed in experiment A, thus allowing the parameter k_U to be determined. These conditions allowed the determination of suitable element length (L_e = 0.012 mm) and time step (Δ_t = 1 h) values through an iterative calibration process, as shown in the convergence study in Appendix A.4.1.

In order to validate the predictive capabilities of the corrosion model for the calibrated parameters, the corrosion of the dogbone specimens observed in experiment A was simulated. Loading and elastic recoil of the sample in uniaxial tension was simulated followed by the subsequent corrosion of the specimen under the influence of 0%, 2.7% and 8.4% plastic strain. Model predictions were compared to the experimental results.

3.5.2 Stent Model

The calibrated corrosion model was used to predict the corrosion performance of the absorbable magnesium stent. The design and geometry of the stent were taken directly from the experiments, as shown in Figure 3.12(a). The stent geometry, which exhibited rotational and circumferential symmetry, as well as periodicity in the longitudinal direction, was represented by a repeating unit cell (RUC) model that was meshed with 91,320 brick elements, as shown in Figure 3.12(b). The RUC method is an established technique which can be used to reduce model size and solution time in the numerical analysis of models balloon-expandable stents (Ju et al., 2008; Li et al., 2009; Xia et al., 2007). The element type and material models used for the stent were the same as those described earlier for the dogbone specimen model in section 3.5.1.

In order to reduce the computational cost of modelling the interaction of the balloon and stent, spring elements were incorporated to simulate the constraint of the balloon using an established technique (Early et al., 2009; Zahedmanesh et al., 2010). The springs had multi-linear stiffness and were attached to the nodes on the inner surface of the stent. The springs had low stiffness (1×10^{-7} N/m) until the stent reached nominal diameter at which point the stiffness increased sharply (0.1 N/m) to inhibit further stent expansion. Periodic boundary conditions were imposed on the symmetry planes of the unit cell in the rotational and longitudinal directions using nodal displacement constraint equations, as outlined in (Xia et al., 2007). A suitable average element size (L_e = 0.012mm) and time step (Δ_t = 1 hour) was established by means of a convergence study in which predicted nodal displacement, element stress and strain, mass loss and stent radial stiffness results were all converged to within 2%, as shown in Appendix A.4.2. Based on the selected L_e, the corrosion model parameters were scaled accordingly. Stent material properties were taken to be the same as those used in the dogbone specimen models (see Figure 3.11).
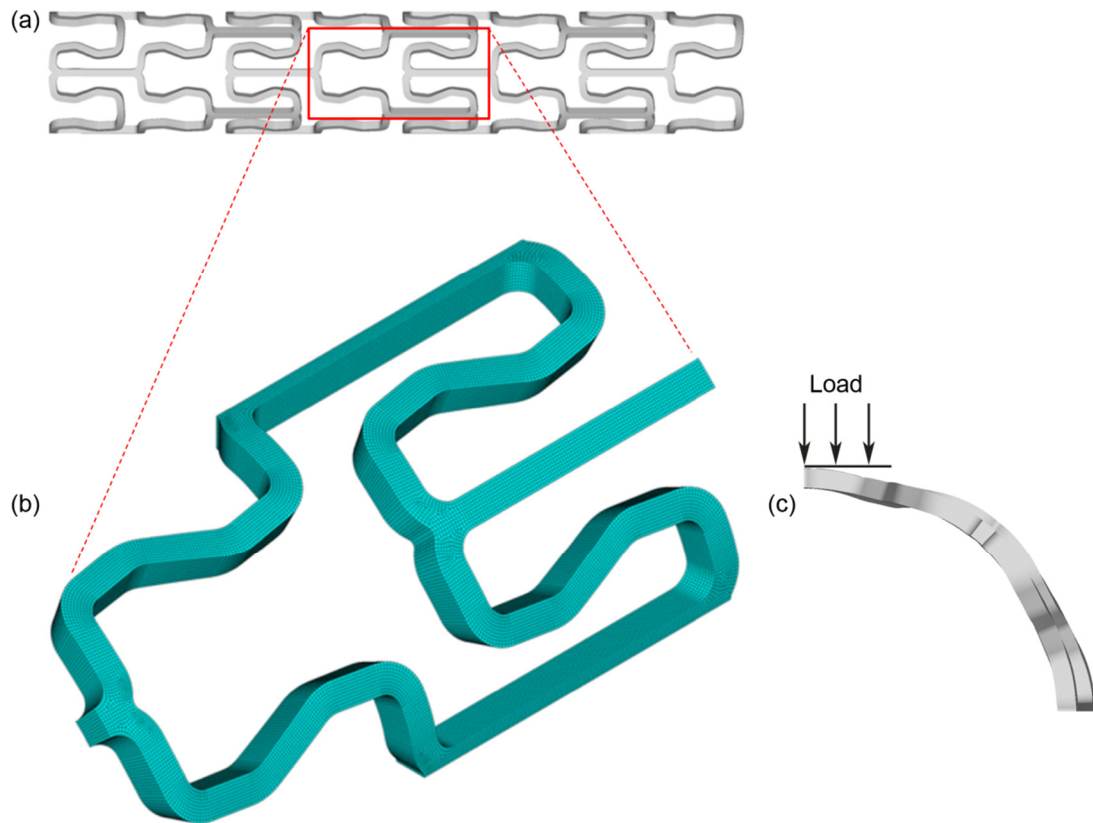
Figure 3.12 (a) Image of the full stent geometry with a repeating unit cell (RUC) indicated (b) The geometry of the FE RUC model prior to deployment (c) Loading applied to contact elements in order to predict the radial stiffness of the stent

The deployment of the uncrimped stent, by way of free expansion, was simulated through the application of a uniform linearly-increasing radial pressure at the internal surface of the stent. When the outer diameter of the stent reached a value similar to that measured experimentally, the pressure load was reduced to zero in order to simulate elastic recoil. The rate of mass loss was determined based on the average damage value (D) over all of the model elements. At 20 hour intervals of simulated corrosion time, a flat analytical surface comprising of contact elements, was brought into contact with the outer surface of the stent and was used to compress the stent in the same manner as that used in the experiments, as shown in Figure 3.12(c). Again, the radial stiffness of the stent was calculated as the change in resistive force for an applied 10% reduction in stent diameter.

Stent Model Calibration

Based on the mass loss curves obtained experimentally for plastic strain values of 0%, 2.7% and 8.4%, the corrosion model predicted the value of φ_e for each element by interpolating, for the ε_{p1} value in the element, between the data points of the experimental curves. However, preliminary stent deployment simulations showed that a small proportion of the elements (typically less than 4%) had ε_{p1} values, ranging from 8.4% to 27%, that were outside the range measured experimentally, as shown in the distribution plot in Figure 3.13(a). In order to investigate the relationship between ε_{p1} and φ_e for these elements, two different corrosion models were developed. In the linear plastic strain (PS) corrosion model, a linear relationship was assumed between ε_{p1} and φ_e above ε_{p1} values of 8.4%. In the plastic strain corrosion model, a non-linear relationship was assumed, where φ_e increased sharply for elements with ε_{p1} values above 8.4%; with substantially higher φ_e applied when ε_{p1} exceeded the engineering strain observed experimentally at the UTS (~20%). For both models, the results predicted for mass loss and radial stiffness were compared to the experimental data in order to determine the model that gave the best correlation.
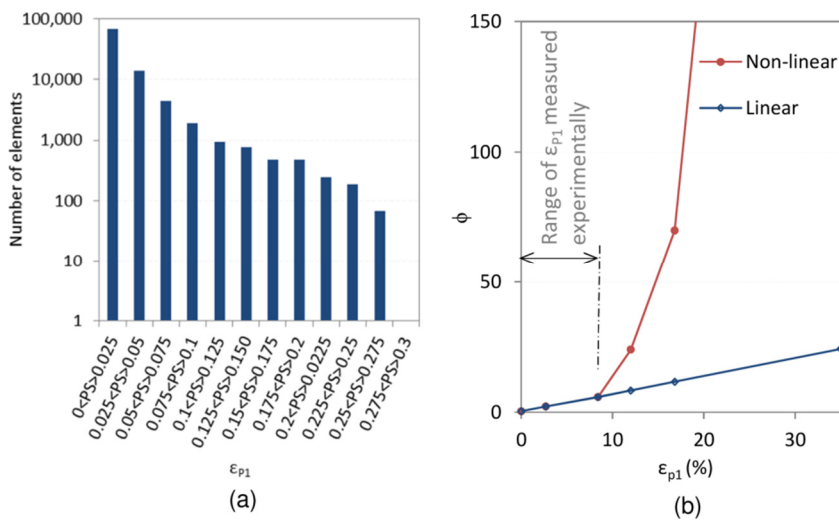
Figure 3.13 (a) Distribution of the elemental ε_{p1} values for the stent model (b) Linear and non-linear models used to represent the dependency of φ_e on elemental ε_{p1}

4. Results

4.1 Stent Manufacture

4.1.1 Laser Cutting

Laser cutting of WE43 tubes produced parts with substantial dross and spatter attachment (see Figure 3.2). Dross may form during laser cutting when a significant temperature gradient exists between the top and bottom surface of the work-piece. This results in a greater amount of material being melted on the underside of the work-piece. The low viscosity and low surface tension of melted magnesium also may have contributed to the spatter attachment observed. Excessive amounts of dross and spatter attachment on the inner surface of the tube prevented the normal fallout of cut sections. Therefore, machining parameters were optimised for cutting the material including the laser power, pulse repetition frequency, pulse width, laser wavelength and cutting speed, as shown in Table 4.1.

Laser machining parameter	Optimised setting
Laser power (W)	24
Pulse repetition frequency (Hz)	6000
Pulse width (µs)	14
Laser wavelength (nm)	1070 ± 5
Cutting speed (mm/sec)	1

Table 4.1 Optimised laser machining parameters for cutting WE43 tube

Nitrogen was selected as an inert shield gas in order to minimise oxidation and gas pressure was increased to improve the quality of the cut and to reduce dross accumulation. The focal position of the laser beam was adjusted to increase the kerf width and hence aid fallout of cut sections. Optimisation of laser parameters successfully reduced dross and spatter adherence. The remaining dross was removed by a combination of chemical and plasma etching processes.

4.1.2 Chemical and Plasma Etching

There was an observable difference in the surface texture of inner and outer surfaces which appeared to originate from the extrusion process used to produce the tubes. Outer surfaces had the smoothest appearance while inner surfaces appeared marginally rougher. Surfaces produced by laser cutting had the roughest appearance. Chemical etching with phosphoric acid removed bulk dross and surface scale from all stent surfaces. A layer of material measuring approximately 5 µm was removed, as measured under SEM. The texture of all stent surfaces was significantly improved to a more uniform morphology, as shown in Figure 4.1. Significant variation was evident in the surface texture of inner, outer and laser cut surfaces after chemical etching. A significant amount of residue and contamination remained on the stent surfaces following the chemical etching process, as shown in Figure 4.1.
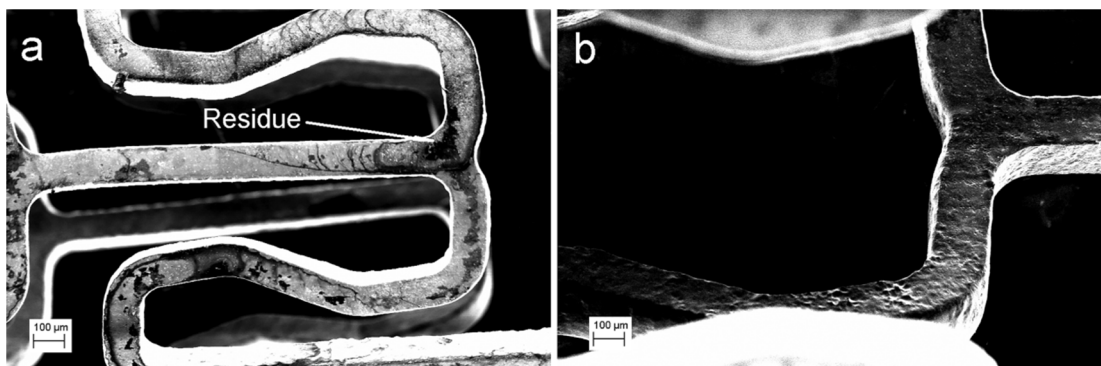
Figure 4.1 Stent surfaces resulting from chemical etching: (a) outer stent surface with residue (dark areas), and (b) inner surface of stent strut

Plasma etching and cleaning was employed in order to remove the surface deposits and contamination that remained from the chemical etching process. SEM and photographic images of a finished stent are shown in Figure 4.2 and Figure 4.3, respectively. It can be seen that plasma etched surfaces appeared lighter in colour compared to chemically etched surfaces and residues were completely removed.

69

Plasma processing reduced surface roughness of all surfaces compared to chemically etched surfaces. The plasma etching process was most effective on the outer surface and less effective on shadowed surfaces and laser cut edges, as shown in Figure 4.2. Plasma etching was performed in three stages where the specimens were manually rotated in increments of 120° on the quartz plate in order to minimise shadowing effects. Although RIE acts mainly as a "line-of-sight" process, it is likely that a significant number of ions would have reached the inner stent surfaces owing to the small strut width (120 μm), the comparatively large spacing between the struts, and the high sheath potential (~495 V). The specimen rotation technique employed here would have limited efficacy in reducing the shadowing effects. A planetary rotating system would provide a more effective method to minimise shadowing effects through continuous specimen rotation during plasma processing.

The etch rate of the 90% Ar and 10% O_2 plasma process was not measured as it was beyond the scope of this work. However, one would expect a significantly higher etch rate for the WE43 alloy when compared to relatively harder traditional stent materials such as stainless steel (316L), cobalt-chromium alloys and titanium alloys. Etch rates of 20 to 30 nm/min in 100% Ar plasma have been reported for pure magnesium (Nishimoto, 2003) and MgO thin films (Kim and Kim, 2007). These studies used higher power settings (300 - 500 W) and higher proportions of Ar compared to those used in this work. The use of comparatively lower power settings and a lower proportion of Ar in this study suggest etch rates well below 20 nm/min for the WE43 alloy material. Therefore, one may expect that a layer of material no more than 0.3 μm thick was removed from the stent with a processing time of 10 minutes.
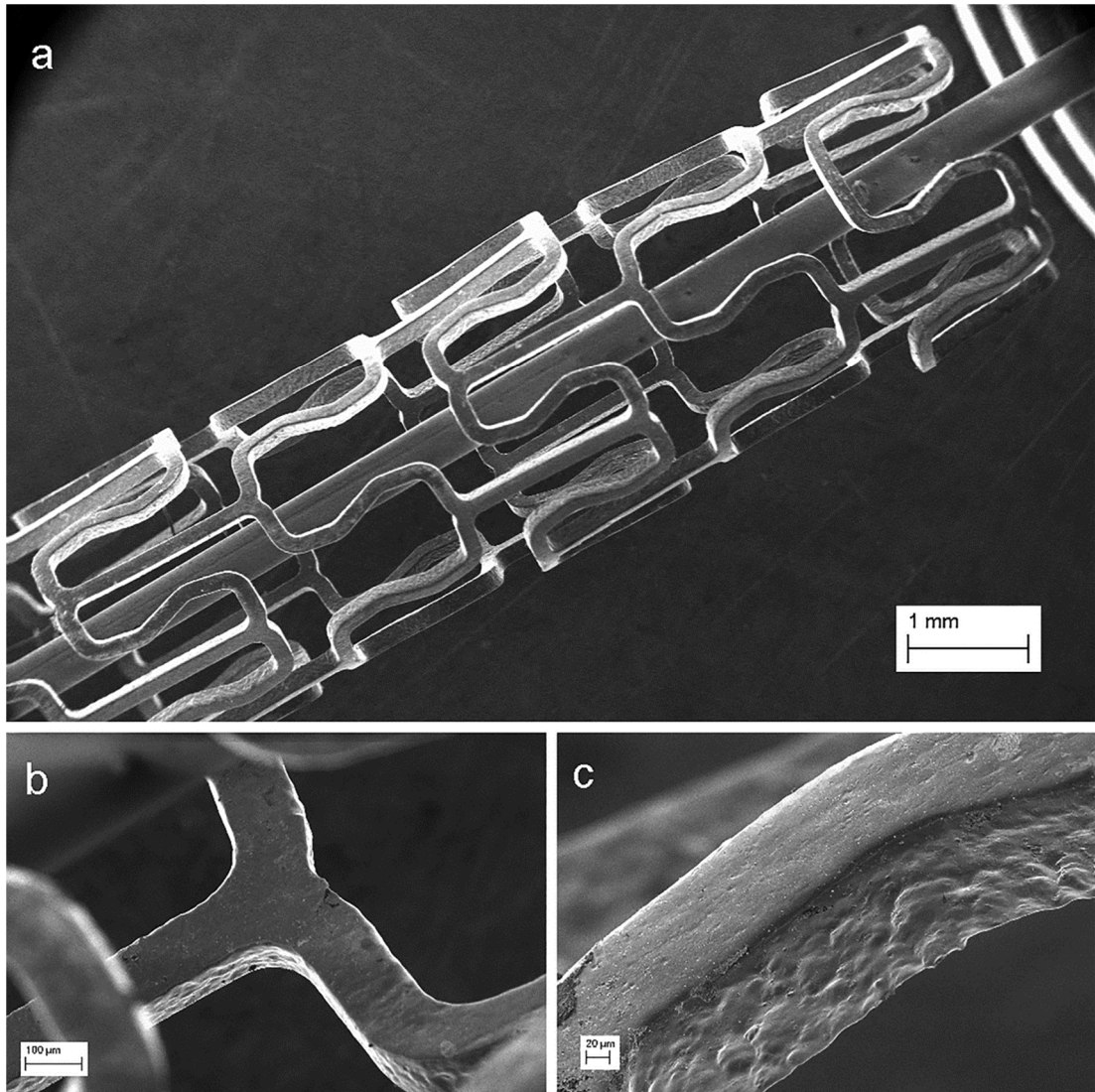
Figure 4.2 SEM images of a finished stent following plasma etching and cleaning: (a) stent mounted on fused silica tube, (b) inner surface, and (c) outer surface
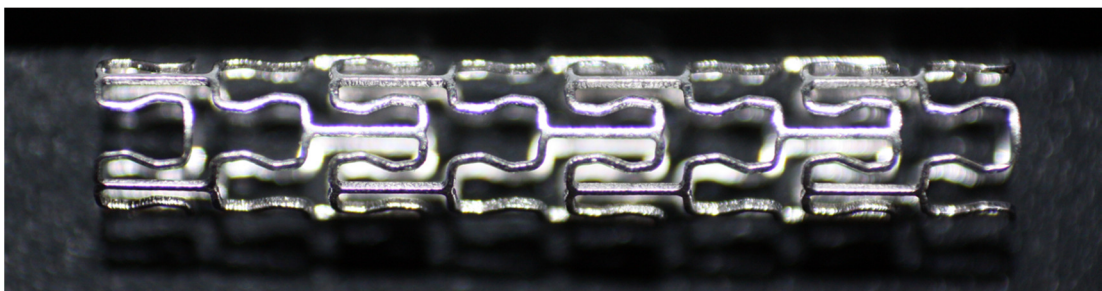
Figure 4.3 Image showing a finished WE43 stent

4.1.3 Surface Characterisation

Surface Chemistry

Figure 4.4(a) shows that the as-received specimens had a relatively rough surface morphology that consisted mainly of a dark-coloured magnesium (Mg) matrix area (α-phase) interspersed with lighter-coloured β-phase areas (Hänzi et al., 2009). The chemical compositions of both the α-phase and β-phase regions of the specimen were measured by EDX at three different sites. Figure 4.4(a) shows the sites where spectra were taken for α-phase (S1-S3) and β-phase (S4-S6) measurements. The weight percent (%) of each element detected at the three sites was averaged (mean) in order to produce the plot shown in Figure 4.4(b). The error bars were calculated as the standard deviation in order to represent the overall distribution of the data. It should be noted that, as with many EDX systems, the system used in this work had inherent difficulty measuring light elements owing to low fluorescence yield, absorption and peak overlaps with heavier elements (Berlin, 2011). Therefore, the readings for C and O obtained by EDX in this work should be disregarded.
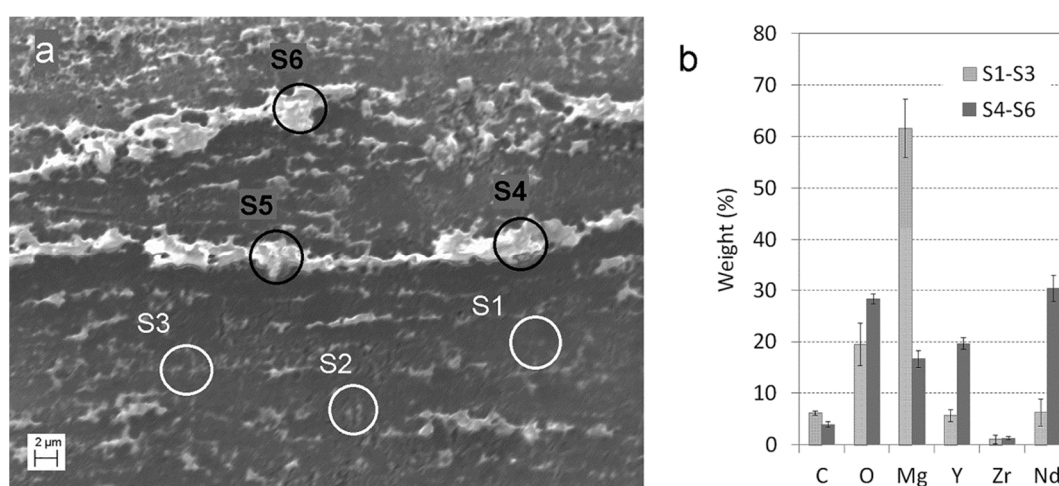
Figure 4.4 (a) Typical surface morphology of as-received specimen showing spectra sites S1-S6, and (b) average chemical composition at spectra sites S1-S3 and spectra sites S3-S6

EDX analysis confirmed the α-phase had high concentrations of Mg (62%) and low concentrations of distributed alloying elements Y (5.6%), Nd (6.2%) and Zr (1.0%) along with O_2 (19.4%) and C (6.1%). Conversely, the surface of the secondary phase areas had low Mg (16.7%) and relatively higher concentrations of alloying elements Y (19.6%), Nd (30.3%) and Zr (1.3%) along with O_2 (28.3%) and C (4.0%). A detailed characterisation of the microstructure of a similar wrought WE43 alloy is given in (Coy et al., 2010).

Chemical etching in phosphoric acid resulted in significant changes in the appearance and surface chemistry of the specimens. The native oxide layer was replaced with a more passive oxide layer with lower porosity and increased corrosion resistance. The surface morphology was more homogenous owing to the lower porosity of the new oxide layer, as shown in Figure 4.5(a). EDX analysis showed that the new surface layer consisted of Mg (91.3%), Y (0.8%), Zr (0.1%), O_2 (6.0%) and C (0.6%) and small amounts of Na (1.0%) and P (0.1% – 0.85%). It is believed that the presence of P in the surface layer can be attributed to the formation of magnesium phosphate during etching (Gray-Munro et al., 2009). The presence of Na in the surface layer may be attributed to the formation of a thin layer of sodium hydroxide that is adsorbed to the specimen during the neutralisation treatment.

A number of rectangular-shaped entities were distributed within the surface layer of the chemically etched specimens, as shown in Figure 4.5(a). An EDX spectrum at S2 showed that these entities were rich in the RE elements Y (80.3%), Nd (9.9%) and Zr (0.8%). The dark surface deposits shown in Figure 4.5(b) consisted mainly of O_2 (46-48%), Na (19.7-28.5%), P (18-25.1%) and Mg (1-10%). These heavy deposits were likely to have been oxides with P and NaOH content as this would account the high O_2 content observed at these sites.
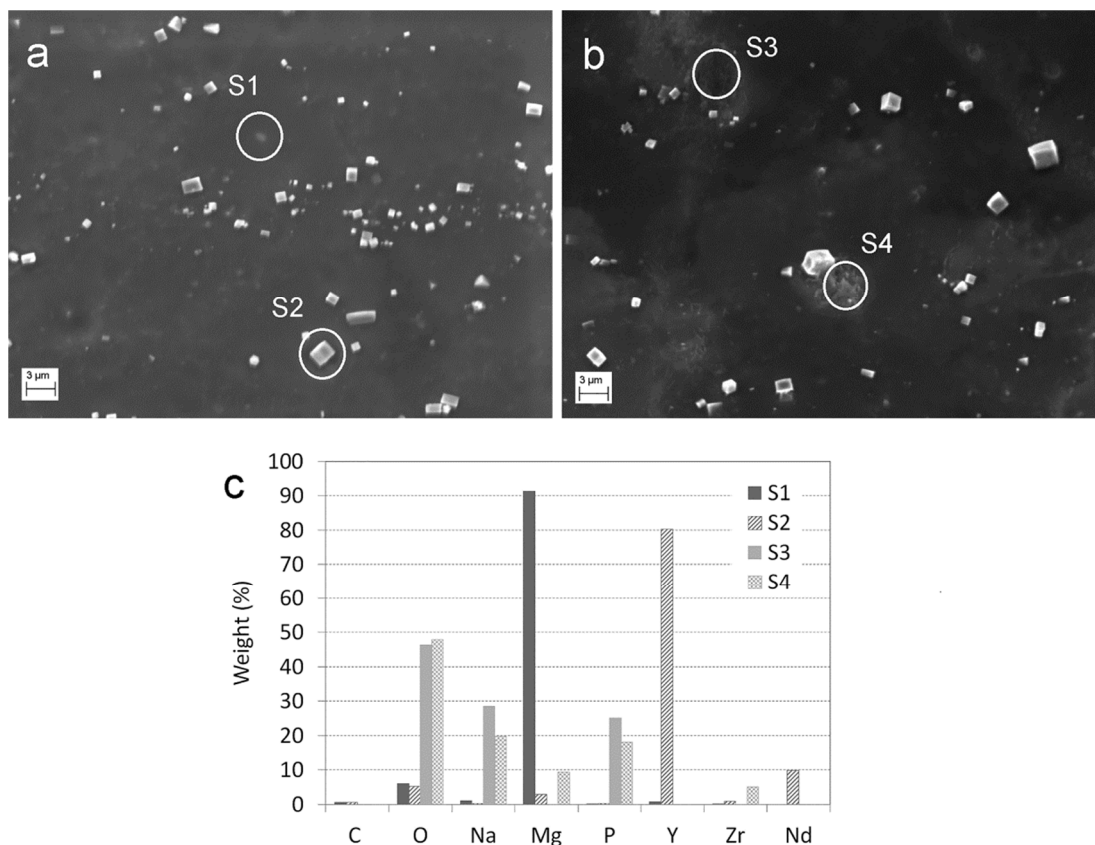
Figure 4.5 Typical surface morphology of chemically etched specimen: (a) normal surface appearance, (b) dark area with surface residue, and (c) chemical composition of surface at spectra sites S1-S4

Plasma etching successfully removed unwanted surface deposits and residue, as shown in Figure 4.6(a). EDX analysis showed lower concentrations of P and Na on plasma etched surfaces compared to chemically etched surfaces, as shown in Figure 4.6(b). These results suggest that the heavy Ar ions in the plasma may have removed some of the phosphor-rich coating. The amount of material removed from the surface can easily be reduced by shortening the treatment time or by increasing the ratio of O_2 to Ar in the gas mixture.
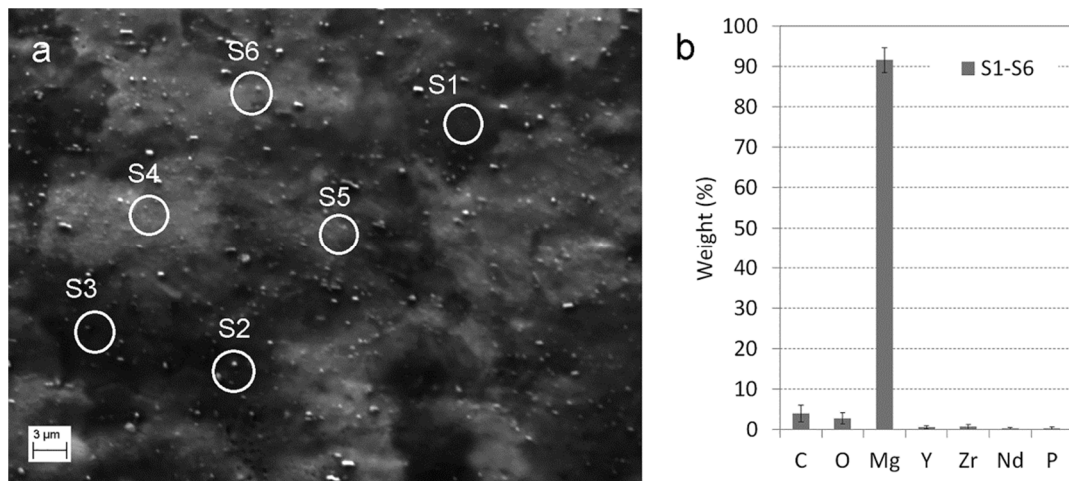
Figure 4.6 (a) Typical surface morphology of plasma etched specimen showing EDX spectra sites S1-S6, and (b) average chemical composition of surface at spectra sites S1-S6

Surface Roughness

Figure 4.7 shows the surface morphologies measured by AFM for the as-received, chemically etched and plasma etched specimens. Figure 4.8 shows average surface roughness values (Sa) for the same three specimen conditions. It was found that plasma etched specimens had the lowest surface roughness (172 nm) compared to chemically etched (191 nm) and as-received (223 nm) specimens. A one-way analysis of variance (ANOVA) showed that the mean surface roughness amongst the three specimen groups (as-received, chemically etched and plasma etched) was statistically significant ($F_{(2,6)} = 5.14$, $p = 0.006$).
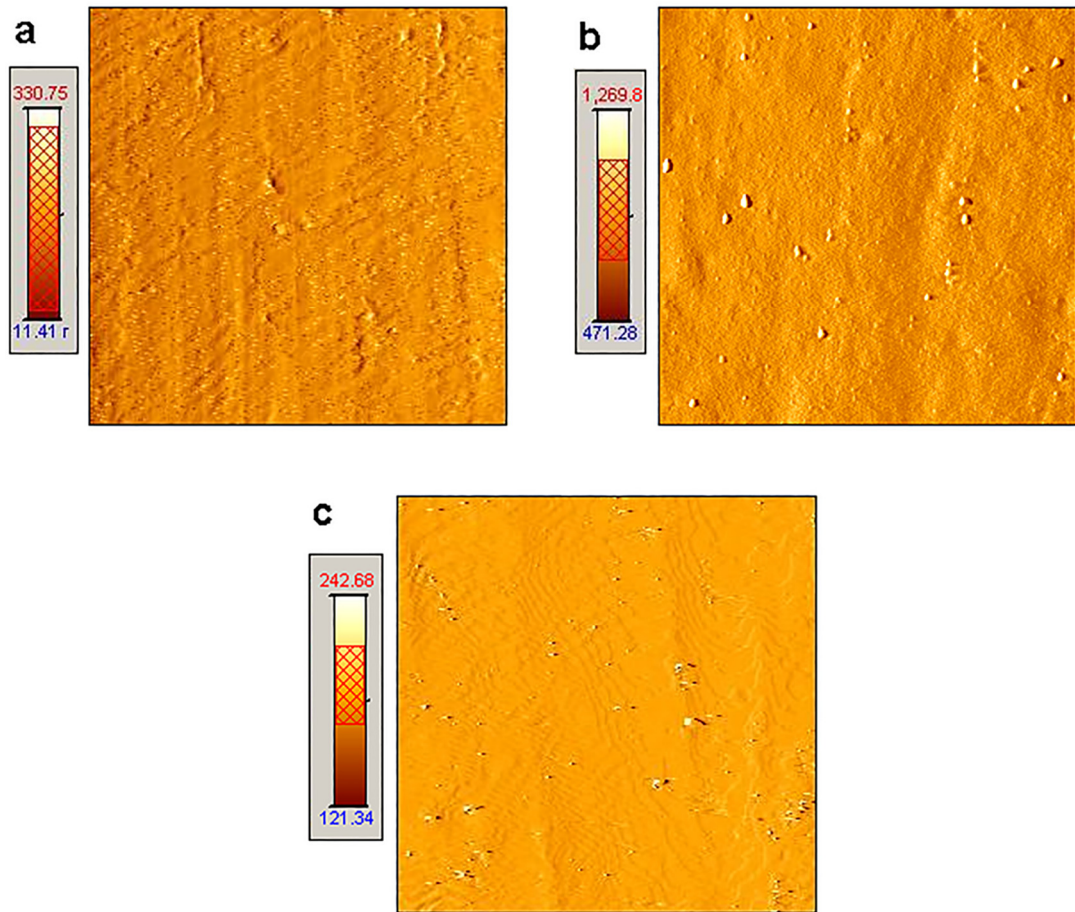
Figure 4.7 Typical surface morphology of specimens generated by AFM: (a) as-received, (b) chemically etched, and (c) plasma etched
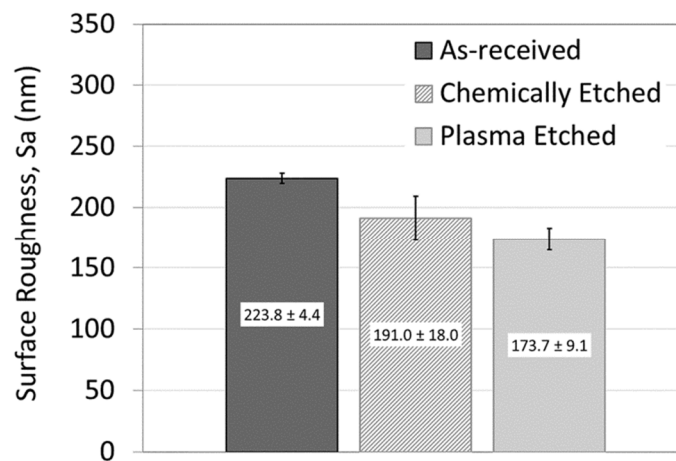
Figure 4.8 Surface roughness (Sa) values (mean ± standard deviation) measured by AFM for as-received, chemically etched and plasma etched tube specimens

The tubes used in this work were subjected to an annealing process. The average surface roughness (Sa) was relatively high in the as-received condition owing to the non-uniform morphology during the tube extrusion process. Figure 4.9(a) shows the parallel lines and defects that ran longitudinally on the surface indicating the direction of the tube extrusion process. These defects were potential sites of stress concentration and material failure due to crack growth during stent expansion. The chemical and plasma processing steps ware intended to minimise these defects. The surface texture was considerably improved by chemical etching which reduced the Sa value by 14.7% from 223 nm to 191 nm. No surface defects were evident on the surface layer that was produced by chemical etching, as shown in Figure 4.9(b). The plasma etched surface was considerably brighter in appearance compared to the surfaces of the other two specimens, as shown in Figure 4.9(c). The average surface roughness of plasma treated specimens (172 nm) was 10% lower compared to chemically etched specimens (191 nm).
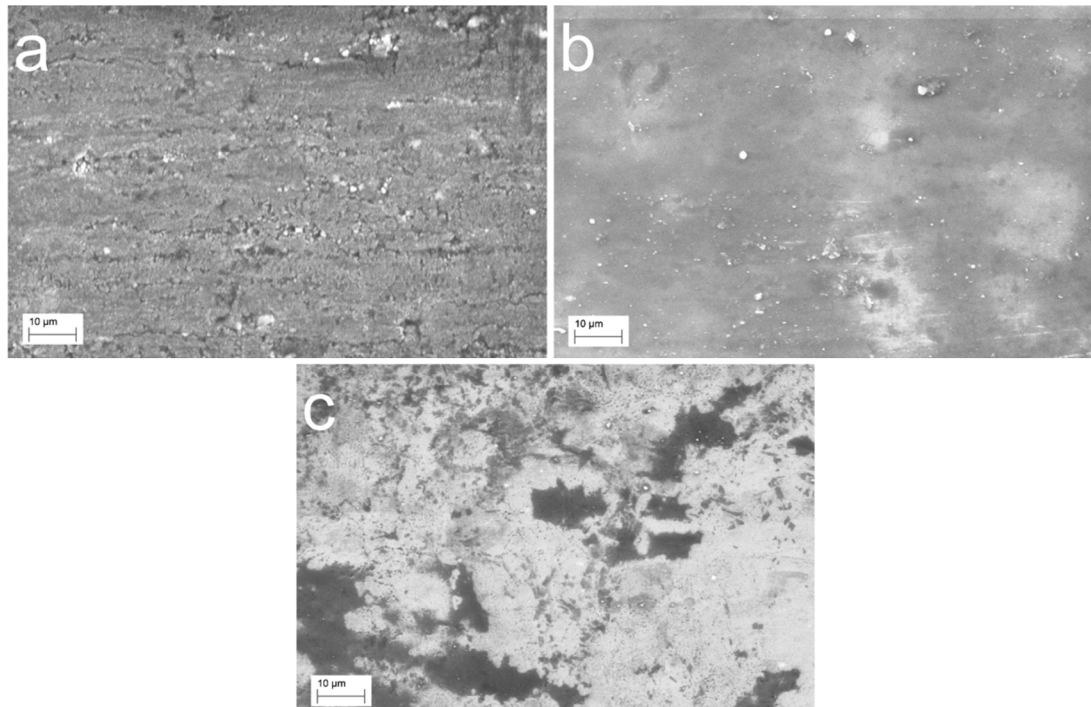
Figure 4.9 SEM images of tube specimens: (a) as-received, (b) chemically etched, and (c) plasma etched and cleaned (magnification = 1000x)

4.2   Mechanical Testing

In the first test, free expansion of the WE43 stent occurred mainly between balloon pressures of 1 atm and 3 atm, while the equivalent range for the 316L stent was between 2 atm and 6 atm, as shown in Figure 4.10(a). Owing to high stent compliance, the proximal and distal ends of the WE43 stent flared significantly at low balloon pressure thus contributing to the rapid increase in ID observed. At the maximum balloon pressure of 15 atm, the average ID for WE43 (4.01 mm) was 9% greater than for 316L (3.68 mm). The inset in Figure 4.10(a) shows the typical deformed geometry of a WE43 stent at three different phases of the free expansion procedure, namely: unexpanded, fully expanded and after elastic recoil. ERR for WE43 (4.4%) was higher compared to the 316L stent (3.6%), as shown in Figure 4.10(b). FS was significantly lower for WE43 (0.84%) compared to 316L (3.55%). Negative DB was greater for WE43 (-2.4%) compared to 316L (-0.52%), thereby indicating a larger central ID than distal ID at maximum balloon pressure, for both stent types.

In the second test, WE43 and 316L stents were expanded inside MCAs, as shown in Figure 4.10(c). Stent metrics were calculated based on measurements of MCA OD as the stent ID could not be accurately measured by visualisation. Compared to free expansion results in the first test, higher ERR and lower DB values were recorded for both stent types, as shown in Figure 4.10(b), owing to the presence of the MCA which applied an inward-acting radial force to the stent. Compared to the first test, FS values were higher for WE43 and lower for 316L stents when deployed in MCAs.

In the third test, under the influence of sequential static physiological pressure loads (80 & 120 mm Hg), the MCA that was stented with a WE43 stent exhibited a cyclic strain amplitude (0.72 %) that was approximately 2.5 times greater

than for the 316L stented MCA (0.29%), as shown in Figure 4.10(d). This finding suggested that the MCA exhibited significantly greater compliance when stented with the WE43 stent compared to the 316L stent.

The surfaces of deployed stents were examined by SEM and there was no evidence of strut failure or cracking, as shown in Figure 4.11(d).
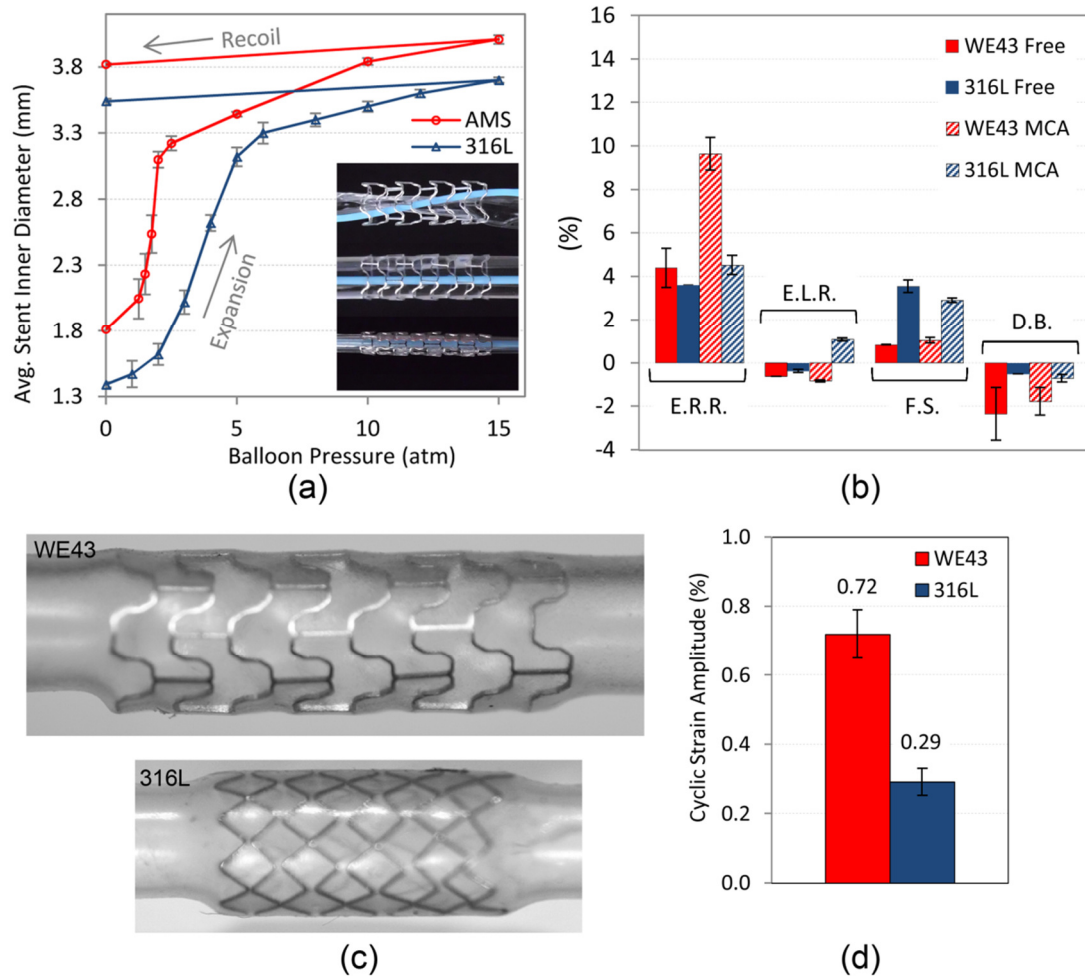
Figure 4.10 (a) Pressure-diameter curves for freely expanded stents. Inset: WE43 stent shown unexpanded, fully expanded and after recoil, (b) performance metrics for the free expansion and expansion in MCA of stents, (c) WE43 stent (top) and 316L stent (bottom) and (d) cyclic strain amplitude results. Error bars represent one standard deviation of uncertainty.
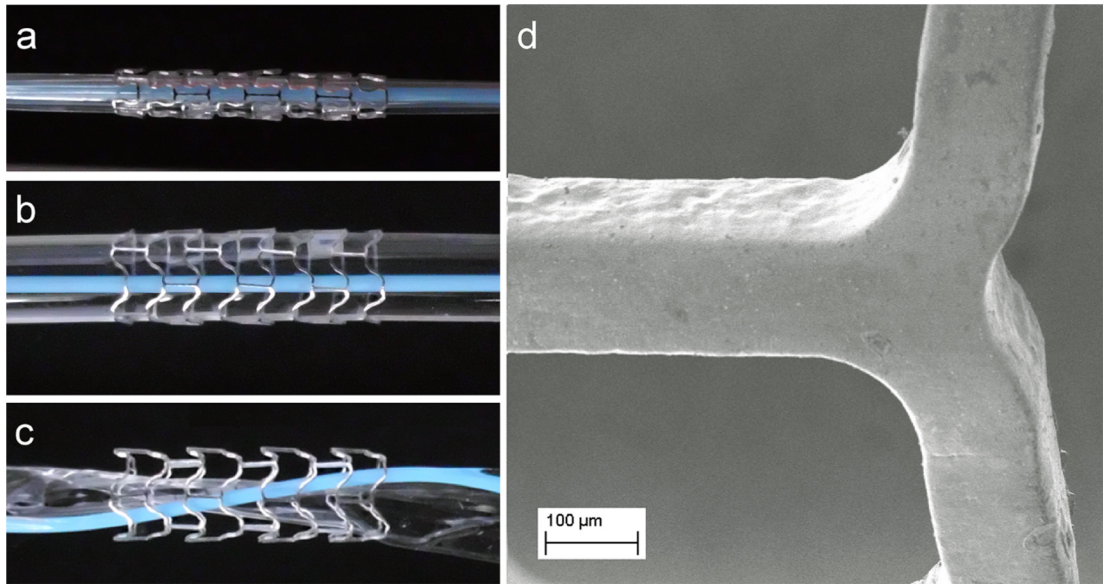
Figure 4.11 Expansion testing of WE43 stent: (a) unexpanded, (b) fully expanded (c) after recoil (d) SEM image of a strut section from an expanded stent

4.3   Corrosion Experiments

Based on the results of experiment A, the mass lost over time by the three groups of dogbone specimen is shown in Figure 4.12. It can be seen that the rate of mass loss increased for specimens with greater levels of plastic strain. Specimens with 0% plastic strain exhibited a relatively low rate of mass loss for the first 1 d of immersion; however, it increased thereafter to give a steady rate of mass loss from which an average corrosion rate of 0.021 mg cm^{-2} h^{-1} was derived. For specimens with plastic strain, higher rates of mass loss were observed for the first 1 d immersion, which slowed significantly between 2 d and 4 d. Beyond 4 d, specimens with 2.7% and 8.4% plastic strain exhibited relatively stable rates of mass loss from which average corrosion rates of 0.025 mg cm^{-2} h^{-1} and 0.027 mg cm^{-2} h^{-1} were derived, respectively.

SEM images, displaying typical surfaces on the inner walls of dogbone specimens with 0% plastic strain, are shown in Figure 4.13. The surface morphology produced by the surface treatments on a finished specimen, prior to immersion

testing, is shown in Figure 4.13(a). It can be seen that the magnesium matrix material was uniformly removed by chemical etching but some intermetallic precipitates were visible in the surface layer. After 1 d immersion, microscopic pits were observed on this surface layer, as shown in Figure 4.13(b). Wide, shallow corrosion pits, surrounded by elevated regions of darker material, were observed on the surface after 3 d immersion, as shown in Figure 4.13(c). The pits increased in size and number over time and thus coalesced and advanced over large regions of the surface, as shown in Figure 4.13(d).
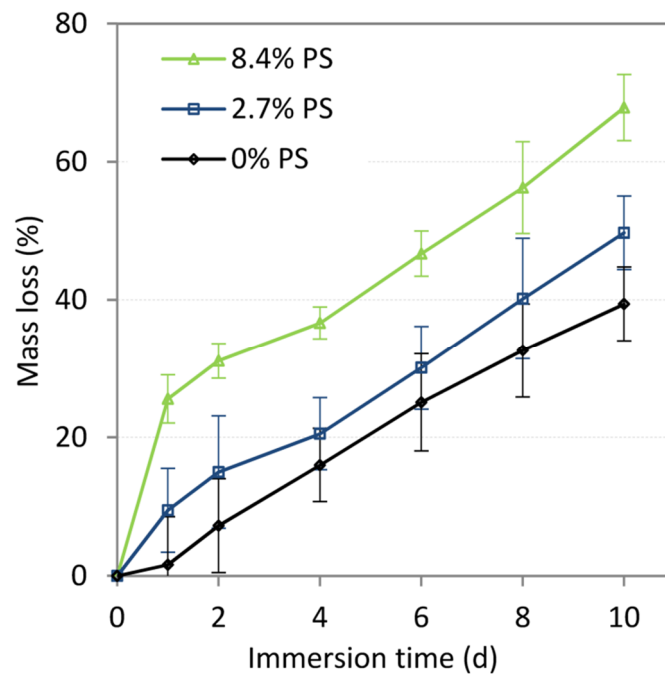
Figure 4.12 Plot of percentage mass lost over time by dogbone specimens based on the results of experiment A. Error bars represent a single standard deviation from the mean.

The composition of the material in the corrosion pits, as determined by EDX analysis, was consistent with that of the magnesium matrix of the alloy. The elevated regions were rich in RE elements (Zr, Y and Nd) and had compositions that were consistent with the β-phase and other intermetallic compounds for the WE43 alloy. Pitting corrosion of the magnesium matrix, at the interface with the β-phase,

led to the undermining and fall-out of β-phase particles, as shown in Figure 4.13(e). Corrosion attack was observed to progress in a layer by layer manner and thus, a relatively uniform specimen morphology resulted after 10 d immersion, as shown in Figure 4.13(f). When the inner and outer walls of the specimen were compared, corrosion attack on laser cut edges resulted in a different morphology, as shown in Figure 4.13(g).
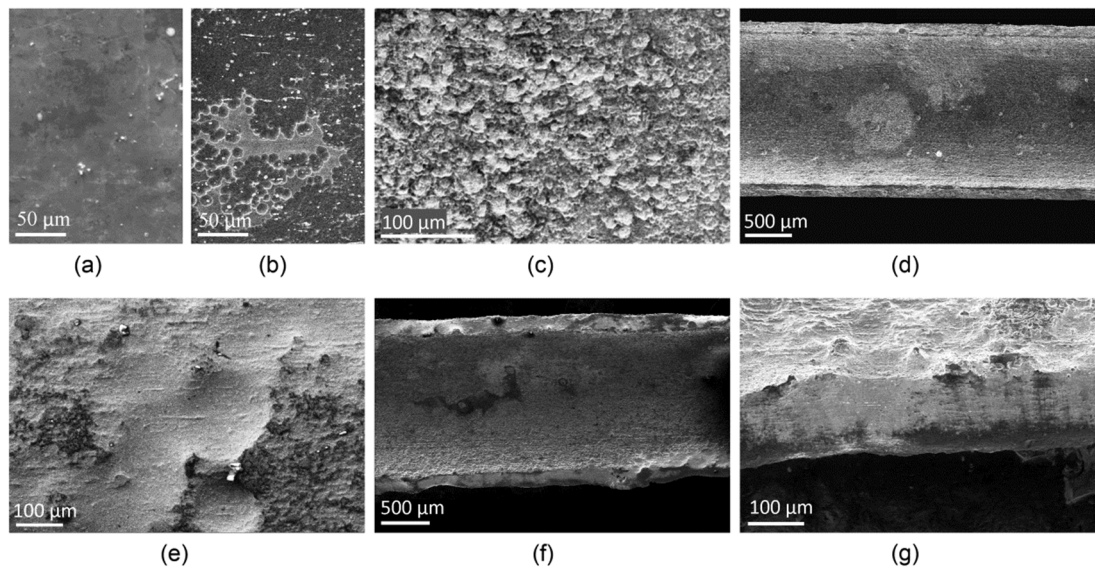
Figure 4.13 SEM images of dogbone specimens with 0% PS following immersion in solution for (a) 0 d, (b) 1 d, (c) 3 d, (d) 3 d (e) 10 d, (f) 10 d and, (g) 10 d

The corrosion processes observed for specimens with plastic strain was similar to that described above for specimens with 0% plastic strain. However, specimens with plastic strain exhibited significantly more advanced pitting corrosion attack after just 1 d, and some cracks were observed, as shown in Figure 4.14(a). Further, the corrosion layer on these specimens displayed many cracks and had a significantly rougher appearance, as shown in Figure 4.14(b). As a result, pitting corrosion of the magnesium matrix and the undermining of β-phase particles progressed at an accelerated rate, as shown in Figure 4.14(c). Compared to 0% plastic strain specimens, corrosion attack after 10 d immersion was greater for

specimens with 2.7% plastic strain, as shown in Figure 4.14(d) and significantly greater for specimens with 8.4% plastic strain, as shown in Figure 4.14(e). Corrosion attack on the laser cut edges was also more pronounced for specimens with plastic strain. This may be attributed to a number of influences at the specimen edge surfaces such as deformation-induced residual stresses and the influence of processing (laser cutting and surface treatments) on the composition, microstructure and crystallographic orientation of the material.
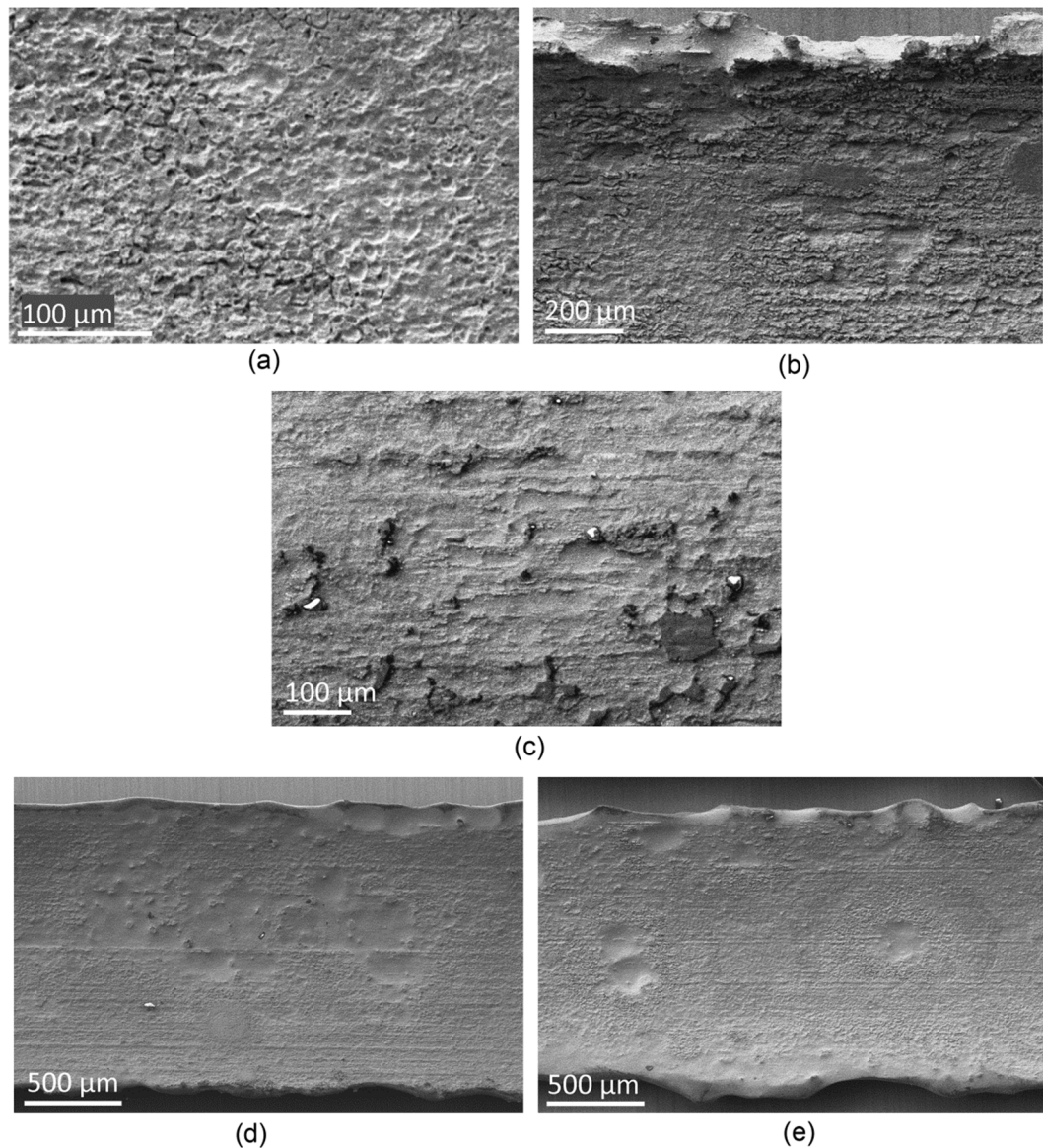
Figure 4.14 SEM images of dogbone specimens with 2.7% PS following immersion in solution: (a) 1 d, (b) 6 d, (c) 10 d, (d) 10 d and, (e) 10 d (8.4%PS)

83

Based on the SEM images and the uniform nature of the corrosion observed, it is suggested that localised micro-galvanic corrosion may be the dominant corrosion processes in this case. The differences in the surface morphology and mass loss rates for specimens with plastic strain suggests that plastic strain had a significant influence on the corrosion behaviour. Plastic strain likely resulted in significant damage to the brittle surface oxide thus allowing corrosion attack to occur immediately after immersion in the solution and to progress at an accelerated rate. The cracking observed on the surface might be attributed to material damage induced by the application of plastic strain, and the influence of hydrogen embrittlement and SCC. The application of plastic also likely led to deformation-induced acceleration in galvanic corrosion processes within the alloy.

Stress-strain curves with error bars representing 95% confidence intervals are shown in Appendix A.2 for specimens with 0%, 2.7% and 8.4% plastic strain. For simplicity, representative stress-strain curves are shown in Figure 4.15(a-c) for specimens with 0%, 2.7% and 8.4% plastic strain, respectively. Specimen strength, as determined by dividing the maximum load withstood by the specimen in tension by the original specimen cross-sectional area, was seen to decrease significantly for both immersion time and increasing plastic strain, as shown in Figure 4.15(d). Similarly, there was a consistent reduction observed in E, σ_y and ε_u for increasing immersion time and for increasing plastic strain, as shown in Figure 4.15(e-g). The plastic strain induced prior to corrosion testing led to work-hardening and hence an increase in the initial σ_y of the 2.7% and 8.4% plastic strain specimen series which decreased with immersion time, as shown in Figure 4.15(g).
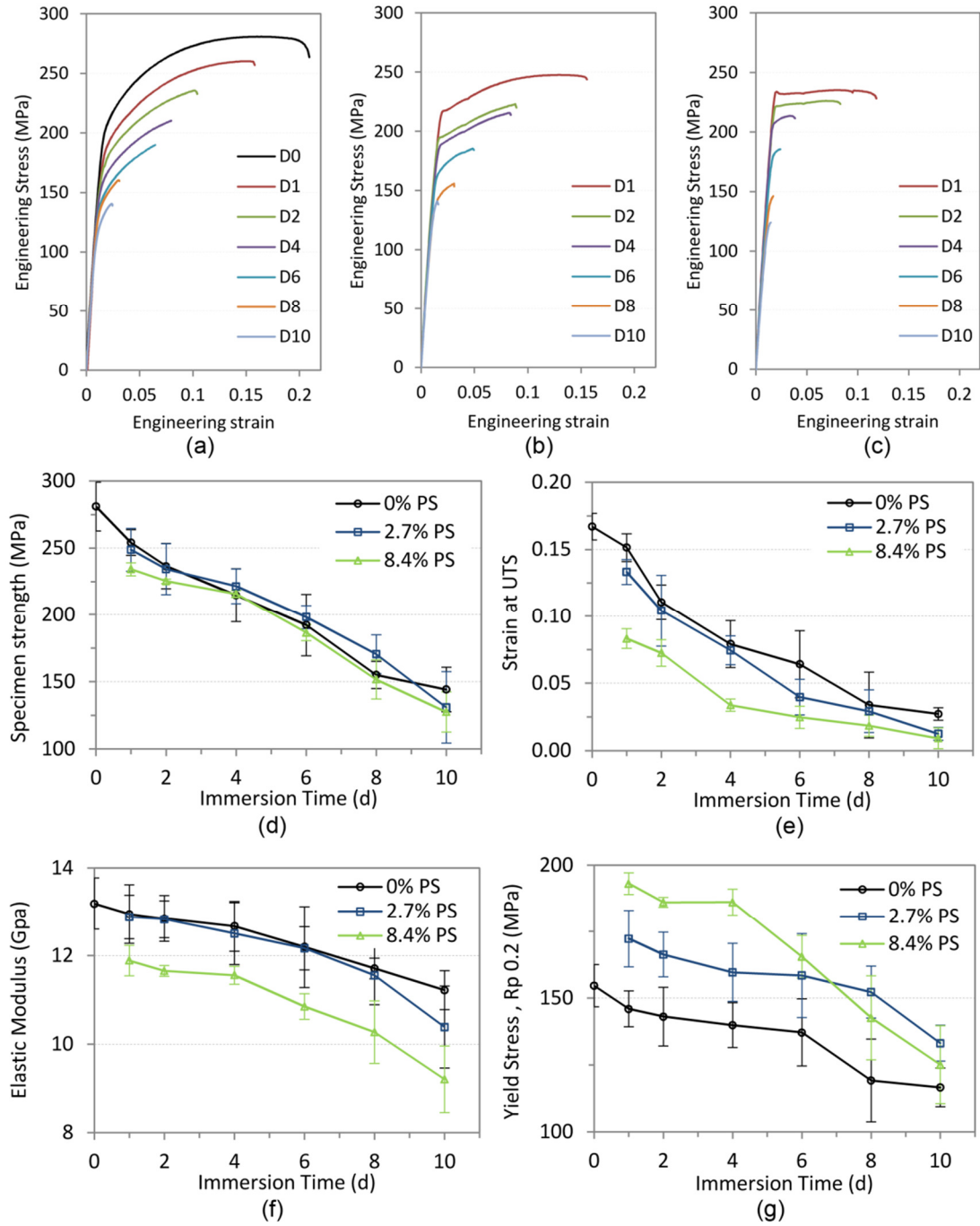
Figure 4.15 Representative stress-strain curves for dogbone specimens based on the results of experiment A, (a) 0% PS (b) 2.7% PS and (c) 8.4% PS. Mechanical properties of dogbone specimens over time: (d) UTS, (e) ε_u, (f) E and (g) σ_y. Error bars represent one standard deviation of uncertainty.

SEM images of fractured dogbone specimens following tensile testing are shown in Figure 4.16 (a-d). It can be seen that, compared to the non-corroded specimen, the corroded specimens display more brittle type of fracture.
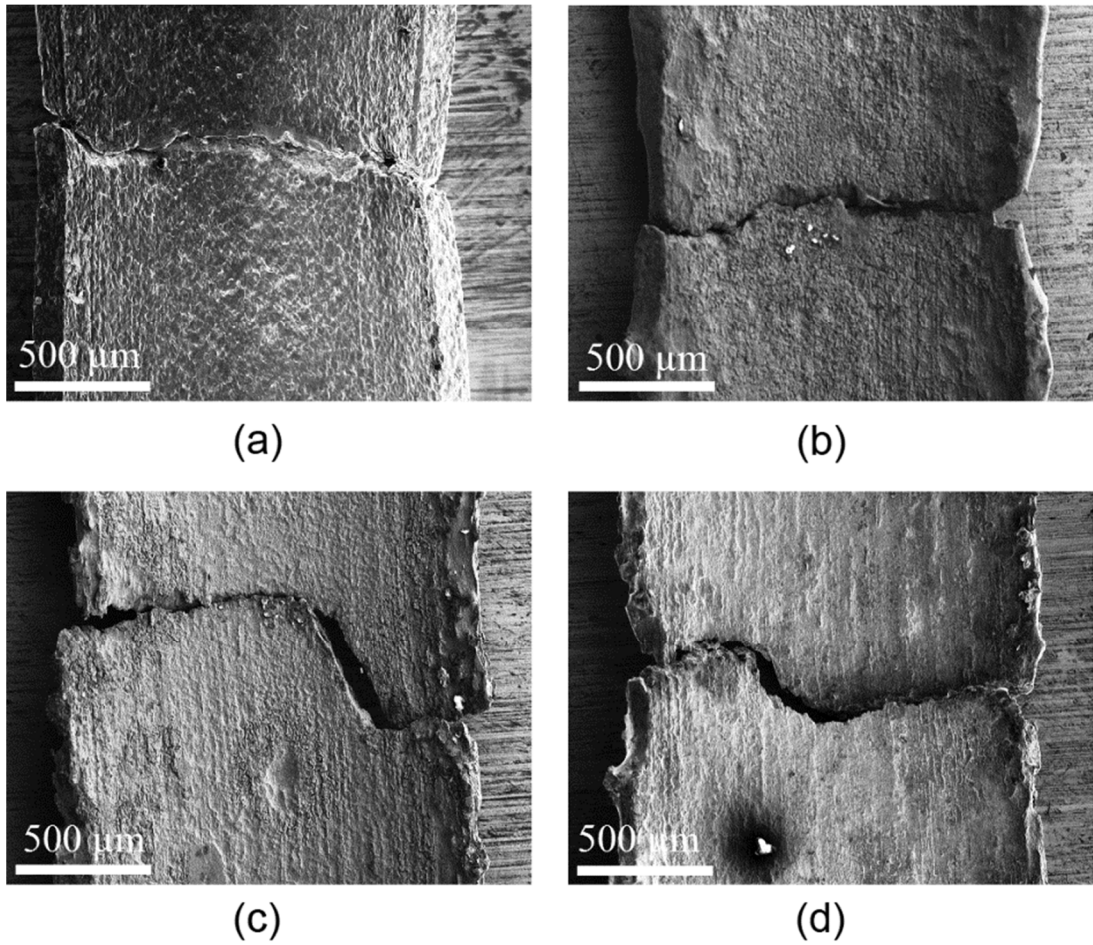
Figure 4.16 SEM images of typical fractured dogbone specimens after tensile testing: (a) 0% PS and 0 d (i.e. no corrosion), (b) 0% PS and 10 d (c) 2.7% PS and 10 d, (d) 8.4% PS and 10 d immersion

Typical fracture surfaces for specimens are shown in Figure 4.17. Non-corroded specimens with 0% plastic strain presented dimple (ductile) rupture, as shown in Figure 4.17(a). After 10 d immersion, specimens with 0% plastic strain displayed corrosion pits along with ductile features on the non-corroded cross-section, as shown in Figure 4.17(b). After 10 d immersion, specimens with plastic strain (2.7% and 8.4%) exhibited relatively greater pitting corrosion along with intergranular cracking and some transgranular cracking (arrows), as shown in Figure 4.17(c-d).

(a)   (b)

(c)   (d)
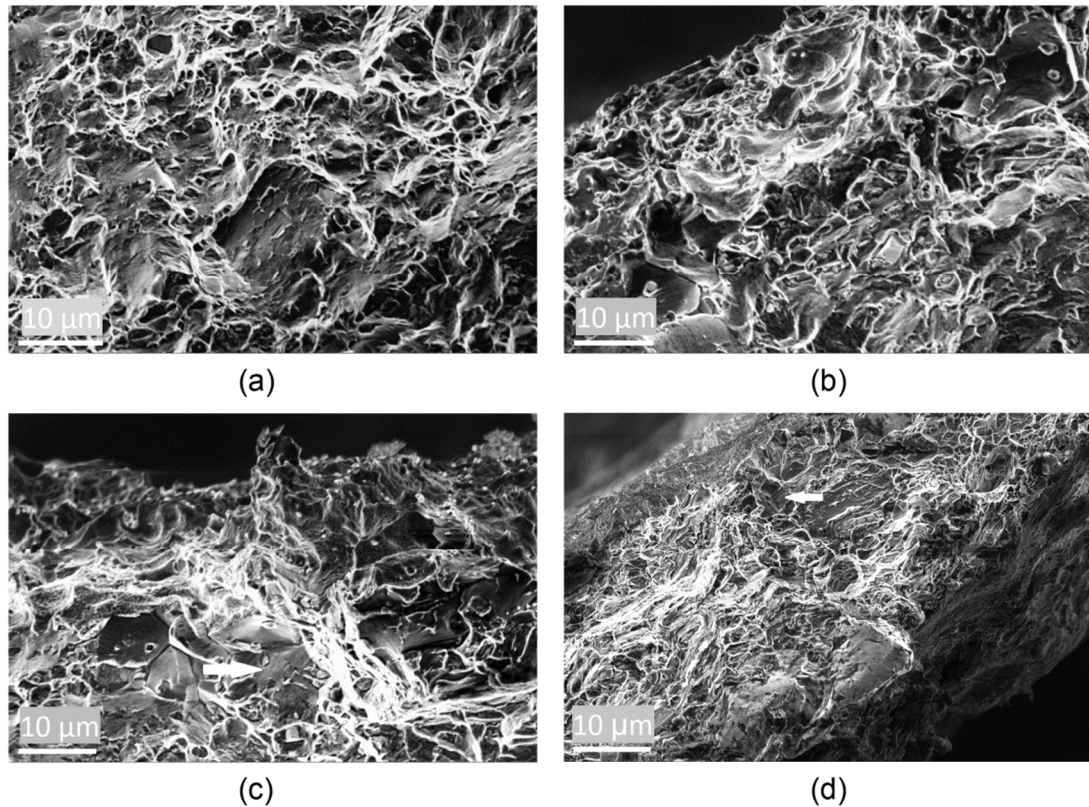
Figure 4.17 Typical morphology of the fracture surfaces of dogbone specimens after tensile testing (a) 0% PS and 0 d – dimple rupture, (b) 0% PS and 10 d – corrosion pits with ductile features on non-corroded cross section (c) 2.7% PS and 10 d – predominant intergranular cracking with brittle features and some transgranular (arrow) cracking, (d) 8.4% PS and 10 d corrosion - predominant intergranular cracking with brittle features and some transgranular (arrow) cracking

Based on the results of experiment B, the percentage mass lost over time by freely expanded WE43 stents, as shown in Figure 4.18(a), was relatively high for the first 10 h but decreased significantly between 10 h and 30 h. Beyond 30 h, the rate of mass loss was largely steady from which an average corrosion rate of 0.021 mg cm^{-2} h^{-1} was derived. The initial and steady state mass loss per unit area, observed for the stent was greater than that observed for dogbone specimens with 0% PS, as shown in Figure 4.18(b). Further, the shape of the curve for the stent was similar to that for dogbone specimens with plastic strain in experiment A; suggesting that the elevated rate of mass loss observed for the stent, may be attributed to the influence

of the plastic strain. The average strut width, in the longitudinal direction, decreased with immersion time for the stent, as shown in Figure 4.18(c), to a final value of 103 μm after 60 h.
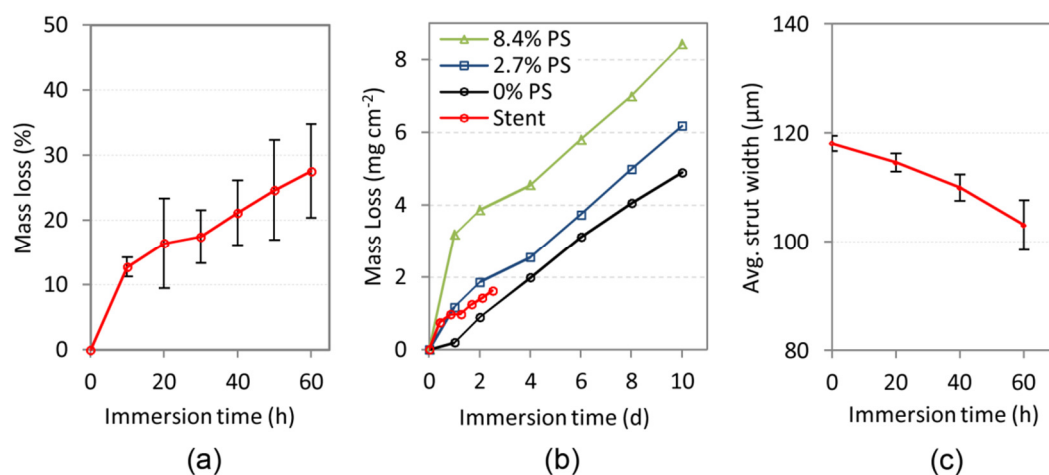
Figure 4.18 Results plots for experiment B (a) Percentage mass lost over time for stent, (b) Mass loss per unit area for stent and dogbone specimens (c) Plot of average strut width over time for stent. Error bars represent a single standard deviation from the mean

Images of the typical corrosion surfaces of the stent are shown in Figure 4.19(a-d). The liberation of H_2 gas bubbles into the solution, which indicated corrosion activity, was visualised using phase contrast microscopy for a number of stents and, was more pronounced at plastic hinge regions after 3 h immersion, as shown in Figure 4.19(a). After 20 h, the stent surfaces were rougher in appearance owing to preferential pitting corrosion of the magnesium matrix, as shown in Figure 4.19(b). A significant amount of material was corroded from the stent surface due to the localised micro-galvanic attack after 40 h, as shown in Figure 4.19(c). The morphology of stent struts after 60 h immersion is shown in Figure 4.19(d). It can be seen that increased localised corrosion attack occurred at regions of the stent that experienced high plastic strain during the deployment procedure, as indicated by the arrows. Representative force-compression curves, derived from radial stiffness tests

performed on stents, are shown in Figure 4.19(e). The radial stiffness was significantly lower for the WE43 stent compared to the 316L stent. The radial stiffness of the WE43 stent decreased significantly with immersion time, as shown in Figure 4.19(f), with a loss of 46 % in radial stiffness after 60 h immersion.
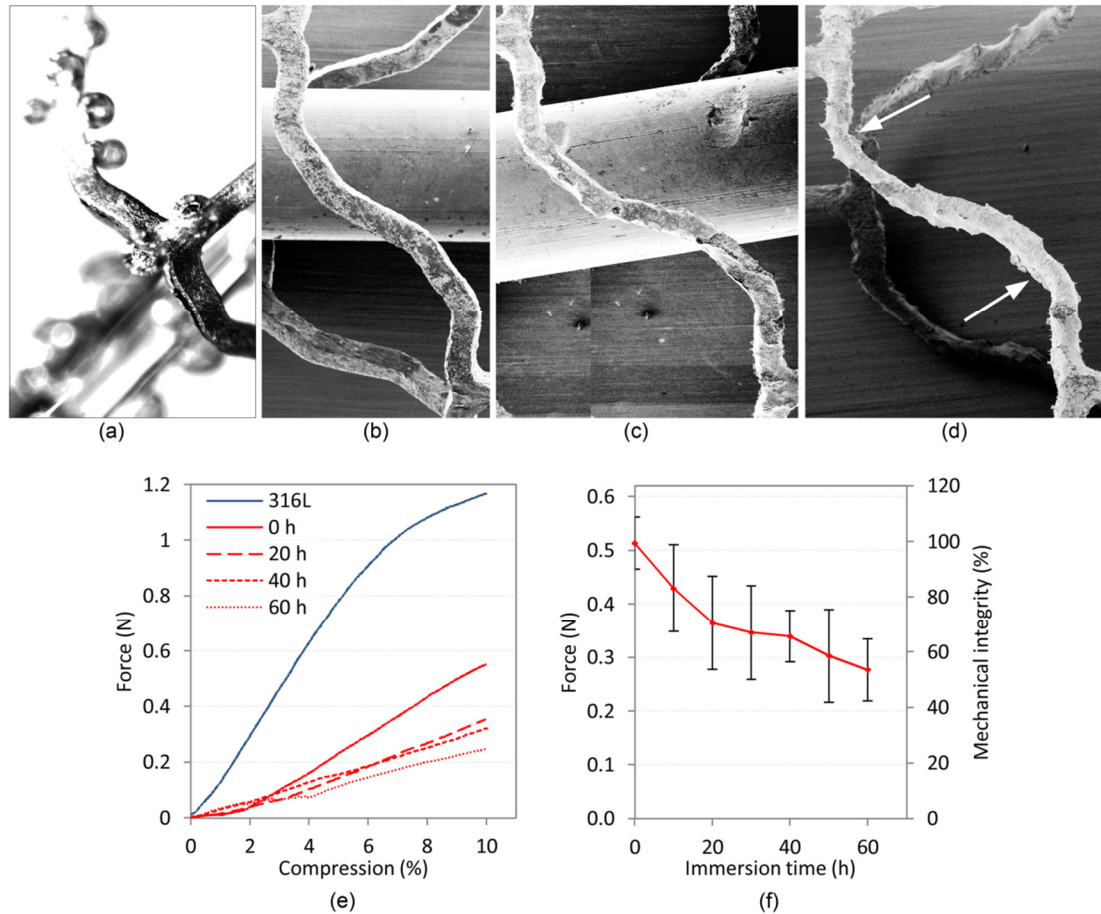
Figure 4.19 Typical morphology of a stent section after an immersion time of (a) 3 h, (b) 20 h, (c) 40 h & (d) 60 h. (e) Representative force versus compression curves for the WE43 and 316L stent (error bars omitted for clarity), (f) Temporal radial stiffness of WE43 stent. Error bars represent a single standard deviation from the mean

4.4 Corrosion Modelling

4.4.1 Corrosion Model Calibration

Three simulations were performed using the corrosion model in order to predict the corrosion behaviour of the dogbone test section for induced plastic strain values of

0%, 2.7% and 8.4%. A uniform plastic strain state was predicted in all simulations thereby confirming that suitable boundary conditions and loading were used for the model. Corrosion was simulated by the progression of the damage parameter, D, and the removal of elements from the FE mesh. The progression of D for the case of a dogbone model with 0% plastic strain is shown in Figure 4.20.
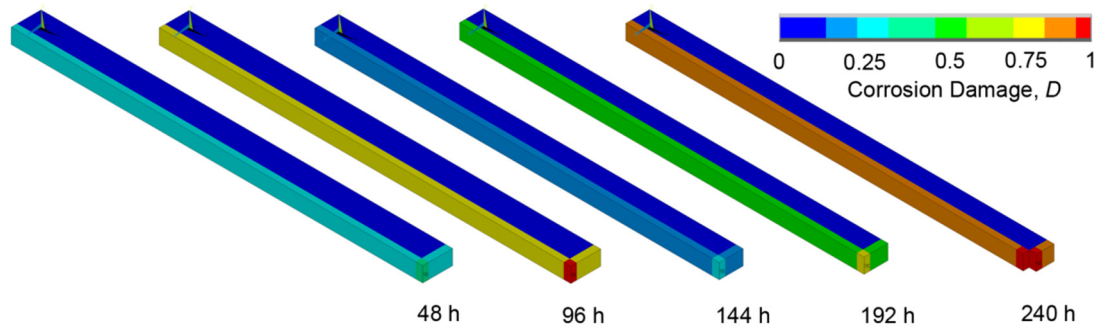
*Figure 4.20 Damage parameter (*D*) values predicted by the corrosion model at 48 h intervals for a specimen with 0% plastic strain*

The parameters for the corrosion model, which were calibrated based on the results of experiments A, are shown in Table 4.2. Parameters are shown for two cases, that of an idealised uniform corrosion model and that of the plastic strain model that most closely captured the experimentally observed corrosion behaviour. The calibrated rate of mass loss from the corrosion model was compared to that observed experimentally in Figure 4.21. It can be seen that the plastic strain model was capable of capturing the experimentally observed rate of mass loss over time for the three investigated values of plastic strain. However, the mass loss over time predicted by the uniform corrosion model showed only moderate correlation with that observed experimentally.

Parameter	δ_U (mm)	Δ_t (h)	L_e (mm)	k_u (h^{-1})	φ_e
Plastic Strain Model	0.015	1	0.012	0.00817	Variable
Uniform Model	0.015	1	0.012	0.00725	0

Table 4.2 Parameters used in the corrosion models in this work
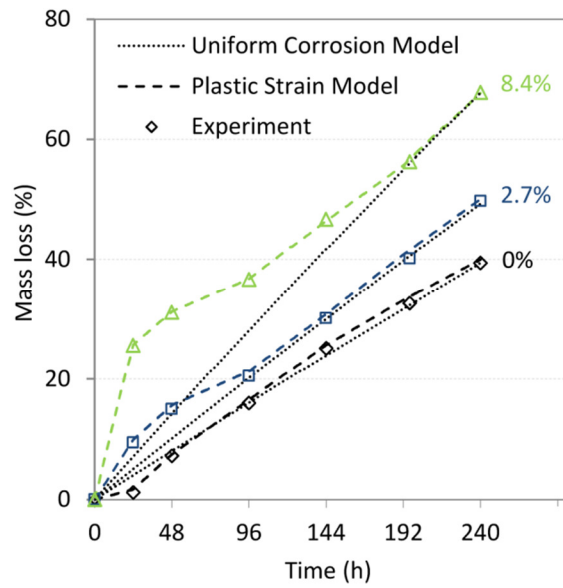
Figure 4.21 Predicted mass loss from the calibrated corrosion model compared to that observed experimentally

The plastic strain corrosion model was further able to capture the experimentally observed specimen stress-strain response and, the non-linear corrosion-induced reduction in specimen mechanical integrity, as shown in Figure 4.22, whereas the uniform model failed to predict the experimentally observed trend, as shown in Figure 4.23.
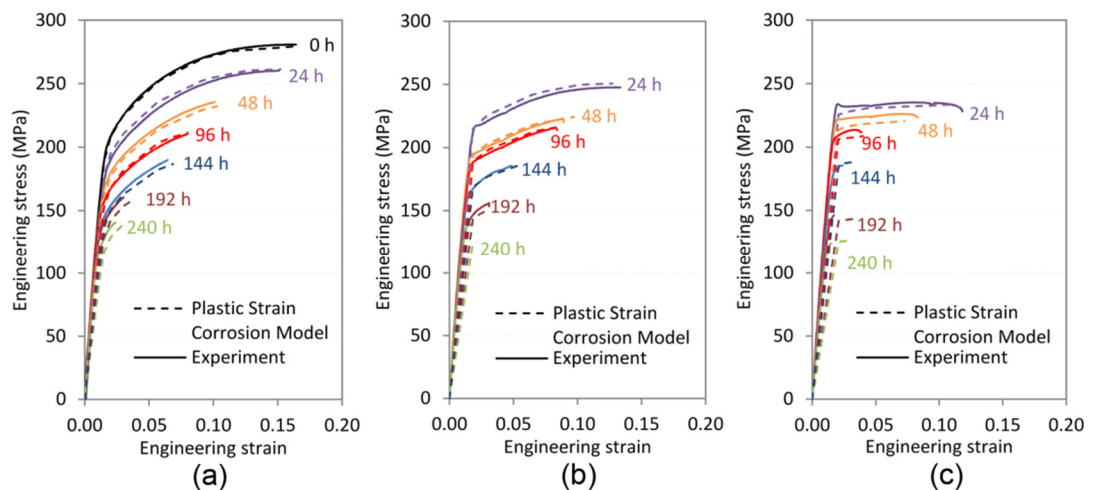
Figure 4.22 Predicted specimen stress-strain response over time for the plastic strain corrosion model compared to that observed experimentally for plastic strains of (a) 0%, (b) 2.7% and (c) 8.4%

91
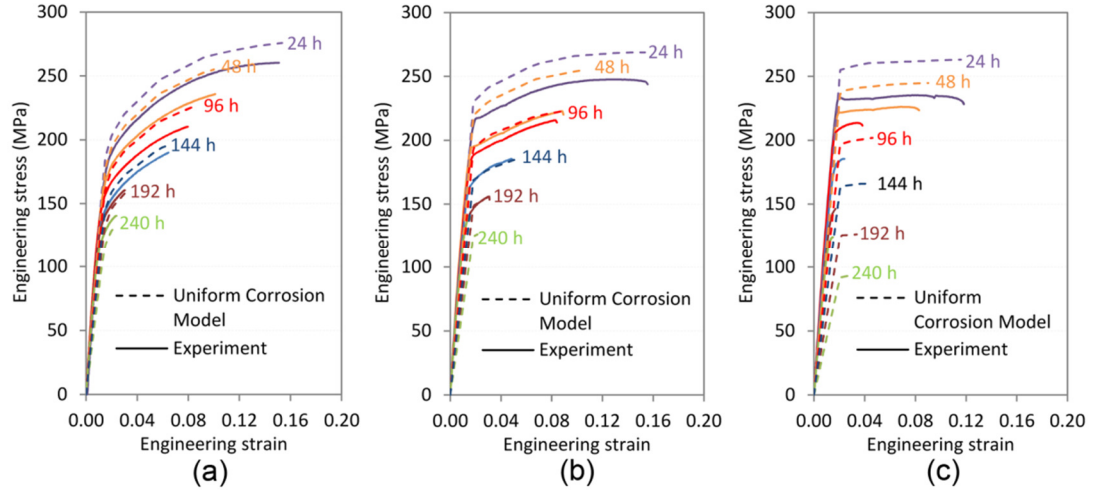
Figure 4.23 Predicted specimen stress-strain response over time for the uniform corrosion model compared to that observed experimentally for plastic strains of (a) 0%, (b) 2.7% and (c) 8.4%

4.4.2 Stent Model

The simulated free expansion and recoil of the RUC stent model is shown in Figure 4.24(a) and (b), respectively. It can be seen that the predicted magnitude of ε_{p1} varied from 0% to 27% for the deployed model. The stent outer diameters pre- and post-recoil were 4.3 mm and 3.9 mm, respectively. Following expansion and recoil, the corrosion of the stent was simulated using the plastic strain corrosion model, the linear plastic strain corrosion model and the uniform corrosion model, as shown in Figure 4.25(a-c), respectively. It can be seen that the predicted corrosion attack led to a non-uniform degradation in the stent geometry for all three corrosion models, with the largest amount of corrosion attack predicted at the plastic hinge regions of the stent. Compared to the other corrosion models, the plastic strain corrosion model predicted the greatest corrosion attack at the plastic hinge regions, as shown in Figure 4.25(a).
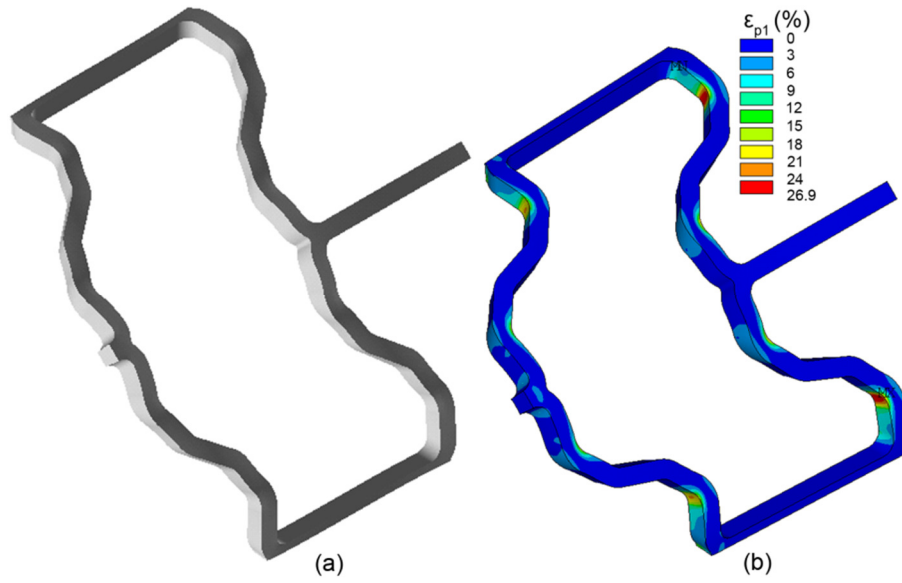
Figure 4.24 Simulated deployment of the RUC stent model: (a) fully expanded (b) predicted ε_{p1} post recoil
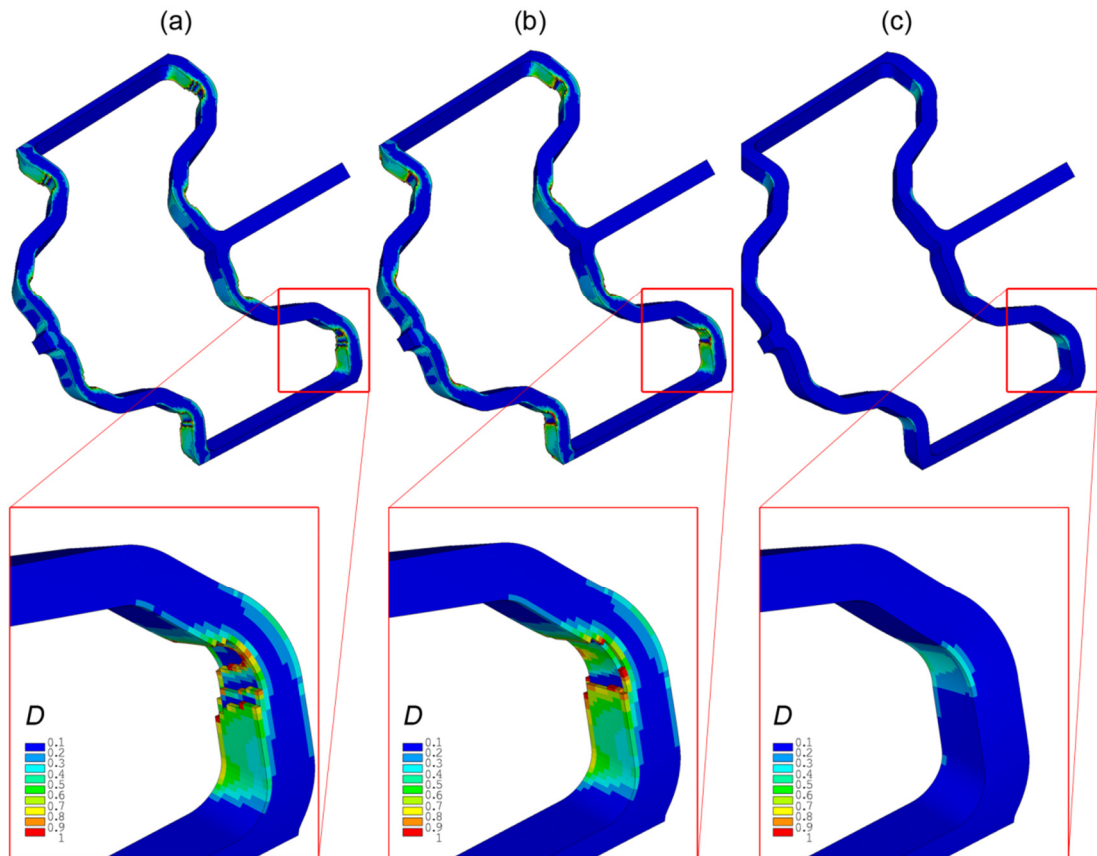
Figure 4.25 Predicted corrosion damage (D) after an immersion time of 10 hours (a) Plastic strain corrosion model (b) Linear PS corrosion model (c) Uniform corrosion model

The plastic strain corrosion model predicted the greatest stent mass loss over time and best characterised that observed experimentally, when compared to the other corrosion models, as shown in Figure 4.26.
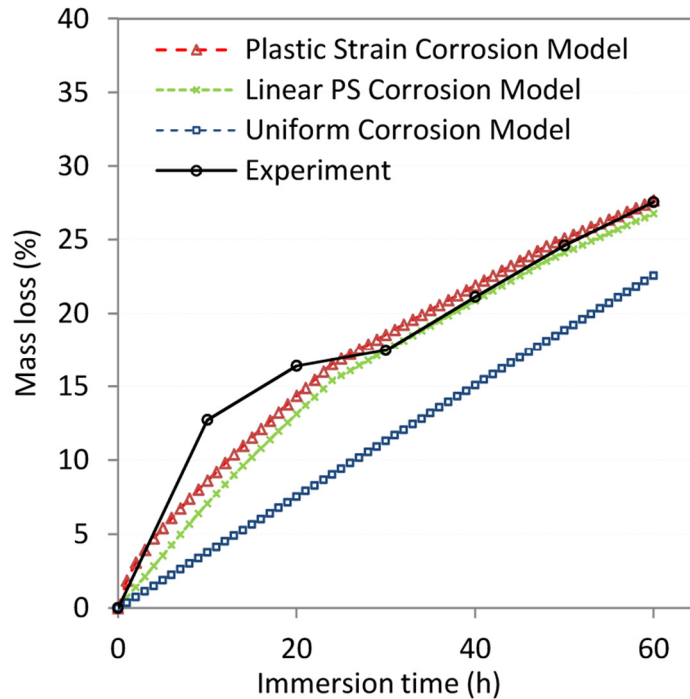
Figure 4.26 Predicted mass loss for the stent over time

The plastic strain corrosion model was further able to predict the influence of plastic strain on the stent radial stiffness both quantitatively and qualitatively, while the other two corrosion models failed to describe the non-linear relationship, as shown in Figure 4.27(a). The force compression curves predicted by the plastic strain corrosion model were in good agreement with those observed experimentally, as shown in Figure 4.27(b).

The plastic strain corrosion model was used to predict the influence of three different values of stent expansion ratio (SER) on the performance of the stent. It was found that higher values of SER led to significant increases in the predicted stent mass loss and in the temporal corrosion induced loss of radial stiffness for the stent, as shown in Figure 4.28(a) and (b), respectively.
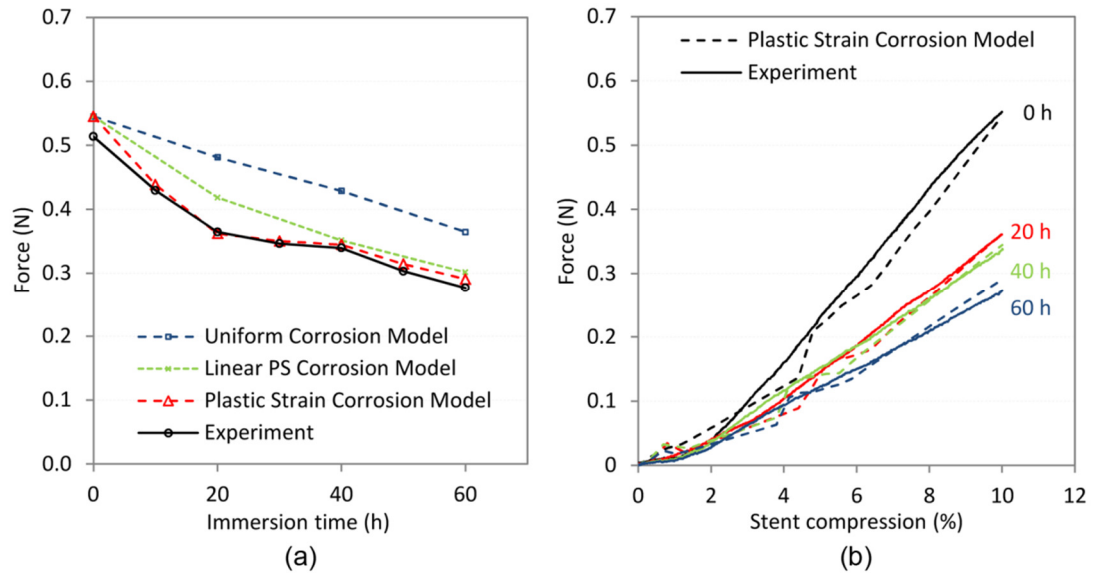
Figure 4.27 (a) Predicted stent radial stiffness at 10% compression (b) Predicted stent radial force versus percentage compression over time
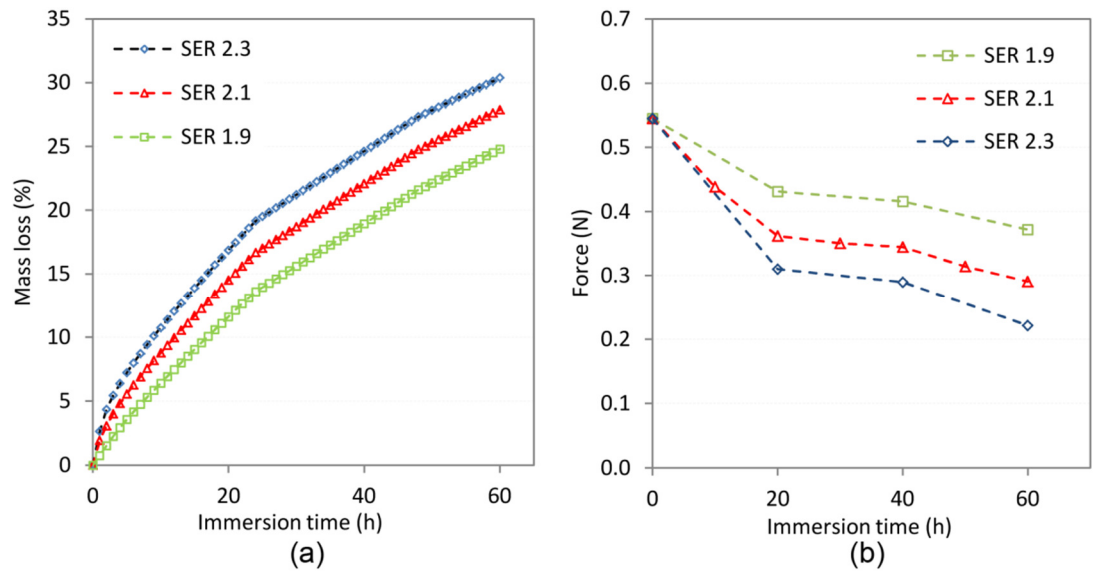
Figure 4.28 (a) Predicted stent mass loss for different values of stent expansion ratio (SER) (b) Predicted stent radial stiffness at 10% compression for different values of SER

95

5. Discussion

5.1   Stent Manufacture

Magnesium alloys possess many inherent characteristics that render them difficult to cut by laser (Abderrazak et al., 2009). The use of an inert nitrogen shield gas, appropriate laser cutting parameters and suitable surface treatments greatly reduced the effects of the HAZ produced by laser cutting. Machining parameters were optimised for the WE43 material in order to produce consistent strut geometries and clean cuts with minimal dross and spatter adherence. This enabled the normal fallout of waste sections from the machined stents.

Chemical etching provided a simple and inexpensive surface treatment which removed dross and spatter remaining from laser cutting, improved surface finish, imparted a non-toxic biocompatible phosphor-rich corrosion-resistant layer and provided a coating pre-treatment in order to functionalise the stent surface.

SEM, AFM and EDX studies showed that plasma etching and cleaning in a mixture of Ar-O_2 gas plasma and pure O_2 plasma successfully reduced surface roughness by 10% compared to chemically etched surfaces and completely removed surface contaminants remaining from the chemical etch process. Plasma processing yielded improvements in biocompatibility through increased surface sterility and wettability (Yi et al., 2004) and, also enhanced the surface adhesion properties for subsequently deposited coating (Nakamura et al., 1996).

The combination of chemical and plasma etching surface treatments produced stent surfaces with low roughness which have been associated with decreased thrombogenicity and IH formation (De Scheerder et al., 2001) and reductions in ISR in porcine models (Halwani et al., 2010). Also, the pitting tendency and corrosion rate are reduced with decreasing surface roughness for magnesium

alloys (Walter and Kannan, 2010) thus, permitting the mechanical integrity of the device to be maintained for a longer period of time.

The suitability of the processing route used in the manufacture of the magnesium stent was confirmed in deployment testing where all stents were expanded successfully and exhibited a uniform deployed geometry. During stent deployment, the elevated strain levels that are induced at plastic hinge sites may induce micro-cracks and other defects in poorly processed stents. Such defects can propagate through the material leading to strut fracture which may contribute to overall device failure and has been associated with higher rates of focal ISR (Celik et al., 2008; Sianos et al., 2004). In this study, stents were deployed with no cracking or fractures observed under SEM (Figure 4.11).

It should be acknowledged that cracks in the surface oxide layer are difficult to detect in post-deployment analysis (i.e. under SEM) as they are likely to close upon balloon deflation. Also, magnesium has high affinity to oxygen and therefore a new surface oxide is likely to quickly form over cracks and other defects making their detection difficult. Sub-surface defects would likely become evident with the progression of corrosion in the substrate, though no evidence of this was observed in the experiments. Non-destructive test (NDT) methods such as ultrasonic testing, eddy current or phased array could be used to determine the severity of the material damage induced in the struts by the stent deployment process.

5.2 Mechanical Testing

The ability of the WE43 stent to deploy at low balloon pressures, compared to commercial 316L stents (Figure 4.10(a)) could potentially be beneficial in terms of reducing arterial injury and hence ISR in arteries with low to moderate levels of disease where predilation of stenosis is not required. Although it has been shown that IH is not significantly greater after high pressure implantation of traditional BMS

compared to low pressure implantation (Hoffmann et al., 2001); no such investigation has been carried out for bare-metal or drug-eluting magnesium stent platforms. Lower radial stiffness and higher elastic recoil were observed for the WE43 stent, compared to the 316L stent, in the deployment experiments (Figure 4.10(b)). Elastic recoil of a stent permits an immediate re-narrowing of the stented artery upon balloon deflation and represents a negative clinical result. The relatively high elastic recoil observed in this work for the WE43 stent in the MCA may be attributed to the influences of the stent geometry, the relatively low elastic modulus of WE43 and the moderate SER used in the experiments. These findings are in agreement with those reported in clinical trials of the Biotronik Magic stent (AMS-1), where post-dilation was frequently used to obtain larger lumen diameter, owing to the relatively low radial stiffness and high acute recoil of the stent (Erbel et al., 2007). Later versions of the Biotronik DREAMS stent used a non-commercial form of the WE43 alloy and had a revised stent geometry that reduced elastic recoil below 3% (Waksman, 2011).

Post-dilation and over-expansion presents a greater fracture risk for magnesium stents compared to stents manufactured from traditional materials, such as 316L, due to the increased likelihood of localised material fracture in magnesium alloys (Grogan et al., 2012; Poncin and Proft, 2003). In this study, trial deployment tests were carried out to investigate the risk of fracture for the magnesium stent. Stents were deployed using both 3.5 mm and 4.0 mm angioplasty balloons, representing SERs of 2.05 and 2.3, respectively. SEM analysis revealed a number of fractured struts for a SER of 2.3. In all cases, the stent successfully expanded to a SER of 2.05 (Figure 4.11(a)), with no fractures observed, which compared favourably to the SER (1.5) observed for crimped AZ31 stents in a similar study, where some strut fractures were reported (Wu et al., 2012). Therefore, all the subsequent deployment testing carried out in this study used 3.5 mm angioplasty

balloons, as described in section 3.3.

In the third test (cyclic strain amplitude), prior to the application of the static pressure loads, the elastomeric MCA acted to reduce the diameter of the stent that was deployed within it. Under the influence of physiological pressure loads, the diameter of both the MCA and the stent were observed to increase. It was noted that contact was maintained at all times during the tests between the outer stent surface and the inner MCA surface. In mechanics therefore, the stented MCA construct could be represented by two springs of different stiffness connected in series. The stent was significantly stiffer and likely followed a near-linear pressure-displacement curve under physiological pressure loads. The MCA was significantly more compliant and exhibited a non-linear hyperelastic response under pressure loads in the physiological range (Colombo et al., 2010). Significantly higher cyclic strain amplitude levels were observed for MCAs stented with the WE43 stent, compared to the 316L stent (Figure 4.10(d)). This may be attributed to the influence of the lower elastic modulus of WE43 compared to 316L and the significant differences that existed in the geometrical design of the two stents. The WE43 stent had a greater inner surface area, compared to the 316L stent, upon which static pressure acted to deform the stent radially. This may have contributed to the higher cyclic strain amplitude levels observed for the WE43 stent. Another limitation of the test was the inability of the videoextensometer to measure the ID or OD of the stent directly by visualisation due to the opacity of the MCA material. Therefore changes in the diameter of the stent (and hence cyclic strain amplitude) were inferred from measurements of the MCA OD which was not ideal. Small measurement errors in the apparent stent OD were likely introduced due to thickness changes in the walls of the MCA while under the influence of the two different pressure loads.

Compliant magnesium stent designs that facilitate high cyclic strain amplitude levels that are closer to the normal physiological range (5-8%) (Draney et

al., 2002), and thus maintain the anti-proliferative effect of cyclic strain amplitude on SMCs (Colombo et al. 2012), could offer an effective strategy to reduce ISR rates. The subsequent corrosion-induced loss of mechanical integrity of magnesium stents (Figure 4.19(f)) should produce a further temporal increase in the cyclic strain amplitude. Upon completion of stent absorption, reconstitution of normal vessel vasomotor function can be expected; thus removing many of the known stimuli for IH and ST (Jabara et al., 2009). It has been suggested that current BAS may not be ideal for patients with severe amounts of lesion calcification due to their limited deliverability scaffolding properties (Kern, 2012). Conceptually, an ideal candidate group for magnesium stents and other types of BAS may be young patients with small plaque burden and focal disease or those requiring treatment of vulnerable plaques prior to plaque rupture (Sabate, 2014).

5.3   Corrosion Experiments

The micro-galvanic corrosion attack observed in this work (Figure 4.13(c)) and, the tendency toward a uniform localised corrosion that progressed in a layer by layer manner (Figure 4.13(f)), is in agreement with results reported for larger samples of WE43 in similar SBF compositions in the literature (Kalb et al., 2012). However, the steady-state corrosion rates (0.021-0.027 mg cm^{-2} h^{-1}) observed in this work (Figure 4.18(b)) were between eight and twenty orders of magnitude lower than those reported for larger WE43 specimens (Rettig and Virtanen, 2009; Zhang et al., 2012) and may be partly attributed to the increased resistance to galvanic corrosion afforded by materials processing of the precursor tubes (Ge et al., 2013; Wang et al., 2007). Further, the surface treatments imparted a magnesium phosphate surface layer with reduced impurity levels (Nwaogu et al., 2009) and low surface roughness (Gray-Munro et al., 2009; Walter et al., 2013) which significantly improved corrosion resistance. This layer may have contributed to the low corrosion rate observed for specimens with 0% plastic strain (Figure 4.12) though some

degradation of the layer was observed after 1 d immersion (Figure 4.13(a)). The layer was significantly more degraded on specimens with plastic strain after 1 d (Figure 4.14(a)).

Mass loss measurements, which are applicable to materials exhibiting near-uniform corrosion, revealed two different trends among the specimens (Figure 4.12). Specimens with 0% plastic strain exhibited a low initial corrosion rate and a largely linear rate thereafter; while higher levels of plastic resulted in larger increases in mass loss in the first 2 d of immersion and moderate increases in steady-state corrosion rate thereafter. The increased mass loss due to plastic strain may be attributed to the likely damage caused to the brittle surface oxide and a deformation-induced acceleration in micro-galvanic attack combined with hydrogen embrittlement and stress corrosion cracking (SCC). Damage and dissolution of the surface oxide and severe pitting attack accompanied by cracking of the corrosion layer (Figure 4.14(a-b)) led to greater levels of material removal from the surface (Figure 4.14(c)) and increased corrosion on laser cut edges (Figure 4.14(e)). These findings are in agreement with those from previous mechanical-electrochemical studies which showed that plastic strain (5.5%) induced significant increases in both the pitting susceptibility of grains (one order of magnitude) and the cathodic reactions at grain boundaries (two order of magnitude) of an aluminium alloy in NaCl solution (Krawiec et al., 2012). Similar findings have been reported for magnesium alloys that were subjected to compression loading (Snir et al., 2012).

The corrosion-induced reduction in the thickness of stent struts (Figure 4.18(c)) was greatest in plastic hinge regions (Figure 4.18(d)) and contributed to a 46% reduction in radial stiffness after 60 h (Figure 4.19(f)) despite a total mass loss of only 28% for the stent. The layer of corrosion products that are formed on the specimen surfaces appeared to offer little protection to the substrate and thus corrosion rates remained largely linear (Figure 4.18(b)). The composition of the

corrosion products, as determined by EDX analysis, was rich in Ca, O, P, Mg, Cl and C, and was similar to that reported for WE43 specimens in similar solutions (Kalb et al., 2012; Rettig and Virtanen, 2009). The shape of the mass loss curve and the loss of approximately 25-30% stent mass after 60 h, due to uniform micro-galvanic and SCC corrosion processes, is in agreement with results reported for an electropolished AZ31 stent (Wu et al., 2012).

The corrosion-induced reduction in the stress-strain response and mechanical properties (UTS, ε_u, E and σ_y) observed in experiment A (Figure 4.15), likely resulted from the reduction in dogbone specimen cross-section and the influence of stress concentrations in pitted regions and, was similar to the reduced stress-strain responses reported for loaded and non-loaded magnesium specimens (Bowen et al., 2012; Winzer et al., 2008). Compared to specimens with 0% plastic strain, specimens with plastic strain exhibited a further reduction in mechanical properties, most notably for ε_u, E and σ_y. It was concluded that the presence of plastic strain increased the micro-galvanic corrosion activity and induced intergranular and transgranular SCC (Figure 4.17). Similar SCC failure modes have been reported for RE magnesium alloys after slow strain rate tests in NaCl solution (Kannan et al., 2008). Magnesium alloys are susceptible to a number of stress-mediated SCC processes which may lead to the rupture of the surface film, H_2 gas ingress and embrittlement and crack initiation and crack growth leading to fracture (Winzer et al., 2005a).

The corrosion-induced reduction in mechanical strength observed for specimens with 0% plastic strain (Figure 4.15(d)) was less rapid than that reported previously for AZ31 and Mg–6Zn alloy specimens in similar studies (Grogan et al., 2011; Zhang et al., 2010) and, may be attributed to the relatively uniform reduction in specimen cross-section seen in this work. Consequently, a mass loss of 40% for dogbone specimens and 28% for stents, corresponded to a 50% reduction in

specimen mechanical strength, compared to a mass loss of only 10-20% in similar studies (Grogan et al., 2011; Zhang et al., 2010). By comparison, the pitting attack observed in this work (Figure 4.13(c)) was less localised, owing in part to the relatively low pitting factor (defined as the ratio of the deepest penetration to the average penetration) of WE43 compared to other magnesium alloys (Kalb et al., 2012).

While no significant differences were observed in the corrosion behaviour on the inner and outer walls of specimens, the corrosion attack observed on laser cut edges had a different morphology (Figure 4.13(g)) and progressed at a higher rate when compared to the other surfaces, particularly in specimens with plastic strain (Figure 4.14(d-e)). Since laser cutting may influence surface roughness, alloy microstructure and expose higher index crystal planes of lower corrosion resistance (Liu et al., 2008), in the absence of subsequent surface modification or coating, higher corrosion rates can be expected on laser-cut edges; though a detailed study has not been carried out for magnesium stents in this regard.

The results of experiment A and B suggest that corrosion behaviour was strongly influenced by alloy microstructure and the magnitude of deployment strains in this study. The findings demonstrate the potential for improvements in the mechanical and corrosion behaviour of magnesium stents through improvements in material processing and surface treatments and, optimisation of stent designs in order to minimise deployment strains. Based on these findings, it is likely that uniform deployed configurations and high strut apposition rates are critical to ensure uniform and controlled corrosion of magnesium stent struts *in vivo*, with an accompanying controlled reduction in corrosion-induced mechanical integrity, owing to the influence of complex blood-tissue interactions on the corrosion behaviour of magnesium alloys (Pierson et al., 2011; Wittchow et al., 2013).

The macroscopic tensile stress-strain response of non-corroded dogbone specimens (Figure 4.15) was shown to be different to that reported for bulk specimens of WE43 (Gu et al., 2010). Compared to bulk specimens with larger grain sizes, dogbone specimens exhibited decreases in σ_y, modest decreases in UTS but no significant differences in ε_u and ε_f. These findings are largely in agreement with those from experimental (Guo et al., 2011) and numerical (Grogan et al., 2014b) studies that examined the influence of grain size on the mechanical properties of non-corroded magnesium materials. The differences in the mechanical properties of dogbone and bulk specimens may be attributed to influences such as, the fine-grained microstructure of the precursor tube (Ge et al., 2013) and size effects resulting from the small specimen geometry and its processing. Magnesium specimens with small grain size have a larger grain boundary fraction and consequently release local strain energy faster, thereby exhibiting lower E values (Moitra, 2013).

Studies of the corrosion behaviour of pure magnesium wires in static SBF and rat artery models suggest that *in vitro* corrosion rates (as denoted by a combined metric) are approximately three times greater than those observed *in vivo* (Bowen et al., 2013). The lower *in vivo* corrosion rates observed for magnesium alloys have been attributed to influences such as the adsorption of proteins on the implant surface, the availability of oxygen (Feyerabend et al., 2012), the levels of blood flow in nearby tissues (Willbold et al., 2013), the suppression of microgalvanic corrosion due to encapsulation (Zainal Abidin et al., 2013) and the influence of macrophages which can release acid digesting substances (Wittchow et al., 2013). The *in vitro* corrosion rate observed in this study for the WE43 stent was lower than those previously reported for WE43 specimen in similar SBF solutions. However, the likely *in vivo* lifetime of the stent would be far too short to scaffold a coronary artery for the six-to-nine month period required, as was the clinical experience with the

(WE43) bare-metal Biotronik AMS-1 (Erbel et al., 2007). Future improvements in magnesium metallurgy and materials processing, combined with more effective surface treatments and stent coating strategies should permit better control of degradation rates and allow the lifetime of magnesium stents to be prolonged. Given the high susceptibility of magnesium alloys to galvanic corrosion, accelerated *in vitro* corrosion testing via electrochemical testing techniques, such as open circuit potential and cyclic potentiodynamic polarisation testing (Gerber, 2008; Nascimento and Zeddies, 2007), should provide useful methods for rapid evaluation of the corrosion behaviour of different magnesium alloys for biomedical applications.

Biodegradable polymers such as poly (l-lactic acid) (PLLA), poly (L-caprolactone) (PCL) and poly (glycolic acid) (PGA) have been approved for numerous clinical applications (O'Brien and Carroll, 2009). More recently, the use of these polymers as protective coatings intended to increase the corrosion resistance of biodegradable magnesium has been explored. PCL and PLLA display good adhesion and cytocompatibility properties, and offer significant reductions in the corrosion rate of the magnesium substrate (Xu and Yamamoto, 2012). In a rat model, poly(1,3-trimethylene carbonate) (PTMC) coatings reduced the corrosion rate by three orders and one order of magnitude compared to bare and PCL coated Mg-Zn-Mn alloy specimens, respectively (Wang et al., 2013). A PLGA coating was used on the Biotronik AMS-3 stent. In animal trials, a mixture of 85% lactide and 15% glycolide provided the lowest intimal area at 28 days and 180 days, and the highest endothelialisation score at 28 days (Wittchow et al., 2013). Chen et al. (Chen et al., 2011) noted a special interaction between high purity magnesium and both PCL and PLA coatings under dynamic SBF flow conditions, which had a deleterious effect on corrosion performance. Such interactions between polymer coating and the magnesium substrate could pose challenges to the future development of drug-eluting magnesium stents.

5.4   Corrosion Modelling

The peak strain (~27%) predicted by the FE model for the deployed stent was significantly greater than the experimentally observed value of failure strain for WE43 (~20%). Strain in the FE model was predicted in the circumferential direction (first principal strain) which was the direction most relevant to the stent deployment analysis. It should be noted that the strain state in the deployed stent was more complex than that induced experimentally by simple uniaxial tensile loading of the dogbone specimens. Therefore, it is suggested that the use of a ductile failure criterion, such as Oyane's Criterion, within the FE model would facilitate better prediction of material failure in future stent deployment analyses.

Observations from the corrosion experiments showed that uniform micro-galvanic corrosion and SCC were likely to be the dominant corrosion processes for both dogbone and stent specimens. The results also suggested a plastic strain mediated corrosion attack for both specimens, as has been observed in previous studies of magnesium alloys (Snir et al., 2012; Wittke et al., 2014). Therefore, an element-specific plastic strain parameter (φ_e) was introduced in this work in order to account for the effects of plastic strain induced corrosion in the modelling framework. The plastic strain corrosion model, which was calibrated based on the results of the corrosion experiments, was capable of predicting the experimentally observed mass loss and the corrosion-induced reduction in stress-strain response of the dogbone and stent specimens, whereas the uniform corrosion model failed to capture the observed effects. The use of a non-linear relationship between ε_{p1} and φ_e for elements with ε_{p1} values above of 8.4%, rather than a simple linear relationship, in the corrosion model better captured the strain-mediated corrosion attack at plastic hinge regions (Figure 4.25). Although only the proportion of elements in the model having ε_{p1} values was modest (4%), the increased corrosion rates prescribed for these elements in the plastic strain model led to significantly greater reductions in

the predicted radial stiffness for the stent, without significantly increasing the overall mass loss of the stent, when compared to the linear corrosion model. This approach (i.e. the use of a non-linear relationship between ε_{p1} and φ_e) was in contrast to previous studies where a ductile failure condition was employed by setting $D = 1$ for elements in which strains exceeded those observed experimentally at the UTS (Gastaldi et al., 2011; Grogan et al., 2011). Thus, in these models, elements may be immediately removed from the mesh at the start of the corrosion simulation leading to the prediction of instantaneous mass loss at a simulation time of zero.

The plastic strain parameter (φ_e) used in this work accounted for both the effects of corrosion and plastic strain (strain hardening) in a single parameter. It may be possible to develop other parameters for use in the corrosion model which delineate the individual influences of plastic strain and corrosion on specimen mechanical integrity and mass loss. Figure 5.1(a) shows the typical stress-strain response for a specimen induced with 2.7% plastic strain (curve 1) and, the subsequent response for the same specimen prior to corrosion (curve 2) and after corrosion (curve 3). The difference between the response observed at curve 1 and 2 indicated the loss of mechanical integrity (reduced ductility) due to plastic strain while that observed at curve 2 and 3 indicated the loss of mechanical integrity due to corrosion alone. As shown in Figure 5.1(b), the mass loss due to plastic strain (green curve) could be delineated by subtracting the mass loss curves for 0% and 2.7% plastic strain.

This use of the element exposure parameter (κ_e) which scaled the corrosion rate of the element according to the number of exposed element faces, allowed the model to predict the rounding of initially sharp strut corners which is expected for a diffusion-controlled corrosion process (Figure 4.25). This feature could also be modified to include the effects of other corrosion phenomena that may be influenced by the number of exposed element faces, such as the growth of corrosion pits.

Although the effects of pitting corrosion were not included in his work, the results of the experiments suggested that the pitting tendency of the WE43 was low when compared to that in previous studies where it was the primary corrosion process (Grogan et al., 2011). The model developed in this work is deterministic in nature. Probabilistic models are useful as they can be used to handle variability and uncertainty which are inherent in many corrosion processes (MacDonald, 1994).
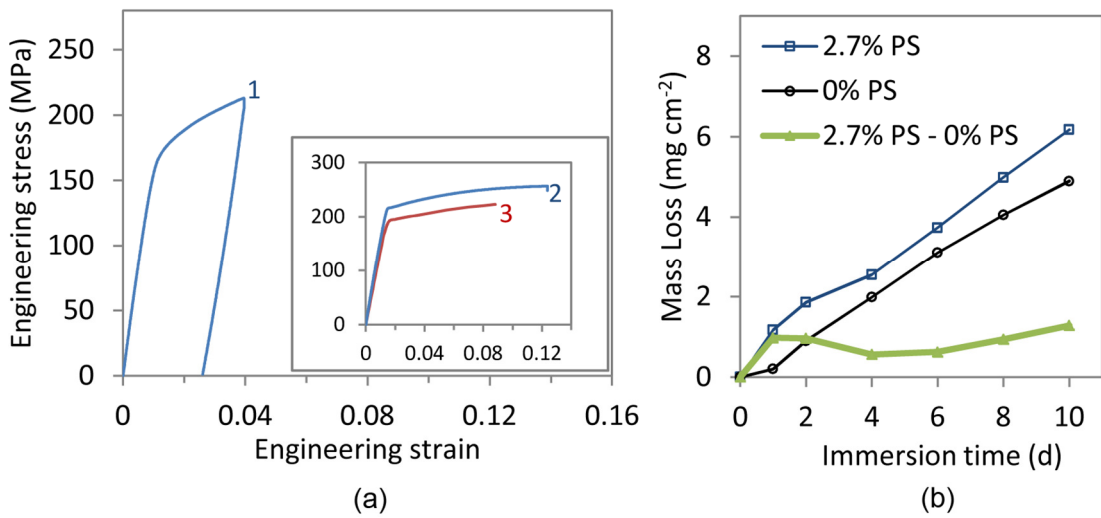
Figure 5.1 (a) Typical stress-strain response for a specimen induced with 2.7% plastic strain (curve 1) and, the subsequent response (inset) for the same specimen prior to corrosion (curve 2) and after corrosion (curve 3), (b) Mass loss curve (green) that is driven by plastic strain alone

Simulation of stent performance may result in large and computationally-expensive FE models owing to strong material and geometrical nonlinearities and, complex multiple contact phenomena. The RUC corrosion model developed in this work had good computational efficiency, requiring approximately nine CPU hours on a single quad-core Intel i7 (2.6 GHz) on a desktop computer. The RUC stent model offered significant reductions in model size and solution time which is especially useful in the preliminary stages of stent design where many cycles of iteration between the simulation and parameter selection are necessary (Xia et al., 2007).

5.5   Summary and Limitations

A number of limitations of this study should be highlighted. No post-cut annealing was used to relieve residual stresses (Poncin and Proft, 2003) in the specimens following laser cutting. However, the precursor tubes were pre-annealed prior to laser cutting. The heat generated during laser cutting was minimised by using a pulsed laser source, high pressure shield gas, and cutting paths and laser parameters intended to minimise heat effects in the machined parts.

Although the surface treatments employed in this work are likely to differ from those used for the Biotronik AMS-1 (Erbel et al., 2007), they provided effective and inexpensive methods for functionalising the laser cut stents. The suitability of the processing route used was demonstrated in bench tests where all stents were expanded successfully to a SER of 2.1 and exhibited a uniform deployed geometry with no evidence of strut fracture.

While the thickness of the dogbone specimen was equal to that of the stent strut (140 µm), its width (1.85 mm) was approximately 1.5 orders of magnitude greater. Therefore, the mechanical and corrosion behaviour observed for the dogbone specimens was indicative of behaviour at that size-scale. However, when compared to the existing studies for magnesium stents in the literature, the specimen size, materials processing and surface treatments used in this work represent a significant step towards elucidating the precise behaviour of magnesium stent struts. Furthermore, the use of finished WE43 stents in the experiments of this work to elucidate device performance characteristics represents a significant contribution to knowledge.

The experimental performance of the stents was determined in MCAs that mimicked only the passive mechanical properties of healthy coronary arteries under static pressure conditions, though the results provided useful data regarding the

comparative performance of WE43 and 316L stents. The *in vitro* conditions used in the corrosion experiments yielded useful fundamental information regarding the corrosion behaviour of the stent and the alloy material but they cannot fully account for the complex tissue interactions that may influence the performance of magnesium devices *in vivo* (Pierson et al., 2011). However, it is noted that the corrosion experiments in this work were carried out under sterile conditions in a cell culture incubator; only a few such studies have been reported for magnesium (Kirkland et al., 2010).

The influence of stent crimping, compressive loading and dynamic (fatigue) loading on corrosion behaviour was not examined in this work. The corrosion model was calibrated in experiments that examined corrosion behaviour at three plastic strain values (0%, 2.7%, 8.4%) and at intervals of twenty four hours. The first principal plastic strain (ε_{p1}) which acted parallel to the applied uniaxial tensile loading in the dogbone specimen, was employed as the mediator of the corrosion in the corrosion models. It is noted that the plastic strain state in the stent was non-uniaxial owing to the complex loading pattern that is associated with the stent deployment process though the model was still capable of capturing the experimentally observed behaviour. Linear rather than continuous functions were used in the representation of the mass loss curves and in the diffusion-controlled corrosion of elements in the corrosion model.

6. Conclusions

6.1 Main Findings

The main aim of this study was the determination of the mechanical and corrosion performance of an absorbable magnesium stent using experimental and numerical analysis. A processing route was identified by which viable balloon-expandable coronary stents were manufactured from precursor tubes of the WE43 alloy using a combination of laser cutting and chemical and plasma-based surface treatments. The physical and chemical characteristics of the stent surfaces produced were revealed through SEM, AFM and EDX analyses. To the author's knowledge, this is the first study to fully describe the fabrication of WE43 stents and to describe the surface treatment of magnesium stents by plasma processing (RIE).

While limited data regarding the performance of the Biotronik AMS-1 stent (also WE43) has been reported in clinical trials (Erbel et al., 2007), this is the first experimental study to report on the mechanical and corrosion performance of a WE43 stent. It is also the first study to demonstrate the critical role of deployment-induced plastic strain on the subsequent corrosion behaviour and temporal scaffolding ability of a magnesium stent. By way of novel corrosion experiments, plastic strain was shown to significantly increase corrosion rates, particularly at plastic hinge regions, thus leading to a deformation-induced acceleration of the underlying corrosion processes. The likely primary corrosion process was identified as uniform micro-galvanic corrosion in non-deformed specimens and as uniform micro-galvanic corrosion combined with SCC and hydrogen embrittlement for specimens with plastic strain. Damage to the brittle surface oxide caused by plastic strain was also thought to play a significant role in accelerating the corrosion attack. Relatively modest mass losses at hinge regions were shown to induce significant reductions in the temporal radial stiffness of the stent.

The corrosion rates observed in this work were found to be significantly lower, with a reduced tendency toward corrosion processes such as pitting corrosion, when compared to many of the existing corrosion studies of magnesium alloys. The rate of mass loss and the nature of the underlying corrosion processes observed for the stent was comparable with those of an electropolished AZ31 stent in a previous study (Wu et al., 2012). When compared to the mechanical properties reported for bulk WE43 specimens in the literature, the non-corroded dogbone specimens used in this work exhibited significantly lower mechanical properties, particularly with respect to E, σ_y and UTS. The observed effects were strongly linked to the material microstructure and the surface properties of the specimens and thus these findings highlight the vital importance of conducting testing on the stent itself or a sample of the stent in its final form and finish. The experimental data presented in this work, regarding the mechanical and corrosion performance of WE43 stents and specimens, will serve as input in future computational models of stent deployment, corrosion analysis and stent optimisation studies.

In the deployment experiments, the WE43 stent deployed at a significantly lower range of balloon pressures than the commercially-available 316L stent. This could potentially be beneficial in terms of reducing arterial injury and hence ISR in arteries with low to moderate levels of disease where predilation of stenosis may be avoided. However, this requires further investigation. The WE43 stent was found to have a lower initial radial stiffness that was observed to decrease with immersion time in the corrosion experiments. Non-corroded WE43 stents were shown to support higher levels of cyclic strain amplitude which plays a crucial role in reducing ISR, owing to the anti-proliferative influence of higher cyclic strain amplitude on SMCs (Colombo et al., 2009). These findings highlight the need for improved understanding of the biomechanical environment in stented vessels. In the future, modulation of the cyclic strain amplitude in vessels stented with compliant

magnesium stent designs that have steerable corrosion kinetics should provide a method to improve the ISR outcomes observed with current stents.

The need for corrosion models that explore the interaction of plastic strain and plastic damage with corrosion damage has been recognised as one of the current challenges in degradable material modelling (Gastaldi et al., 2011). A FE based plastic strain mediated phenomenological corrosion model was developed in this work and was calibrated based on the results of the corrosion experiments. It was found to be capable of predicting the experimentally observed plastic strain mediated mass loss profile and the corrosion-induced reduction in the radial stiffness of the stent over time. To the author's knowledge, the results presented here represent the first experimental calibration of a plastic strain mediated corrosion model of a corroding magnesium stent.

The results of this study provide new insights into the performance of an absorbable magnesium stent and the fundamental corrosion processes that lead to the temporal degradation of the stent. The findings will help direct future design efforts towards the minimisation of plastic strain during device manufacture, deployment and in-service, in order to reduce corrosion rates and prolong the mechanical integrity of magnesium devices. Improvements in the corrosion performance and biocompatibility of magnesium stents are needed and may be achieved through improved stent design, advances in metallurgy and materials processing, better surface treatments and coating strategies (Kitabata et al., 2014).

FE modelling is a powerful tool for device evaluation and corrosion simulations and is a requirement for FDA approval of many medical devices, such as coronary stents. Although the model developed in this work was validated and applied to the case of a WE43 stent, it can be readily adapted in order to study the behaviour of other alloys and devices. The model can also be used to examine the

effects of different materials processing, alloy compositions, and surface treatments on overall device performance. It provides a flexible modelling framework which can be adapted to explore other potentially relevant corrosion processes, such as pitting and crevice corrosion, through modification of the damage law (Eqn. 3.4).

6.2   Future Work

The influence of the surface treatments used in this study on the various surface properties which effect the biocompatibility of magnesium (Yang et al., 2011) require further investigation. Although a bare-metal magnesium stent platform, similar to the that developed in this work, demonstrated good biocompatibility in clinical trials (Erbel et al., 2007), the toxicology and metabolic pathway of the RE elements used in the WE43 alloy require further investigation (Gu and Zheng, 2010). Biocompatibility testing should include cytotoxicity, haemolysis and platelet adhesion testing, cell viability assays and additional corrosion analysis performed on specimens with materials processing and surface treatments that are relevant to stents. The work presented in this study should be advanced by carrying out experimental mechanical testing of strut-sized magnesium specimens, as has been investigated previously for traditional stent materials such as 316L (Murphy et al., 2003). However, the determination of specimen mass loss by gravimetric measurement at these size-scales represents a significant challenge. Hence, alternative approaches to determine specimen corrosion rates may be required such as Inductively Coupled Plasma Mass Spectrometry (ICP-MS) which can be used to measure the concentration of magnesium ions released into solution by corroding magnesium specimens (Schinhammer et al., 2010).

Drug-elution studies have shown that long-lasting antiproliferative effects do not require sustained drug release (Garg & Serruys, 2010). These findings suggest that effective magnesium BAS could be composed of an absorbable metal

backbone coated with an antiproliferative drug, rather than requiring drug wells or the inclusion of antiproliferative agents in the backbone material (Topol, 2008). The widespread adoption of magnesium stents requires improvements in device efficacy which could be achieved through the development of a biocompatible coating technology that permits control of drug delivery and device corrosion rate.

Since the study of plastic damage was the original application of the CDM approach, future CDM-based models of corrosion damage could contribute to exploring the interaction of plastic strain with corrosion damage for a range of absorbable magnesium devices. The various components of plastic strain that are induced during the processing of precursor tubes and stent manufacturing, as well as those that result from fatigue loading *in vivo*, could be used in future CDM models as the impetus for corrosion within the model. One approach might be to use deformation-induced changes in electrochemical measurements in the magnesium alloy as mediators of corrosion behaviour in the model. A number of studies have explored this relationship between deformation-induced electrochemical changes and corrosion behaviour in magnesium alloys (Snir et al., 2012; Wittke et al., 2014).

In the future, advanced imaging modalities and lower-cost screening tests may enable identification and pre-emptive treatment with BAS of patients with vulnerable plaques in order to reduce morbidity and mortality (Kukreja et al., 2009). The unique properties of magnesium devices will lead to new treatment options and improved outcomes for patients and should play a role in revolutionising medical devices (Farraro et al., 2013). Tissue engineering strategies may be combined with magnesium, such as the addition of biological agents to expedite healing of hard and soft tissues. Such devices could find utility in a host of implants such as coronary and ureteral stents (Lock et al., 2012), fracture fixation devices, ligament and tendon reconstruction implants (Walton and Cotton, 2007), sutures and ligatures (Seitz et al., 2011) and as bone substitutes (Krüger et al., 2013).

References

Abbas, G., Liu, Z., Skeldon, P., 2005. Corrosion behaviour of laser-melted magnesium alloys. Appl. Surf. Sci. 247, 347–353.

Abderrazak, K., Kriaa, W., Ben Salem, W., Mhiri, H., Lepalec, G., Autric, M., 2009. Numerical and experimental studies of molten pool formation during an interaction of a pulse laser (Nd:YAG) with a magnesium alloy. Opt. & Laser Technol. 41, 470–480.

Agema, W.R.P., Monraats, P.S., Zwinderman, A.H., De Winter, R.J., Tio, R. a, Doevendans, P. a F.M., Waltenberger, J., De Maat, M.P.M., Frants, R.R., Atsma, D.E., Van Der Laarse, A., Van Der Wall, E.E., Jukema, J.W., 2004. Current PTCA practice and clinical outcomes in The Netherlands: the real world in the pre-drug-eluting stent era. Eur. Heart J. 25, 1163–70. doi:10.1016/j.ehj.2004.05.006

Albaladejo, P., Samama, C.M., 2010. Patients under anti-platelet therapy. Best Pract. Res. Clin. Anaesthesiol. 24, 41–50. doi:10.1016/j.bpa.2009.09.008

Alqahtani, A., suwaidi, J., Mohsen, M., 2013. Stent fracture: How frequently is it recognized? Hear. Views 14, 72–81.

Alvarez-Lopez, M., Pereda, M.D., del Valle, J. a, Fernandez-Lorenzo, M., Garcia-Alonso, M.C., Ruano, O. a, Escudero, M.L., 2010. Corrosion behaviour of AZ31 magnesium alloy with different grain sizes in simulated biological fluids. Acta Biomater. 6, 1763–71. doi:10.1016/j.actbio.2009.04.041

Amira, S., Dubé, D., Tremblay, R., Ghali, E., 2008. Influence of the microstructure on the corrosion behavior of AXJ530 magnesium alloy in 3.5% NaCl solution. Mater. Charact. 59, 1508–1517. doi:10.1016/j.matchar.2008.01.018

Anis, R.R., Karsch, K.R., 2006. The future of drug eluting stents. Heart 92, 585–8. doi:10.1136/hrt.2005.068288

Ansys, 2010. Ansys Parametric Design Language (APDL) User Guide, Release 13.0.

Aoki, J., Nakazawa, G., Tanabe, K., Hoye, A., Yamamoto, H., Nakayama, T., Onuma, Y., Higashikuni, Y., Otsuki, S., Yagishita, A., Yachi, S., Nakajima, H., Hara, K., 2007. Incidence and clinical impact of coronary stent fracture after sirolimus-eluting stent implantation. doi:10.1002/ccd.20950

Arakawa, K., Isoda, K., Sugiyabu, Y., Fukuda, M., Nishizawa, K., Shibuya, T., Nakamura, H., 1998. Intimal proliferation after stenting reflected by increased stent-to-vessel cross-sectional area ratio: serial intravascular ultrasound study. J. Cardiol. 32, 379–389.

Argade, G.R., Panigrahi, S.K., Mishra, R.S., 2012. Effects of grain size on the corrosion resistance of wrought magnesium alloys containing neodymium. Corros. Sci. 58, 145–151. doi:10.1016/j.corsci.2012.01.021

Atrens, A., Liu, M., Zainal Abidin, N.I., 2011. Corrosion mechanism applicable to biodegradable magnesium implants. Mater. Sci. Eng. B 176, 1609–1636.

Avedesian, M.M., Baker, H., 1999. Magnesium & Magnesium Alloys. ASM International.

Bailey, S.R., 2009. DES Design: Theoretical Advantages and Disadvantages of Stent Strut Materials, Design, Thickness, and Surface Characteristics. J. Interv. Cardiol. 22, S3–S17. doi:10.1111/j.1540-8183.2009.00449.x

Berlin, J., 2011. Analysis of Boron with Energy Dispersive Spectrometry. Imaging Microsc. 13, 19–21.

Birrer, R.B., Shallash, A.J., 2002. Selected Topics : Toxicology HYPERMAGNESEMIA-INDUCED FATALITY FOLLOWING EPSOM SALT GARGLES 22, 185–188.

Bosiers, M., Deloose, K., Verbist, J., Peeters, P., 2005. First Clinical Application of Absorbable Metal Stents in the Treatment of Critical Limb Ischemia: 12-month results. Vasc. Dis. Manag. 2, 86–91.

Bosiers, M., Peeters, P., D'Archambeau, O., Hendriks, J., Pilger, E., Düber, C., Zeller, T., Gussmann, A., Lohle, P.N.M., Minar, E., Scheinert, D., Hausegger, K., Schulte, K.-L., Verbist, J., Deloose, K., Lammer, J., 2009. AMS INSIGHT-- absorbable metal stent implantation for treatment of below-the-knee critical limb ischemia: 6-month analysis. Cardiovasc. Intervent. Radiol. 32, 424–35. doi:10.1007/s00270-008-9472-8

Bowen, P.K., Drelich, J., Goldman, J., 2013. A new in vitro-in vivo correlation for bioabsorbable magnesium stents from mechanical behavior. Mater. Sci. Eng. C. Mater. Biol. Appl. 33, 5064–70. doi:10.1016/j.msec.2013.08.042

Bowen, P.K., Drelich, J., Goldman, J., 2014. Magnesium in the murine artery : Probing the products of corrosion. Acta Biomater. 10, 1475–83. doi:10.1016/j.actbio.2013.11.021

Bowen, P.K., Gelbaugh, J. a, Mercier, P.J., Goldman, J., Drelich, J., 2012. Tensile testing as a novel method for quantitatively evaluating bioabsorbable material degradation. J. Biomed. Mater. Res. B. Appl. Biomater. 100, 2101–13. doi:10.1002/jbm.b.32775

Briguori, C., Takahiro Nishida, Milena Adamian, Remo Albiero, Angelo Anzuini, Carlo Di Mario, Antonio Colombo, Nishida, T., Adamian, M., Albiero, R., Anzuini, A., Mario, C. Di, Colombo, A., 2000. Coronary stenting versus balloon angioplasty in small coronary artery with complex lesions. Catheter. Cardiovasc. Interv. 50, 390–397.

Castagna, M.T., Mintz, G.S., Leiboff, B.O., Ahmed, J.M., Mehran, R., Satler, L.F., Kent, K.M., Pichard, A.D., Weissman, N.J., 2001. The contribution of "mechanical" problems to in-stent restenosis: An intravascular ultrasonographic analysis of 1090 consecutive in-stent restenosis lesions. Am. Heart J. 142, 970–974.

Celik, T., Iyisoy, A., Jata, B., Yuksel, C.U., Isik, E., 2008. Stent fracture: A new villain of the village. Int. J. Cardiol. 138, 100–101.

Chen, Y., Song, Y., Zhang, S., Li, J., Zhao, C., Zhang, X., 2011. Interaction between a high purity magnesium surface and PCL and PLA coatings during dynamic degradation. Biomed. Mater. 6, 025005. doi:10.1088/1748-6041/6/2/025005

Chu, P.K., Chen, J.Y., Wang, L.P., Huang, N., 2002. Plasma-surface modification of biomaterials. Mater. Sci. Eng. … 36, 143–206.

Colombo, A., Cahill, P.A., Lally, C., 2009. The amplitude rather than mean strain determines the proliferative and apoptotic capacity of vascular smooth muscle cells in vitro. Communications 81, 2009.

Colombo, A., Guha, S., Mackle, J.N., Cahill, P. a, Lally, C., 2012. Cyclic strain amplitude dictates the growth response of vascular smooth muscle cells in vitro: role in in-stent restenosis and inhibition with a sirolimus drug-eluting stent. Biomech. Model. Mechanobiol. 12, 671–683. doi:10.1007/s10237-012-0433-4

Colombo, A., Karvouni, E., 2000. Biodegradable Stents : "Fulfilling the Mission and Stepping Away". Circulation 102, 371–373.

Colombo, A., Zahedmanesh, H., Toner, D.M., Cahill, P.A., Lally, C., 2010. A method to develop mock arteries suitable for cell seeding and in-vitro cell culture experiments. J. Mech. Behav. Biomed. Mater. 3, 470–477.

Connolley, T., McHugh, P.E., Bruzzi, M., 2005. A review of deformation and fatigue of metals at small size scales. Fatigue Fract. Eng. Mater. Struct. 28, 1119–1152. doi:10.1111/j.1460-2695.2005.00951.x

Coy, A.E., Viejo, F., Skeldon, P., Thompson, G.E., 2010. Susceptibility of rare-earth-magnesium alloys to micro-galvanic corrosion. Corros. Sci. 52, 3896–3906. doi:10.1016/j.corsci.2010.08.006

Dangas, G.D., Claessen, B.E., Caixeta, A., Sanidas, E. a, Mintz, G.S., Mehran, R., 2010. In-stent restenosis in the drug-eluting stent era. J. Am. Coll. Cardiol. 56, 1897–907. doi:10.1016/j.jacc.2010.07.028

Dangas, G.D., Serruys, P.W., Kereiakes, D.J., Hermiller, J., Rizvi, A., Newman, W., Sudhir, K., Smith, R.S., Cao, S., Theodoropoulos, K., Cutlip, D.E., Lansky, A.J., Stone, G.W., 2013. Meta-analysis of everolimus-eluting versus paclitaxel-eluting stents in coronary artery disease: final 3-year results of the SPIRIT clinical trials program (Clinical Evaluation of the Xience V Everolimus Eluting Coronary Stent System in the Treatment of P. JACC. Cardiovasc. Interv. 6, 914–22. doi:10.1016/j.jcin.2013.05.005

De Scheerder, I., Sohier, J., Froyen, L., Van Humbeeck, J., Verbeken, E., 2001. Biocompatibility of Coronary Stent Materials: Effect of Electrochemical Polishing. doi:10.1002/1521-4052(200102)32:2<142::aid-mawe142>3.0.co;2-n

Demir, A.G., Previtali, B., Biffi, C.A., 2013. Fibre Laser Cutting and Chemical Etching of AZ31 for Manufacturing Biodegradable Stents. Adv. Mater. Sci. Eng. 2013, 1–11.

Demir, A.G., Previtali, B., Colombo, D., Ge, Q., Vedani, M., Petrini, L., Wu, W., Biffi, C.A., 2012. Fiber laser micromachining of magnesium alloy tubes for biocompatible and biodegradable cardiovascular stents 823730–823739. doi:10.1117/12.910131

Deshpande, K.B., 2010. Validated numerical modelling of galvanic corrosion for couples: Magnesium alloy (AE44)–mild steel and AE44–aluminium alloy (AA6063) in brine solution. Corros. Sci. 52, 3514–3522. doi:10.1016/j.corsci.2010.06.031

Deshpande, K.B., 2011. Numerical modeling of micro-galvanic corrosion. Electrochim. Acta 56, 1737–1745. doi:10.1016/j.electacta.2010.09.044

Di Mario, C., Ferrante, G., 2008. Biodegradable drug-eluting stents: promises and pitfalls. Lancet 371, 873–874.

Di Mario, C., Griffiths, H., Goktekin, O., Peeters, N., Verbist, J., Bosiers, M., Deloose, K., Heublein, B., Rohde, R., Kasese, V., Ilsley, C., Erbel, R., 2004. Drug-eluting bioabsorbable magnesium stent. J. Interv. Cardiol. 17, 391–395. doi:JOIC4081 [pii] 10.1111/j.1540-8183.2004.04081.x

Dietzel, W., Pfuff, M., Winzer, N., 2010. Testing and mesoscale modelling of hydrogen assisted cracking of magnesium. Eng. Fract. Mech. 77, 257–263. doi:10.1016/j.engfracmech.2009.07.009

Draney, M.T., Herfkens, R.J., Hughes, T.J.R., Pelc, N.J., Wedding, K.L., Zarins, C.K., Taylor, C. a., 2002. Quantification of Vessel Wall Cyclic Strain Using Cine

Phase Contrast Magnetic Resonance Imaging. Ann. Biomed. Eng. 30, 1033–1045. doi:10.1114/1.1513566

Drenth, D.J., Winter, J.B., Veeger, N.J.G.M., Monnink, S.H.J., van Boven, A.J., Grandjean, J.G., Mariani, M. a., Boonstra, P.W., 2002. Minimally invasive coronary artery bypass grafting versus percutaneous transluminal coronary angioplasty with stenting in isolated high-grade stenosis of the proximal left anterior descending coronary artery: Six months' angiographic and clinical follow-u. J. Thorac. Cardiovasc. Surg. 124, 130–135. doi:10.1067/mtc.2002.122525

Drynda, A., Deinet, N., Braun, N., Peuster, M., 2009. Rare earth metals used in biodegradable magnesium-based stents do not interfere with proliferation of smooth muscle cells but do induce the upregulation of inflammatory genes. J. Biomed. Mater. Res. A 91, 360–9. doi:10.1002/jbm.a.32235

Duraiswamy, N., Schoephoerster, R.T., Moreno, M.R., Moore, J.E., 2007. Stented Artery Flow Patterns and Their Effects on the Artery Wall. Annu. Rev. Fluid Mech. 39, 357–382. doi:10.1146/annurev.fluid.39.050905.110300

Early, M., Lally, C., Prendergast, P.J., Kelly, D.J., 2009. Stresses in peripheral arteries following stent placement: a finite element analysis. Comput. Methods Biomech. Biomed. Engin. 12, 25–33. doi:10.1080/10255840802136135

Edelman, E.R., Rogers, C., 1998. Pathobiologic Responses to Stenting. Am. J. Cardiol. 81, 4E–6E.

Erbel, R., Di Mario, C., Bartunek, J., Bonnier, J., de Bruyne, B., Eberli, F.R., Erne, P., Haude, M., Heublein, B., Horrigan, M., Ilsley, C., Bose, D., Koolen, J., Luscher, T.F., Weissman, N., Waksman, R., 2007. Temporary scaffolding of coronary arteries with bioabsorbable magnesium stents: a prospective, non-randomised multicentre trial. Lancet 369, 1869–1875. doi:S0140-6736(07)60853-8 [pii] 10.1016/S0140-6736(07)60853-8

Erne, P., Schier, M., Resink, T.J., 2006. The road to bioabsorbable stents: reaching clinical reality? Cardiovasc Interv. Radiol 29, 11–16. doi:10.1007/s00270-004-0341-9

Fang, G., Ai, W., Leeflang, S., Duszczyk, J., Zhou, J., 2013. Multipass cold drawing of magnesium alloy minitubes for biodegradable vascular stents. Mater. Sci. Eng. C. Mater. Biol. Appl. 33, 3481–8. doi:10.1016/j.msec.2013.04.039

Farè, S., Ge, Q., Vedani, M., Vimercati, Ig., Gastaldi, D., Francesco Migliavacca; Lorenza Petrini; Stefano Trasatti, 2010. Evaluation of material properties and design requirements for biodegradable magnesium stents. Rev. Mater. 15, 96–103.

Farraro, K.F., Kim, K.E., Woo, S.L.-Y., Flowers, J.R., McCullough, M.B., 2013. Revolutionizing orthopaedic biomaterials: The potential of biodegradable and bioresorbable magnesium-based materials for functional tissue engineering. J. Biomech. doi:10.1016/j.jbiomech.2013.12.003

Feyerabend, F., Drücker, H., Laipple, D., Vogt, C., Stekker, M., Hort, N., Willumeit, R., 2012. Ion release from magnesium materials in physiological solutions under different oxygen tensions. J. Mater. Sci. Mater. Med. 23, 9–24. doi:10.1007/s10856-011-4490-5

Feyerabend, F., Fischer, J., Holtz, J., Witte, F., Willumeit, R., Drücker, H., Vogt, C., Hort, N., 2010. Evaluation of short-term effects of rare earth and other elements used in magnesium alloys on primary cells and cell lines. Acta Biomater. 6, 1834–1842.

Frey, T., Noster, U., Scholtes, B., Uggowitzer, P.J., 2005. Microstructural influences on the cyclic deformation behaviour of magnesium wrought alloys, in: H. Kaufmann (Ed.), Proc. of the 2nd Int. Conf. on Light Metals Technology. Springer Verlag, pp. 149 – 154.

Friedrich, H.E., Mordike, B.L. (Eds.), 2006. Magnesium Technology: Metallurgy, Design Data, Applications, eBook. ed. Springer Berlin Heidelberg.

Fuentes, J.C., Salmon, A. a, Silver, M. a, 2006. Acute and chronic oral magnesium supplementation: effects on endothelial function, exercise capacity, and quality of life in patients with symptomatic heart failure. Congest. Heart Fail. 12, 9–13.

Fung, Y.C., 1993. Biomechanics. Mechanical Properties of Living Tissues , 2nd ed. Springer-Verlag, New York.

Galvin, E., Morshed, M.M., Cummins, C., Daniels, S., Lally, C., MacDonald, B.J., 2013. Surface Modification of Absorbable Magnesium Stents by Reactive Ion Etching. J. Plasma Chem. Process. 33, 1137–1152. doi:10.1007/s11090-013-9477-1

Gastaldi, D., Sassi, V., Petrini, L., Vedani, M., Trasatti, S., Migliavacca, F., 2011. Continuum damage model for bioresorbable magnesium alloy devices -- Application to coronary stents. J. Mech. Behav. Biomed. Mater. 4, 352–365.

Ge, Q., Dellasega, D., Demir, A.G., Vedani, M., 2013. The processing of ultrafine-grained Mg tubes for biodegradable stents. Acta Biomater. 9, 8604–10. doi:10.1016/j.actbio.2013.01.010

Ge, Q., Vedani, M., Vimercati, G., 2011. Extrusion of Magnesium Tubes for Biodegradable Stent Precursors. Mater. Manuf. Process. 27, 140–146. doi:10.1080/10426914.2011.560231

Gerber, I., 2008. Metallic Medical Implants : Electrochemical Characterization of Corrosion Processes 35–40.

Go, A.S., Mozaffarian, D., Roger, V.L., Benjamin, E.J., Berry, J.D., Borden, W.B., Bravata, D.M., Dai, S., Ford, E.S., Fox, C.S., Franco, S., Fullerton, H.J., Gillespie, C., Hailpern, S.M., Heit, J. a, Howard, V.J., Huffman, M.D., Kissela, B.M., Kittner, S.J., Lackland, D.T., Lichtman, J.H., Lisabeth, L.D., Magid, D., Marcus, G.M., Marelli, A., Matchar, D.B., McGuire, D.K., Mohler, E.R., Moy, C.S., Mussolino, M.E., Nichol, G., Paynter, N.P., Schreiner, P.J., Sorlie, P.D., Stein, J., Turan, T.N., Virani, S.S., Wong, N.D., Woo, D., Turner, M.B., 2013. Heart disease and stroke statistics--2013 update: a report from the American Heart Association. Circulation 127, e6–e245. doi:10.1161/CIR.0b013e31828124ad

Gogas, B., Farooq, V., Onuma, Y., Serruys, P., 2012. The ABSORB bioresorbable vascular scaffold: an evolution or revolution in interventional cardiology. Hell. J Cardiol 53, 301–309.

Gogas, B.D., McDaniel, M., Samady, H., King, S.B., 2014. Novel Drug-Eluting Stents For Coronary Revascularization. Trends Cardiovasc. Med. doi:10.1016/j.tcm.2014.07.004

Gray-Munro, J.E., Seguin, C., Strong, M., 2009. Influence of surface modification on the in vitro corrosion rate of magnesium alloy AZ31. J. Biomed. Mater. Res. A 91, 221–30. doi:10.1002/jbm.a.32205

Grogan, J.A., Leen, S.B., McHugh, P.E., 2012. Comparing coronary stent material performance on a common geometric platform through simulated bench testing. J. Mech. Behav. Biomed. Mater. 12, 129–38. doi:10.1016/j.jmbbm.2012.02.013

Grogan, J.A., Leen, S.B., McHugh, P.E., 2013. Influence of statistical size effects on the plastic deformation of coronary stents. J. Mech. Behav. Biomed. Mater. 20, 61–76. doi:10.1016/j.jmbbm.2012.12.008

Grogan, J.A., Leen, S.B., McHugh, P.E., 2014a. A physical corrosion model for bioabsorbable metal stents. Acta Biomater. 10, 2313–2322. doi:10.1016/j.actbio.2013.12.059

Grogan, J.A., Leen, S.B., McHugh, P.E., 2014b. Computational micromechanics of bioabsorbable magnesium stents. J. Mech. Behav. Biomed. Mater. 34, 93–105. doi:10.1016/j.jmbbm.2014.01.007

Grogan, J.A., O'Brien, B.J., Leen, S.B., McHugh, P.E., 2011. A corrosion model for bioabsorbable metallic stents. Acta Biomater. 7, 3523–3533.

Gu, X.N., Zheng, Y.F., 2010. A review on magnesium alloys as biodegradable materials. Front. Mater. Sci. China 4, 111–115.

Gu, X.N., Zhou, W.R., Zheng, Y.F., Cheng, Y., Wei, S.C., Zhong, S.P., Xi, T.F., Chen, L.J., 2010. Corrosion fatigue behaviors of two biomedical Mg alloys - AZ91D and WE43 - In simulated body fluid. Acta Biomater. 6, 4605–4613.

Gunde, P., Hänzi, A.C., Sologubenko, A.S., Uggowitzer, P.J., 2011. High-strength magnesium alloys for degradable implant applications. Mater. Sci. Eng. A 528, 1047–1054.

Gundogan, B., Tan, A., Farhatnia, Y., Alavijeh, M.S., Cui, Z., Seifalian, A.M., 2014. Bioabsorbable stent quo vadis: a case for nano-theranostics. Theranostics 4, 514–33. doi:10.7150/thno.8137

Guo, L., Chen, Z., Gao, L., 2011. Effects of grain size, texture and twinning on mechanical properties and work-hardening behavior of AZ31 magnesium alloys. Mater. Sci. Eng. A 528, 8537–8545. doi:10.1016/j.msea.2011.07.076

Guo, L.F., Yue, T.M., Man, H.C., 2005. Excimer laser surface treatment of magnesium alloy WE43 for corrosion resistance improvement. J. Mater. Sci. 40, 3531–3533. doi:10.1007/s10853-005-2888-5

Guy, L., 2013. PRECLINICAL STUDIES OF UPCOMING BIORESORBABLE SCAFFOLDS Pre-clinical evaluation of the magnesium scaffold, in: EuroPCR.

Halfmann, H., Bibinov, N., Wunderlich, J., Awakowicz, P., 2007. A double inductively coupled plasma for sterilization of medical devices. J. Phys. D. Appl. Phys. 40, 4145–4154. doi:10.1088/0022-3727/40/14/008

Hänzi, A.C., Gerber, I., Schinhammer, M., Löffler, J.F., Uggowitzer, P.J., 2010. On the in vitro and in vivo degradation performance and biological response of new biodegradable Mg-Y-Zn alloys. Acta Biomater. 6, 1824–33. doi:10.1016/j.actbio.2009.10.008

Hänzi, A.C., Gunde, P., Schinhammer, M., Uggowitzer, P.J., 2009. On the biodegradation performance of an Mg-Y-RE alloy with various surface conditions in simulated body fluid. Acta Biomater. 5, 162–171.

Hara, H., Nakamura, M., Palmaz, J.C., Schwartz, R.S., 2006. Role of stent design and coatings on restenosis and thrombosis. Adv. Drug Deliv. Rev. 58, 377–86. doi:10.1016/j.addr.2006.01.022

Hartwig, a, 2001. Role of magnesium in genomic stability. Mutat. Res. 475, 113–21.

Hassel, T., Bach, F.W., Golovko, A.N., 2006. Production and Properties of Small Tubes Made From MgCa0.8 for Application as Stent in Biomedical Science, in: Kainer, K.U. (Ed.), 7th International Conference on Magnesium Alloys and

Their Applications. Wiley-VCH, Dresden, pp. 432–437.

Haude, M., Erbel, R., Erne, P., Verheye, S., Degen, H., Böse, D., Vermeersch, P., Wijnbergen, I., Weissman, N., Prati, F., Waksman, R., Koolen, J., 2013. Safety and performance of the drug-eluting absorbable metal scaffold (DREAMS) in patients with de-novo coronary lesions: 12 month results of the prospective, multicentre, first-in-man BIOSOLVE-I trial. Lancet 381, 836–844. doi:10.1016/S0140-6736(12)61765-6

Hermawan, H., Dubé, D., Mantovani, D., 2010a. Degradable metallic biomaterials: design and development of Fe–Mn alloys for stents. J. Biomed. … 1–10.

Hermawan, H., Dubé, D., Mantovani, D., 2010b. Developments in metallic biodegradable stents. Acta Biomater. 6, 1693–1697.

Hermawan, H., Mantovani, D., Dubé, D., Alamdari, A., 2008. Iron-Manganese: new class of metallic degradable biomaterials prepared by powder metallurgy. Powder Metall. 51, 38–45.

Heublein, B., Rohde, R., Kaese, V., Niemeyer, M., Hartung, W., Haverich, A., 2003. Biocorrosion of magnesium alloys: a new principle in cardiovascular implant technology? Heart 89, 651–656.

Hoffmann, R., Haager, P., Mintz, G.S., Kerckhoff, G., Schwarz, R., Franke, A., vom Dahl, J., Hanrath, P., 2001. The impact of high pressure vs low pressure stent implantation on intimal hyperplasia and follow-up lumen dimensions; results of a randomized trial. Eur. Heart J. 22, 2015–24. doi:10.1053/euhj.2001.2609

Hoffmann, R., Radke, P.W., Ortlepp, J.R., Haager, P.K., Blindt, R., Iofina, E., Franke, A., Langenberg, R., Weber, C., Hanrath, P., 2004. Intravascular ultrasonic comparative analysis of degree of intimal hyperplasia produced by four different stents in the coronary arteries. Am. J. Cardiol. 94, 1548–1550.

Holzapfel, G. a., Sommer, G., Regitnig, P., 2004. Anisotropic Mechanical Properties of Tissue Components in Human Atherosclerotic Plaques. J. Biomech. Eng. 126, 657. doi:10.1115/1.1800557

Holzapfel, G., Gasser, T., Ogden, R., 2000. A New Constitutive Framework for Arterial Wall Mechanics and a Comparative Study of Material Models. J. Elast. 61, 1–48. doi:10.1023/a:1010835316564

Holzapfel, G.A., Ogden, R.W., 2006. Mechanics of biological tissues. Springer-Verlag, Berlin.

Holzapfel, G.A., Sommer, G., Gasser, C.T., Regitnig, P., 2005. Determination of layer-specific mechanical properties of human coronary arteries with nonatherosclerotic intimal thickening and related constitutive modeling. Am. J. Physiol. - Hear. Circ. Physiol. 289, H2048–H2058. doi:10.1152/ajpheart.00934.2004

Hong, D., Saha, P., Chou, D.-T., Lee, B., Collins, B.E., Tan, Z., Dong, Z., Kumta, P.N., 2013. In vitro degradation and cytotoxicity response of Mg-4% Zn-0.5% Zr (ZK40) alloy as a potential biodegradable material. Acta Biomater. 9, 8534–47. doi:10.1016/j.actbio.2013.07.001

Hornberger, H., Virtanen, S., Boccaccini, A.R., 2012. Biomedical coatings on magnesium alloys - a review. Acta Biomater. doi:10.1016/j.actbio.2012.04.012

Hruby, A., McKeown, N.M., 2013. Bioactive Food as Dietary Interventions for Diabetes, Bioactive Food as Dietary Interventions for Diabetes. Elsevier. doi:10.1016/B978-0-12-397153-1.00032-9

Hunt, B., Poston, L., Schachter, M., Halliday, A., 2002. An introduction to vascular

biology; From basic science to clinical practice, Second. ed. Cambridge Press, UK.

Jabara, R., Pendyala, L., Chen, J., Chronos, N., 2009. Bioabsorbable Stents: The Future Is Near, A review of the breakthroughs and challenges of bioabsorbable stents as a potential solution to the risks associated with available drug-eluting stents. Card. Interv. Today June/July, 50–53.

Jain, A., Duygulu, O., Brown, D.W., Tomé, C.N., Agnew, S.R., 2008. Grain size effects on the tensile properties and deformation mechanisms of a magnesium alloy, AZ31B, sheet. Mater. Sci. Eng. A 486, 545–555. doi:10.1016/j.msea.2007.09.069

Jia, J.X., Song, G., Atrens, A., 2006. Influence of geometry on galvanic corrosion of AZ91D coupled to steel. Corros. Sci. 48, 2133–2153. doi:10.1016/j.corsci.2005.08.013

Ju, F., Xia, Z., Sasaki, K., 2008. On the finite element modelling of balloon-expandable stents. J. Mech. Behav. Biomed. Mater. 1, 86–95.

Kainer, K.U., 2003. Magnesium - Proceedings of the 7th International Conference on Magnesium Alloys and Their Applications (My Ref. Book 2). Wiley-VCH Verlag, Weinheim.

Kalb, H., Rzany, A., Hensel, B., 2012. Impact of microgalvanic corrosion on the degradation morphology of WE43 and pure magnesium under exposure to simulated body fluid. Corros. Sci. 57, 122–130. doi:10.1016/j.corsci.2011.12.026

Kandzari, D.E., Leon, M.B., Meredith, I., Fajadet, J., Wijns, W., Mauri, L., 2013. Final 5-year outcomes from the Endeavor zotarolimus-eluting stent clinical trial program: comparison of safety and efficacy with first-generation drug-eluting and bare-metal stents. JACC. Cardiovasc. Interv. 6, 504–12. doi:10.1016/j.jcin.2012.12.125

Kandzari, D.E., Tcheng, J.E., Zidar, J.P., 2002. Coronary artery stents: Evaluating new designs for contemporary percutaneous intervention. Catheter. Cardiovasc. Interv. 56, 562–576. doi:10.1002/ccd.10248

Kannan, M.B., 2010. Influence of microstructure on the in-vitro degradation behaviour of magnesium alloys. Mater. Lett. 64, 739–742.

Kannan, M.B., Dietzel, W., Blawert, C., Atrens, A., Lyon, P., 2008. Stress corrosion cracking of rare-earth containing magnesium alloys ZE41, QE22 and Elektron 21 (EV31A) compared with AZ80. Mater. Sci. Eng. A 480, 529–539.

Kastrati, A., Mehili, J., Dirschinger, J., 2001. Intracoronary stenting and angiographic results: strut thickness effect on restenosis outcomes (ISAR-STEREO) trial. ACC Curr. J. Rev. 10, 59.

Kern, M., 2012. Bioabsorbable Stents - Where are we now? Cath Lab Dig. 20, 4–6.

Kim, G.-H., Kim, C.-I., 2007. Dry etching of magnesium oxide thin films by using inductively coupled plasma for buffer layer of MFIS structure. Thin Solid Films 515, 4955–4959. doi:10.1016/j.tsf.2006.10.087

Kim, J.-S., Jang, I.-K., Fan, C., Kim, T.H., Kim, J.-S., Park, S.M., Choi, E.-Y., Lee, S.H., Ko, Y.-G., Choi, D., Hong, M.-K., Jang, Y., 2009. Evaluation in 3 months duration of neointimal coverage after zotarolimus-eluting stent implantation by optical coherence tomography: the ENDEAVOR OCT trial. JACC. Cardiovasc. Interv. 2, 1240–7. doi:10.1016/j.jcin.2009.10.006

Kirkland, N.T., Lespagnol, J., Birbilis, N., Staiger, M.P., 2010. A survey of bio-

corrosion rates of magnesium alloys. Corros. Sci. 52, 287–291.

Kitabata, H., Waksman, R., Warnack, B., 2014. Bioresorbable metal scaffold for cardiovascular application: Current knowledge and future perspectives. Cardiovasc. Revasc. Med. 15, 109–116. doi:10.1016/j.carrev.2014.01.011

Kraitzer, A., Kloog, Y., Zilberman, M., 2008. Approaches for prevention of restenosis. doi:10.1002/jbm.b.30974

Krawiec, H., Szklarz, Z., Vignal, V., 2012. Influence of applied strain on the microstructural corrosion of AlMg2 as-cast aluminium alloy in sodium chloride solution. Corros. Sci. 65, 387–396. doi:10.1016/j.corsci.2012.08.047

Krüger, R., Seitz, J.-M., Ewald, A., Bach, F.-W., Groll, J., 2013. Strong and tough magnesium wire reinforced phosphate cement composites for load-bearing bone replacement. J. Mech. Behav. Biomed. Mater. 20, 36–44. doi:10.1016/j.jmbbm.2012.12.012

Kukreja, N., Onuma, Y., Serruys, P.W., 2009. Future Directions of Drug-Eluting Stents. J. Interv. Cardiol. 22, S96–S105. doi:10.1111/j.1540-8183.2009.00455.x

Kutniy, K. V, Papirov, I.I., Tikhonovsky, M.A., Pikalov, A.I., Sivtzov, S. V, Pirozhenko, L.A., Shokurov, V.S., Shkuropatenko, V.A., 2009. Influence of grain size on mechanical and corrosion properties of magnesium alloy for medical implants Einfluss der Korngröße auf die mechanischen und korrosionstechnischen Eigenschaften von Magnesiumlegierungen für medizinische Implantate. Materwiss. Werksttech. 40, 242–246. doi:10.1002/mawe.200900434

Lally, C., Kelly, D.J., Prendergast, P.J., 2006. Stents, in: Wiley Encyclopedia of Biomedical Engineering. John Wiley & Sons, Inc. doi:10.1002/9780471740360.ebs1142

Lamaka, S.V., Montemor, M.F., Galio, a. F., Zheludkevich, M.L., Trindade, C., Dick, L.F., Ferreira, M.G.S., 2008. Novel hybrid sol–gel coatings for corrosion protection of AZ31B magnesium alloy. Electrochim. Acta 53, 4773–4783. doi:10.1016/j.electacta.2008.02.015

Levine, G.N., Bates, E.R., Blankenship, J.C., Bailey, S.R., Bittl, J. a., Cercek, B., Chambers, C.E., Ellis, S.G., Guyton, R. a., Hollenberg, S.M., Khot, U.N., Lange, R. a., Mauri, L., Mehran, R., Moussa, I.D., Mukherjee, D., Nallamothu, B.K., Ting, H.H., 2011. 2011 ACCF/AHA/SCAI Guideline for Percutaneous Coronary Intervention: Executive Summary. J. Am. Coll. Cardiol. 58, 2550–2583. doi:10.1016/j.jacc.2011.08.006

Lewington, S., Clarke, R., Qizilbash, N., Peto, R., Collins, R., 2003. Age-specific relevance of usual blood pressure to vascular mortality. Lancet 361, 1391–1392.

Li, J., Chen, R., Ma, Y., Ke, W., 2013. Effect of Zr modification on solidification behavior and mechanical properties of Mg–Y–RE (WE54) alloy. J. Magnes. Alloy. 1, 346–351. doi:10.1016/j.jma.2013.12.001

Li, J., Zheng, F., Qiu, X., Wan, P., Tan, L., Yang, K., 2014. Finite element analyses for optimization design of biodegradable magnesium alloy stent. Mater. Sci. Eng. C 42, 705–714. doi:10.1016/j.msec.2014.05.078

Li, N., Zhang, H., Ouyang, H., 2009. Shape optimization of coronary artery stent based on a parametric model. Finite Elem. Anal. Des. 45, 468–475.

Li, N., Zheng, Y., 2013. Novel Magnesium Alloys Developed for Biomedical

Application: A Review. J. Mater. Sci. Technol. 29, 489–502. doi:10.1016/j.jmst.2013.02.005

Lim, H., Hur, G., Kim, S., Kim, Y., Kwon, S., 2008. Coronary Stent Fracture: Detection with 64-Section Multidetector CT Angiography in Patients and in Vitro1. Radiology 249, 810–819.

Liu, L.J., Schlesinger, M., 2009. Corrosion of magnesium and its alloys. Corros. Sci. 51, 1733–1737. doi:10.1016/j.corsci.2009.04.025

Liu, M., Qiu, D., Zhao, M.-C., Song, G., Atrens, A., 2008. The effect of crystallographic orientation on the active corrosion of pure magnesium. Scr. Mater. 58, 421–424.

Liu, S.Y., Hu, J.D., Yang, Y., Guo, Z.X., Wang, H.Y., 2005. Microstructure analysis of magnesium alloy melted by laser irradiation. Appl. Surf. Sci. 252, 1723–1731. doi:10.1016/j.apsusc.2005.03.110

Lock, J.Y., Draganov, M., Whall, A., Dhillon, S., Upadhyayula, S., Vullev, V.I., Liu, H., 2012. Antimicrobial properties of biodegradable magnesium for next generation ureteral stent applications. Conf. Proc. IEEE Eng. Med. Biol. Soc. 2012, 1378–81. doi:10.1109/EMBC.2012.6346195

Lunder, O., Lein, J.E., Hesjevik, S.M., Aune, T.K., Nisancioglu, K., 1994. Corrosion morphologies on magnesium alloy AZ 91. Mater. Corros. 45, 331–340.

Ma, J., Thompson, M., Zhao, N., Zhu, D., 2014. Similarities and differences in coatings for magnesium-based stents and orthopaedic implants. J. Orthop. Transl. doi:10.1016/j.jot.2014.03.004

Macdonald, D.D., 1994. Performance Comparison Between a Statistical Model a Deterministic Model , and an Artificial Neural Network Model for Predicting Damage From Pitting Corrosion. J. Res. Natl. Inst. Stand. Technol. 99.

Magnesium Elektron, 2007. Material Datasheet WE43B, Magnesium Elektron, http://www.magnesium-elektron.com/, February 2007.

Martini, F.H., 2006. Fundamentals of Anatomy and Physiology, 7th ed. Pearson Education, San Francisco USA.

Mathers, T.W., Beckstrand, R.L., 2009. Oral magnesium supplementation in adults with coronary heart disease or coronary heart disease risk. J. Am. Acad. Nurse Pract. 21, 651–7. doi:10.1111/j.1745-7599.2009.00460.x

Mercado, N., Boersma, E., Wijns, W., Gersh, B.J., Morillo, C.A., de Valk, V., van Es, G.-A., Grobbee, D.E., Serruys, P.W., 2001. Clinical and quantitative coronary angiographic predictors of coronary restenosis: A comparative analysis from the balloon-to-stent era. J. Am. Coll. Cardiol. 38, 645–652.

Migliavacca, F., Petrini, L., Colombo, M., Auricchio, F., Pietrabissa, R., 2002. Mechanical behavior of coronary stents investigated through the finite element method. J. Biomech. 35, 803–811.

Moitra, A., 2013. Grain size effect on microstructural properties of 3D nanocrystalline magnesium under tensile deformation. Comput. Mater. Sci. 79, 247–251. doi:10.1016/j.commatsci.2013.05.051

Montoya, R., Iglesias, C., Escudero, M.L., García-Alonso, M.C., 2014. Modeling in vivo corrosion of AZ31 as temporary biodegradable implants. Experimental validation in rats. Mater. Sci. Eng. C. Mater. Biol. Appl. 41, 127–33. doi:10.1016/j.msec.2014.04.033

Moravej, M., Prima, F., Fiset, M., Mantovani, D., 2010a. Electroformed iron as new

biomaterial for degradable stents: Development process and structure-properties relationship. Acta Biomater. 6, 1726–1735.

Moravej, M., Purnama, A., Fiset, M., Couet, J., Mantovani, D., 2010b. Electroformed pure iron as a new biomaterial for degradable stents: In vitro degradation and preliminary cell viability studies. Acta Biomater. 6, 1843–1851.

Morshed, M.M., Alam, M.M., Daniels, S.M., 2011. Moisture Removal from Natural Jute Fibre by Plasma Drying Process. Plasma Chem. Plasma Process. 32, 249–258. doi:10.1007/s11090-011-9340-1

Morton, A.C., Crossman, D., Gunn, J., 2004. The influence of physical stent parameters upon restenosis. Pathol. Biol. (Paris). 52, 196–205. doi:10.1016/j.patbio.2004.03.013

Murphy, B.P., Savage, P., McHugh, P.E., Quinn, D.F., 2003. The Stress–Strain Behavior of Coronary Stent Struts is Size Dependent. Ann. Biomed. Eng. 31, 686–691. doi:10.1114/1.1569268

Nakamura, Y., Suzuki, Y., Watanabe, Y., 1996. Effect of oxygen plasma etching on adhesion between polyimide films and metal. Thin Solid Films 290-291, 367–369.

Nascimento, M., Zeddies, M., 2007. Magnesium and its alloys as degradable biomaterials: corrosion studies using potentiodynamic and EIS electrochemical techniques. Materials (Basel). 10.

Nichols, W.W., O'Rourke, M.F., Vlachopoulos, C., 2005. McDonald's blood flow in arteries: theoretical, experimental, and clinical principles, 6th ed. Hodder Arnold, New York.

Nishimoto, K.T., 2003. A study of plasma etching for use in active metals. Massachusetts Institute of Technology.

Nishinari, M., Shimohama, T., Tojo, T., Shiono, T., Shinagawa, H., Kameda, R., Aoyama, N., Izumi, T., 2013. Two-week interval optical coherence tomography: imaging evidence on neointimal coverage completion after implantation of the Endeavor zotarolimus-eluting stent. Catheter. Cardiovasc. Interv. 82, E871–8. doi:10.1002/ccd.25136

Nishio, S., Kosuga, K., Igaki, K., Okada, M., Kyo, E., Tsuji, T., Takeuchi, E., Inuzuka, Y., Takeda, S., Hata, T., Takeuchi, Y., Kawada, Y., Harita, T., Seki, J., Akamatsu, S., Hasegawa, S., Bruining, N., Brugaletta, S., de Winter, S., Muramatsu, T., Onuma, Y., Serruys, P.W., Ikeguchi, S., 2012. Long-Term (>10 Years) clinical outcomes of first-in-human biodegradable poly-l-lactic acid coronary stents: Igaki-Tamai stents. Circulation 125, 2343–53. doi:10.1161/CIRCULATIONAHA.110.000901

Nwaogu, U.C., Blawert, C., Scharnagl, N., Dietzel, W., Kainer, K.U., 2009. Influence of inorganic acid pickling on the corrosion resistance of magnesium alloy AZ31 sheet. Corros. Sci. 51, 2544–2556. doi:10.1016/j.corsci.2009.06.045

O'Brien, B., Carroll, W., 2009. The evolution of cardiovascular stent materials and surfaces in response to clinical drivers: A review. Acta Biomater. 5, 945–958.

O'Riordan, M., 2006. Disappearing act: Bioabsorbable magnesium-alloy stent safe to implant. theHeart.org.

Oberhofer, G., Gese, H., Groß, M., Kühling, M., Seidel, D., 2006. Numerical Analysis of the Balloon Dilatation Process Using the Explicit Finite Element Method for the Optimization of a Stent Geometry, in: Proceedings of LS-DYNA Anwenderforum. Ulm, pp. 35–46.

Ong, A.T.L., Hoye, A., Aoki, J., van Mieghem, C.A.G., Rodriguez Granillo, G.A., Sonnenschein, K., Regar, E., McFadden, E.P., Sianos, G., van der Giessen, W.J., de Jaegere, P.P.T., de Feyter, P., van Domburg, R.T., Serruys, P.W., 2005. Thirty-day incidence and six-month clinical outcome of thrombotic stent occlusion after bare-metal, sirolimus, or paclitaxel stent implantation. J. Am. Coll. Cardiol. 45, 947–953.

Onuma, Y., Serruys, P.W., 2011. Bioresorbable Scaffold: The Advent of a New Era in Percutaneous Coronary and Peripheral Revascularization? Circulation 123, 779–797. doi:10.1161/circulationaha.110.971606

Pachla, W., Mazur, a., Skiba, J., Kulczyk, M., Przybysz, S., 2012. Wrought Magnesium Alloys ZM21, ZW3 and WE43 Processed by Hydrostatic Extrusion with Back Pressure. Arch. Metall. Mater. 57. doi:10.2478/v10172-012-0050-3

Palmerini, T., Biondi-Zoccai, G., Della Riva, D., Mariani, A., Sabaté, M., Smits, P.C., Kaiser, C., D'Ascenzo, F., Frati, G., Mancone, M., Genereux, P., Stone, G.W., 2014. Clinical outcomes with bioabsorbable polymer- versus durable polymer-based drug-eluting and bare-metal stents: evidence from a comprehensive network meta-analysis. J. Am. Coll. Cardiol. 63, 299–307. doi:10.1016/j.jacc.2013.09.061

Peuster, M., Hesse, C., Schloo, T., Fink, C., Beerbaum, P., von Schnakenburg, C., 2006. Long-term biocompatibility of a corrodible peripheral iron stent in the porcine descending aorta. Biomaterials 27, 4955–4962.

Peuster, M., Wohlsein, P., Brugmann, M., Ehlerding, M., Seidler, K., Fink, C., Brauer, H., Fischer, A., Hausdorf, G., 2001. A novel approach to temporary stenting: degradable cardiovascular stents produced from corrodible metal-results 6-18 months after implantation into New Zealand white rabbits. Heart 86, 563–569.

Pierson, D., Edick, J., Tauscher, A., Pokorney, E., Bowen, P., Gelbaugh, J., Stinson, J., Getty, H., Lee, C.H., Drelich, J., Goldman, J., 2011. A simplified in vivo approach for evaluating the bioabsorbable behavior of candidate stent materials. J. Biomed. Mater. Res. Part B Appl. Biomater. 100, 58–67. doi:10.1002/jbm.b.31922

Poncin, P., Proft, J., 2003. Stent Tubing: Understanding the Desired Attributes. Proc. ASM Conf. Mater. Process. Med. Devices 253–259.

Ratner, B.D., Hoffman, A.S., Schoen, F.J., Lemons, J.E., 1996. Biomaterials science: an introduction to materials in medicine. Academic Press, San Diego.

Raulea, L.V., Goijaerts, A.M., 2001. Size effects in the processing of thin metal sheets. … Mater. Process. … 115, 44–48. doi:10.1016/S0924-0136(01)00770-1

Rettig, R., Virtanen, S., 2009. Composition of corrosion layers on a magnesium rare-earth alloy in simulated body fluids. J. Biomed. Mater. Res. A 88, 359–69. doi:10.1002/jbm.a.31887

Sabate, M., 2014. Absorb STEMI - TROF II: The use of Bioresorbable Scaffolds in Acute STEMI, in: EuroPCR Online.

Sabir, M., Liu, E.B., Li, Z., Zheng, Y.F., Li, L., 2012. Magnesium Alloy Stent Expansion Behavior Simulated by Finite Element Method. Appl. Mech. Mater. 232, 697–700. doi:10.4028/www.scientific.net/AMM.232.697

Sammel, A.M., Chen, D., Jepson, N., 2013. New generation coronary stent technology--is the future biodegradable? Heart. Lung Circ. 22, 495–506. doi:10.1016/j.hlc.2013.02.008

Sangiorgi, G., Melzi, G., Agostoni, P., Cola, C., Clementi, F., Romitelli, P., Virmani, R., Colombo, A., 2007. Engineering aspects of stents design and their translation into clinical practice. Ann. Ist. Super. Sanita 43, 89–100.

Santhanakrishnan, S., Kumar, N., Dendge, N., Choudhuri, D., Katakam, S., Palanivel, S., Vora, H.D., Banerjee, R., Mishra, R.S., Dahotre, N.B., 2013. Macro- and Microstructural Studies of Laser-Processed WE43 (Mg-Y-Nd) Magnesium Alloy. Metall. Mater. Trans. B 44, 1190–1200. doi:10.1007/s11663-013-9896-7

Savage, M.P., Fischman, D.L., Schatz, R.A., Teirstein, P.S., Leon, M.B., Baim, D., Ellis, S.G., Topol, E.J., Hirshfeld, J.W., Cleman, M.W., 1994. Long-term angiographic and clinical outcome after implantation of a balloon-expandable stent in the native coronary circulation. Palmaz-Schatz Stent Study Group. J Am Coll Cardiol 24, 1207–1212.

Savage, P., O'Donnell, B.P., McHugh, P.E., Murphy, B.P., Quinn, D.F., 2004. Coronary stent strut size dependent stress-strain response investigated using micromechanical finite element models. Ann. Biomed. Eng. 32, 202–11.

Schinhammer, M., Hänzi, A.C., Löffler, J.F., Uggowitzer, P.J., 2010. Design strategy for biodegradable Fe-based alloys for medical applications. Acta Biomater. 6, 1705–1713.

Schulz, C., Herrmann, R. a, Beilharz, C., Pasquantonio, J., Alt, E., 2000. Coronary stent symmetry and vascular injury determine experimental restenosis. Heart 83, 462–7.

Schwartz, R.S., Holmes Jr, D.R., Topol, E.J., 1992. The restenosis paradigm revisited: An alternative proposal for cellular mechanisms. J. Am. Coll. Cardiol. 20, 1284–1293.

Scott, N. a, 2006. Restenosis following implantation of bare metal coronary stents: pathophysiology and pathways involved in the vascular response to injury. Adv. Drug Deliv. Rev. 58, 358–76. doi:10.1016/j.addr.2006.01.015

Seitz, J.-M., Eifler, R., Stahl, J., Kietzmann, M., Bach, F.-W., 2012. Characterization of MgNd2 alloy for potential applications in bioresorbable implantable devices. Acta Biomater. 8, 3852–64. doi:10.1016/j.actbio.2012.05.024

Seitz, J.-M., Utermöhlen, D., Wulf, E., Klose, C., Bach, F.-W., 2011. The Manufacture of Resorbable Suture Material from Magnesium – Drawing and Stranding of Thin Wires. Adv. Eng. Mater. 13, 1087–1095. doi:10.1002/adem.201100152

Serruys, P.W., de Jaegere, P., Kiemeneij, F., Macaya, C., Rutsch, W., Heyndrickx, G., Emanuelsson, H., Marco, J., Legrand, V., Materne, P., Belardi, J., Sigwart, U., Colombo, A., Goy, J.J., van den Heuvel, P., Delcan, J., Morel, M., 1994. A Comparison of Balloon-Expandable-Stent Implantation with Balloon Angioplasty in Patients with Coronary Artery Disease. N. Engl. J. Med. 331, 489–495. doi:doi:10.1056/NEJM199408253310801

Sianos, G., Hofma, S., Ligthart, J.M.R., Saia, F., Hoye, A., Lemos, P.A., Serruys, P.W., 2004. Stent fracture and restenosis in the drug-eluting stent era. Catheter. Cardiovasc. Interv. 61, 111–116. doi:10.1002/ccd.10709

Snir, Y., Ben-Hamu, G., Eliezer, D., Abramov, E., 2012. Effect of compression deformation on the microstructure and corrosion behavior of magnesium alloys. J. Alloys Compd. 528, 84–90. doi:10.1016/j.jallcom.2012.03.010

Song, G., 1999. Corrosion mechanisms of magnesium alloys. Adv. Eng. Mater. 11–33.

Song, G., Atrens, a., 2003. Understanding Magnesium Corrosion—A Framework for Improved Alloy Performance. Adv. Eng. Mater. 5, 837–858. doi:10.1002/adem.200310405

Song, G., Atrens, a., 2007. Recent Insights into the Mechanism of Magnesium Corrosion and Research Suggestions. Adv. Eng. Mater. 9, 177–183. doi:10.1002/adem.200600221

Song, G., Atrens, A., 1999. Corrosion mechanisms of magnesium alloys. Adv. Eng. Mater. 1, 11–33. doi:10.1002/(SICI)1527-2648(199909)1:1<11::AID-ADEM11>3.3.CO;2-E

Song, G., Atrens, A., Dargusch, M., 1999. Influence of microstructure on the corrosion of diecast AZ91D. Corros. Sci. 41, 138–162.

Song, G.L., 2011. Corrosion of Magnesium Alloys. Woodhead Publishing, Oxford Philadelphia, PA.

Song, G.-L., Xu, Z., 2012. Crystal orientation and electrochemical corrosion of polycrystalline Mg. Corros. Sci. 63, 100–112. doi:10.1016/j.corsci.2012.05.019

Stack, R.E., Califf, R.M., Phillips, H.R., 1988. Interventional cardiac catheterization at Duke Medical Center. Am J Cardiol .

Staiger, M.P., Pietak, A.M., Huadmai, J., Dias, G., 2006. Magnesium and its alloys as orthopedic biomaterials: a review. Biomaterials 27, 1728–1734.

Sternberg, K., Gratz, M., Koeck, K., Mostertz, J., Begunk, R., Loebler, M., Semmling, B., Seidlitz, A., Hildebrandt, P., Homuth, G., Grabow, N., Tuemmler, C., Weitschies, W., Schmitz, K.-P., Kroemer, H.K., 2011. Magnesium used in bioabsorbable stents controls smooth muscle cell proliferation and stimulates endothelial cells in vitro. J. Biomed. Mater. Res. Part B Appl. Biomater. 100B, 41–50. doi:10.1002/jbm.b.31918

Stone, G., Ellis, S., Cox, D., 2004. A polymer-based, paclitaxel-eluting stent in patients with coronary artery disease. … Engl. J. … 350, 221–231.

Sun, W., Wang, L., Wu, T., Liu, G., 2014. An arbitrary Lagrangian–Eulerian model for modelling the time-dependent evolution of crevice corrosion. Corros. Sci. 78, 233–243. doi:10.1016/j.corsci.2013.10.003

Svilaas, T., van der Horst, I.C.C., Zijlstra, F., 2007. A quantitative estimate of bare-metal stenting compared with balloon angioplasty in patients with acute myocardial infarction: angiographic measures in relation to clinical outcome. Heart 93, 792–800. doi:10.1136/hrt.2006.093740

Tamai, H., Igaki, K., Kyo, E., Kosuga, K., Kawashima, A., Matsui, S. et al., 2000. Initial and 6-month results of biodegradable poly-l-lactid acid coronary sents in humans. J Am Hear. Assoc.

Thamida, S.K., 2012. Modeling and simulation of galvanic corrosion pit as a moving boundary problem. Comput. Mater. Sci. 65, 269–275. doi:10.1016/j.commatsci.2012.07.029

Topol, E.J., 2008. Textbook of Interventional Cardiology, 5th Ed. ed. Elsevier Inc., Philadelphia.

Transparency Market Research, 2014. Coronary Stents Market (Bare Metal Stents, Drug Eluting Stents and Bio-absorbable Stents) - Global Industry Analysis, Size, Share, Pipeline Overview, Growth, Trends and Forecast, 2013 - 2019.

Ulvrová, M., Labrosse, S., Coltice, N., Råback, P., Tackley, P.J., 2012. Numerical modelling of convection interacting with a melting and solidification front:

Application to the thermal evolution of the basal magma ocean. Phys. Earth Planet. Inter. 206-207, 51–66. doi:10.1016/j.pepi.2012.06.008

Valente, T., 2001. Grain boundary effects on the behavior of WE43 magnesium castings. Corrosion 67–69.

Vedani, M., Ge, Q., Wu, W., Petrini, L., 2012. Texture effects on design of Mg biodegradable stents. Int. J. Mater. Form. 7, 31–38. doi:10.1007/s12289-012-1108-5

Vernhet, H., Demaria, R., Juan, J.M., Oliva-Lauraire, M.C., Sénac, J.P., Dauzat, M., 2001. Changes in Wall Mechanics After Endovascular Stenting in the Rabbit Aorta. Am. J. Roentgenol. 176, 803–807.

Vernhet, H., Juan, J.M., Demaria, R., Oliva-Lauraire, M.C., Sénac, J.P., Dauzat, M., 2000. Acute Changes in Aortic Wall Mechanical Properties after Stent Placement in Rabbits. J. Vasc. Interv. Radiol. 11, 634–638.

Waksman, R., 2011. The Biotronik Bioabsorbable Magnesium Scaffold DREAMS, in: TCTAP 2011. Seoul, Korea.

Waksman, R., Erbel, R., Di Mario, C., Bartunek, J., de Bruyne, B., Eberli, F.R., Erne, P., Haude, M., Horrigan, M., Ilsley, C., Böse, D., Bonnier, H., Koolen, J., Lüscher, T.F., Weissman, N.J., 2009. Early- and Long-Term Intravascular Ultrasound and Angiographic Findings After Bioabsorbable Magnesium Stent Implantation in Human Coronary Arteries. J. Am. Coll. Cardiol. Cardiovasc. Interv. 2, 312–320.

Waksman, R., Pakala, R., Kuchulakanti, P.K., Baffour, R., Hellinga, D., Seabron, R., Tio, F.O., Wittchow, E., Hartwig, S., Harder, C., Rohde, R., Heublein, B., Andreae, A., Waldmann, K.H., Haverich, A., 2006. Safety and efficacy of bioabsorbable magnesium alloy stents in porcine coronary arteries. Catheter Cardiovasc Interv 68, 607–609. doi:10.1002/ccd.20727

Walter, R., Kannan, M.B., 2010. Influence of surface roughness on the corrosion behaviour of magnesium alloy. Mater. Des. 32, 2350–2354.

Walter, R., Kannan, M.B., He, Y., Sandham, a., 2013. Effect of surface roughness on the in vitro degradation behaviour of a biodegradable magnesium-based alloy. Appl. Surf. Sci. 279, 343–348. doi:10.1016/j.apsusc.2013.04.096

Walton, C. a., Horstemeyer, M.F., Martin, H.J., Francis, D.K., 2014. Formulation of a macroscale corrosion damage internal state variable model. Int. J. Solids Struct. 51, 1235–1245. doi:10.1016/j.ijsolstr.2013.12.007

Wang, H., Estrin, Y., Fu, H., Song, G., Zúberová, Z., 2007. The Effect of Pre-Processing and Grain Structure on the Bio-Corrosion and Fatigue Resistance of Magnesium Alloy AZ31. Adv. Eng. Mater. 9, 967–972. doi:10.1002/adem.200700200

Wang, J., He, Y., Maitz, M.F., Collins, B., Xiong, K., Guo, L., Yun, Y., Wan, G., Huang, N., 2013. A surface-eroding poly(1,3-trimethylene carbonate) coating for fully biodegradable magnesium-based stent applications: toward better biofunction, biodegradation and biocompatibility. Acta Biomater. 9, 8678–89. doi:10.1016/j.actbio.2013.02.041

Wang, X., Cui, F., Li, J., Zhao, X., 2009. [Mechanical analysis on a new type of biodegradable magnesium-alloy stent]. Sheng Wu Yi Xue Gong Cheng Xue Za Zhi 26, 338–341.

Weiß, S., Szymczak, H., Meißner, A., 2009. Fatigue and endurance of coronary stents. doi:10.1002/mawe.200800409

Welt, F.G.P., Rogers, C., 2002. Inflammation and Restenosis in the Stent Era. Arterioscler. Thromb. Vasc. Biol. 22, 1769–1776. doi:10.1161/01.ATV.0000037100.44766.5B

Wiersma, S.A., Taylor, D., 2004. A critical distance approach applied to microscopic 316L biomedical specimens under fatigue loading, in: The 15th European Conference of Fracture-Advanced Fracture Mechanics for Life and Safety Assessments. Sweden.

Willbold, E., Kalla, K., Bartsch, I., Bobe, K., Brauneis, M., Remennik, S., Shechtman, D., Nellesen, J., Tillmann, W., Vogt, C., Witte, F., 2013. Biocompatibility of rapidly solidified magnesium alloy RS66 as a temporary biodegradable metal. Acta Biomater. 9, 8509–17. doi:10.1016/j.actbio.2013.02.015

Williams, D., 2006. New interests in magnesium. Med Device Technol 17, 9–10.

Winzer, N., Atrens, a, Dietzel, W., Raja, V., Song, G., Kainer, K., 2008. Characterisation of stress corrosion cracking (SCC) of Mg–Al alloys. Mater. Sci. Eng. A 488, 339–351. doi:10.1016/j.msea.2007.11.064

Winzer, N., Atrens, a., Song, G., Ghali, E., Dietzel, W., Kainer, K.U., Hort, N., Blawert, C., 2005a. A Critical Review of the Stress Corrosion Cracking (SCC) of Magnesium Alloys. Adv. Eng. Mater. 7, 659–693. doi:10.1002/adem.200500071

Winzer, N., Atrens, A., Dietzel, W., Song, G., Kainer, K.U., 2007. Stress corrosion cracking in magnesium alloys: Characterization and prevention. Jom 59, 49–53. doi:10.1007/s11837-007-0104-6

Winzer, N., Atrens, A., Song, G., Ghali, E., Dietzel, W., Kainer, K.U., Hort, N., Blawert, C., 2005b. A Critical Review of the Stress Corrosion Cracking (SCC) of Magnesium Alloys. Adv. Eng. Mater. 7, 659–693. doi:10.1002/adem.200500071

Wittchow, E., Adden, N., Riedmüller, J., Savard, C., Waksman, R., Braune, M., 2013. Bioresorbable drug-eluting magnesium-alloy scaffold: design and feasibility in a porcine coronary model. EuroIntervention 8, 1441–50. doi:10.4244/EIJV8I12A218

Witte, F., 2010. The history of biodegradable magnesium implants: A review. Acta Biomater. 6, 1680–1692.

Witte, F., Hort, N., Vogt, C., Cohen, S., Kainer, K.U., Willumeit, R., Feyerabend, F., 2008. Degradable biomaterials based on magnesium corrosion. Curr. Opin. Solid State Mater. Sci. 12, 63–72. doi:10.1016/j.cossms.2009.04.001

Wittke, P., Klein, M., Walther, F., 2014. Corrosion Fatigue Behaviour of Creep-resistant Magnesium Alloy Mg-4Al-2Ba-2Ca. Procedia Eng. 74, 78–83. doi:10.1016/j.proeng.2014.06.228

Wu, Q., Zhu, S., Wang, L., Liu, Q., Yue, G., Wang, J., Guan, S., 2012. The microstructure and properties of cyclic extrusion compression treated Mg-Zn-Y-Nd alloy for vascular stent application. J. Mech. Behav. Biomed. Mater. 8, 1–7. doi:10.1016/j.jmbbm.2011.12.011

Wu, W., Chen, S., Gastaldi, D., Petrini, L., 2012. Experimental data confirm numerical modeling on degradation process of magnesium alloys stents. Acta Biomater. doi:10.1016/j.actbio.2012.10.035.

Wu, W., Gastaldi, D., Yang, K., Tan, L., Petrini, L., Migliavacca, F., 2011. Finite element analyses for design evaluation of biodegradable magnesium alloy stents in arterial vessels. Mater. Sci. Eng. B 176, 1733–1740.

Wu, W., Petrini, L., Gastaldi, D., Villa, T., Vedani, M., Lesma, E., Previtali, B., Migliavacca, F., 2010. Finite Element Shape Optimization for Biodegradable Magnesium Alloy Stents. Ann. Biomed. Eng. 38, 2829–2840. doi:10.1007/s10439-010-0057-8

Xia, Z., Ju, F., Sasaki, K., 2007. A general finite element analysis method for balloon expandable stents based on repeated unit cell (RUC) model. Finite Elem. Anal. Des. 43, 649–658.

Xin, Y., Huo, K., Tao, H., Tang, G., Chu, P.K., 2008. Influence of aggressive ions on the degradation behavior of biomedical magnesium alloy in physiological environment. Acta Biomater. 4, 2008–2015.

Xu, L., Yamamoto, A., 2012. Characteristics and cytocompatibility of biodegradable polymer film on magnesium by spin coating. Colloids Surf. B. Biointerfaces 93, 67–74. doi:10.1016/j.colsurfb.2011.12.009

Xue, Y., Horstemeyer, M., Mcdowell, D., Elkadiri, H., Fan, J., 2007. Microstructure-based multistage fatigue modeling of a cast AE44 magnesium alloy. Int. J. Fatigue 29, 666–676. doi:10.1016/j.ijfatigue.2006.07.005

Yang, J., Cui, F., Lee, I.S., 2011. Surface modifications of magnesium alloys for biomedical applications. Ann. Biomed. Eng. 39, 1857–1871.

Yang, J., Cui, F., Lee, I.S., Wang, X., 2010. Plasma surface modification of magnesium alloy for biomedical application. Surf. Coatings Technol. 205, S182–S187. doi:10.1016/j.surfcoat.2010.07.045

Yang, L., Zhang, E., 2009. Biocorrosion behavior of magnesium alloy in different simulated fluids for biomedical application. Mater. Sci. Eng. C 29, 1691–1696. doi:10.1016/j.msec.2009.01.014

Yang, Z., Li, J.P., Zhang, J.X., Lorimer, G.W., Robson, J., 2008. Review on Research and Development of Magnesium Alloys. Acta Metall. Sin. (English Lett. 21, 313–328.

Yi, C.H., Jeong, C.H., Lee, Y.H., Ko, Y.W., Yeom, G.Y., 2004. Oxide surface cleaning by an atmospheric pressure plasma. Surf. Coatings Technol. 177-178, 711–715. doi:10.1016/j.surfcoat.2003.08.011

Yusuf, S., Hawken, S., Ounpuu, S., Dans, T., Avezum, A., Lanas, F., McQueen, M., Budaj, A., Pais, P., Varigos, J., Lisheng, L., 2004. Effect of potentially modifiable risk factors associated with myocardial infarction in 52 countries (the INTERHEART study): case-control study. Lancet 364, 937–52. doi:10.1016/S0140-6736(04)17018-9

Yutani, C., Imakita, M., Ishibashi-Ueda, H., Tsukamoto, Y., Nishida, N., Ikeda, Y., 1999. Coronary atherosclerosis and interventions: Pathological sequences and restenosis. Pathol. Int. 49, 273–290. doi:10.1046/j.1440-1827.1999.00861.x

Zahedmanesh, H., John Kelly, D., Lally, C., 2010. Simulation of a balloon expandable stent in a realistic coronary artery--Determination of the optimum modelling strategy. J. Biomech. 43, 2126–2132.

Zainal Abidin, N.I., Rolfe, B., Owen, H., Malisano, J., Martin, D., Hofstetter, J., Uggowitzer, P.J., Atrens, A., 2013. The in vivo and in vitro corrosion of high-purity magnesium and magnesium alloys WZ21 and AZ91. Corros. Sci. 75, 354–366. doi:10.1016/j.corsci.2013.06.019

Zeng, R., Dietzel, W., Witte, F., Hort, N., Blawert, C., 2008. Progress and Challenge for Magnesium Alloys as Biomaterials. Adv. Eng. Mater. 10, B3–B14. doi:10.1002/adem.200800035

Zeng, R., Zhang, J., Huang, W., Dietzel, W., 2006. Review of studies on corrosion of magnesium alloys. Trans. Nonferrous Met. Soc. China 16, 763–771.

Zhang, J., Niu, X., Qiu, X., Liu, K., Nan, C., Tang, D., Meng, J., 2009. Effect of yttrium-rich misch metal on the microstructures, mechanical properties and corrosion behavior of die cast AZ91 alloy. J. Alloys Compd. 471, 322–330. doi:10.1016/j.jallcom.2008.03.089

Zhang, S., Zhang, X., Zhao, C., Li, J., Song, Y., Xie, C., Tao, H., Zhang, Y., He, Y., Jiang, Y., Bian, Y., 2010. Research on an Mg-Zn alloy as a degradable biomaterial. Acta Biomater. 6, 626–40. doi:10.1016/j.actbio.2009.06.028

Zhang, X., Yuan, G., Mao, L., Niu, J., Ding, W., 2012. Biocorrosion properties of as-extruded Mg–Nd–Zn–Zr alloy compared with commercial AZ31 and WE43 alloys. Mater. Lett. 66, 209–211. doi:10.1016/j.matlet.2011.08.079

Zhang, Y., Bourantas, C. V, Farooq, V., Muramatsu, T., Diletti, R., Onuma, Y., Garcia-Garcia, H.M., Serruys, P.W., 2013. Bioresorbable scaffolds in the treatment of coronary artery disease. Med. Devices (Auckl). 6, 37–48. doi:10.2147/MDER.S22547

Zhao, H.D., Qin, G.W., Ren, Y.P., Pei, W.L., Chen, D., Guo, Y., 2011. The maximum solubility of Y in α-Mg and composition ranges of Mg24Y5−x and Mg2Y1−x intermetallic phases in Mg–Y binary system. J. Alloys Compd. 509, 627–631. doi:10.1016/j.jallcom.2010.09.120

Zhao, M.-C., Liu, M., Song, G.-L., Atrens, A., 2008. Influence of pH and chloride ion concentration on the corrosion of Mg alloy ZE41. Corros. Sci. 50, 3168–3178.

Zheng, Y.F., Gu, X.N., Witte, F., 2014. Biodegradable metals. Mater. Sci. Eng. R Reports 77, 1–34. doi:10.1016/j.mser.2014.01.001

Zhou, W., Shan, D., Han, E.-H., Ke, W., 2008. Structure and formation mechanism of phosphate conversion coating on die-cast AZ91D magnesium alloy. Corros. Sci. 50, 329–337. doi:10.1016/j.corsci.2007.08.007

Zhou, W.R., Zheng, Y.F., Leeflang, M. a, Zhou, J., 2013. Mechanical property, biocorrosion and in vitro biocompatibility evaluations of Mg-Li-(Al)-(RE) alloys for future cardiovascular stent application. Acta Biomater. 1–11. doi:10.1016/j.actbio.2013.01.032

Zohdi, T.I., Holzapfel, G. a, Berger, S. a, 2004. A phenomenological model for atherosclerotic plaque growth and rupture. J. Theor. Biol. 227, 437–43. doi:10.1016/j.jtbi.2003.11.025

Zorion Medical, 2014. ZMED Device Information [WWW Document]. URL http://www.zorionmedical.com/ (accessed 7.10.13).

Appendix A

A.1 Compositional analysis

Three specimens (n=3) of the WE43 precursor tube were acid digested using a Milestone Microwave Digestion System and analysed using Inductively Coupled Plasma Mass Spectrometry (ICP-MS) (7500 ICP-MS, Agilent Technologies) in order to determine the compositional content of magnesium and the three main alloying elements (Y, Zr & Nd). The weight % of magnesium and the alloying elements was found to be consistent with that specified by the manufacturer of WE43 (Magnesium Elektron, 2007), as shown in Table A.1.

Element	Mg	Y	Zr	Nd
Weight %	92.8	4.0	0.7	2.3

Table A.1 Elemental composition (average weight %) of WE43 tube specimen determined by ICP-MS

A.2 Additional Data from Corrosion Experiment A
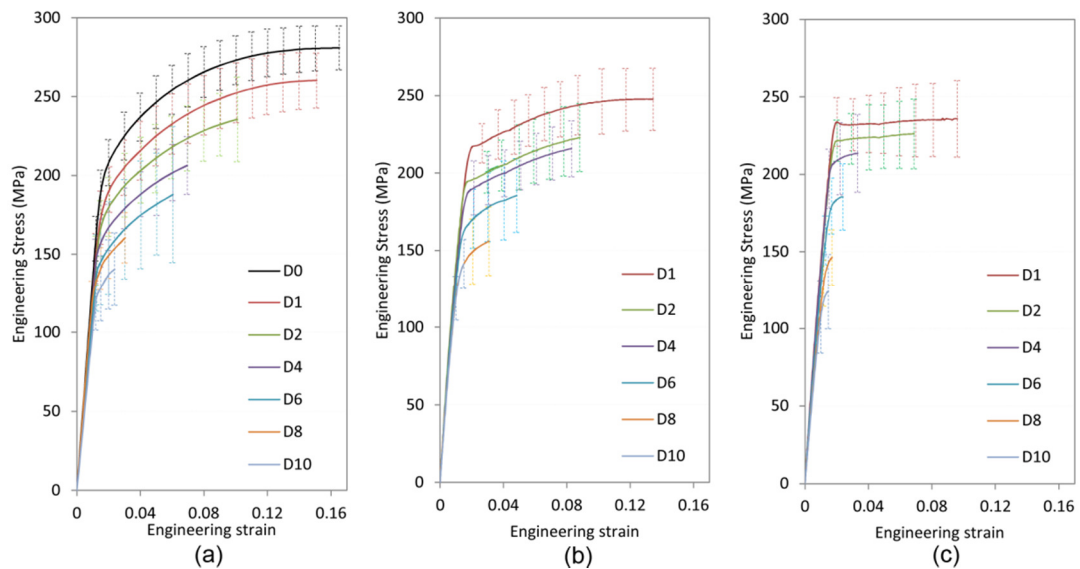
Figure A.1 Stress-strain curves (terminating at the UTS) for dogbone specimens based on the results of experiment A, (a) 0% PS (b) 2.7% PS and (c) 8.4% PS. Error bars represent 95% confidence intervals derived from T-table.

A.3 APDL Implementation of Corrosion Model

```
!====================================================================
!----- Plastic strain-mediated corrosion algorithm V5.1 -----------
!----- Written by: Emmet Galvin, Date: 10/07/14 --------------------
!----- All text to the right of "!" are comments -----------------------
!====================================================================

!-------------- Set control parameters for corrosion algorithm ----------------------
finish
/prep7                                  ! Enter preprocessor
k_U=8.1667e-3                           ! Corrosion kinetic parameter (hr^-1)
Delta_t=1                               ! Time step (hr)
tMax=60                                 ! Maximum solution time (hr)
ItNum=tMax/Delta_t+1                    ! Set number of iterations
ItNum=nint(ItNum)                       ! Find nearest integer value of ItNum
INL=ItNum+1
delta_U=0.015                           ! Material characteristic length (mm)
DeDt=delta_U*k_U*Delta_t

esel,s,type,,1
*get,J,elem,,count                      ! Get the number of elements (J) in
esel,all                                ! the selected set

!-------------- Create element characteristic length (L_e) array --------------------
*del,L_e
*dim,L_e,array,J                        ! Create array for L_e
*do,EE,1,J
        *get,V_e,elem,EE,volu           ! Get element volume
        L_e(EE)=(V_e)**(1/3)            ! Get L_e and write
*enddo                                  ! to L_e array

!-------------- Create damage (D) array ----------------------------------------------
*del,De1
*dim,De1,array,J,INL                    ! Create array for De1
*do,EE,1,J
        De1(EE,1)=0                     ! Initialise damage parameter
        De1(EE,2)=0
*enddo

!-------------- Create results array -------------------------------------------------
*del,MML
*dim,MML,array,INL,4                    ! Create results array
MML(1,1)=0                              ! Iteration number
MML(1,2)=0                              ! Solution time (hr)
MML(1,3)=J                              ! Number of live elements
MML(1,4)=0                              ! Model mass loss(%) from DES

!-------------- Create K array -------------------------------------------------------
*del,K
*dim,K,array,J,9                        ! K (no. of exposed element faces) array

*do,EE,1,J
        *do,xx,1,9
                K(EE,xx)=0              ! Initialise K parameter
        *enddo
*enddo

esel,s,,,allbcelem
```

```
*get,J3,elem,0,count
i=0
xx=1
*do,xx,1,J3
        ff=elnext(i)
        K(ff,7)=1                               ! Set K(ff,7)=1 for elements
        i=ff                                    ! on symmetry edges
*enddo
alls

!-------------- Create current element strain (CES) array --------------------------
*del,CES
*dim,CES,array,J
*do,EE,1,J
        CES(EE)=0                               ! CES array records element first
*enddo                                          ! principal plastic strain

!-------------- Create DES (current Element Damage) array ----------------------
*del,DES
*dim,DES,array,J                                ! DES array records element damage (D)
*do,EE,1,J
        DES(EE)=0
*enddo

!-------------- Create recent death (RDM) array ----------------------------------------
*del,RDM
*dim,RDM,array,J,INL                            ! RDM array records element death

*do,EE,1,J
        *do,zz,1,INL
                RDM(EE,zz)=0
        *enddo
*enddo

!-------------- Create material model number (MMN) array -----------------------
*del,MMN
*dim,MMN,array,J
*do,EE,1,J
        MMN(EE)=1                               ! Set initial material model
*enddo                                          ! for all elements to 1
alls

!-------------- Create plastic strain parameter (Phi) array ------------------------
!-------------- to scale DeDt based on current element strain (CES) ------------
*DIM,mult1,TABLE,6,6,1, , ,
*TAXIS,mult1(1,1,,),,  0,0.027,0.084,0.12,0.168,0.35       ! Plastic strain
*TAXIS,mult1(1,1,,),2,24,48,96,144,192,240                ! Time (hr)
mult1(1,1)=0.368, 2.190, 5.830, 25.00, 70.00, 700.0
mult1(1,2)=1.287, 1.265, 1.264, 6.000, 12.00, 20.00
mult1(1,3)=1.000, 0.632, 0.630, 1.500, 2.000, 3.000
mult1(1,4)=1.035, 1.092, 1.149, 1.150, 1.250, 1.350
mult1(1,5)=0.862, 1.149, 1.093, 1.093, 1.093, 1.093
mult1(1,6)=0.785, 1.095, 1.483, 1.800, 2.000, 2.200

!-------------- Simulate Stent Deployment & Recoil ----------------------------------
finish                                          ! Finish preprocessor
/solu                                           ! Enter solution
nlgeom,on                                       ! Activate large deformation controls
solcon,on                                       ! Activate solution controls
```

```
sf,stentinner,pres,0.95                ! Simulate stent expansion
nsubst,50,100,20
outres,all,last
time,0.9
solve

sf,stentinner,pres,0                   ! Simulate stent elastic recoil
nsubst,20,20,20
outres,all,all
time,1.0
solve


!--------------- Update CES array -----------------------------------------------
finish                                 ! Finish solution
/post1                                 ! Enter postprocessor
etable,epl,eppl,1                      ! create etable 'epl' of first
*do,EE,1,J                             ! principal plastic strain
        *get,pps,elem,EE,etab,epl
        CES(EE)=pps                    ! update CES array
*enddo

I=2
parsav, all, params1, ,                ! Save scalar parameters to text file
parsav,scalar,scalparams,,

finish
/solu
antype,,restart,,,continue            ! CES data is lost after restart so
parres, new, params1,,                 ! must read from text file
parres, change, scalparams,,
nsubst,1,1,1
outres,all,last,                       ! Save last result set only
alls
save

!--------------- Corrosion Algorithm Iterative cycle ----------------------------------
*do,I,2,ItNum                          ! I varies from 2 to ItNum

        CT=I-1                         ! Corrosion Time (hr)
        /gopr                          ! Reactivate suppressed printout

        ST=Delta_t*(CT)                        ! Solution Time (hr)
        *if,ST,ge,0,and,ST,le,24,then          ! y mediates mult1 array column
        y=24                                   ! selection
        *elseif,ST,gt,24,and,ST,le,48,then
        y=48
        *elseif,ST,gt,48,and,ST,le,96,then
        y=96
        *elseif,ST,gt,96,and,ST,le,144,then
        y=144
        *elseif,ST,gt,144,and,ST,le,192,then
        y=192
        *elseif,ST,gt,192,and,ST,le,240,then
        y=240
        *endif

        !--------------- Update Ke array -----------------------------------------
        esel,s,live                    ! Select live elements
        esel,r,type,,1
```

```
        *do,EE,1,J                              ! Find number of neighbouring elements
                *do,fn,1,6
                        *if,eladj(EE,fn),lt,1,then
                                K(EE,fn)=0
                        *else
                                *get,ELS1,elem,eladj(EE,fn),attr,live
                                  *if,eladj(EE,fn),ge,1,and,ELS1,eq,1,then
                                                K(EE,fn)=1
                                        *else
                                                K(EE,fn)=0
                                        *endif
                        *endif
                *enddo

K(EE,8)=6-(K(EE,1)+K(EE,2)+K(EE,3)+K(EE,4)+K(EE,5)+K(EE,6)+K(EE,7))
                                        ! K(EE,8)= number of exposed elem faces
                *if,K(EE,8),eq,0,then      ! Set Ke parameter based on K(EE,8)
                        K(EE,9)=0.000
                *elseif,K(EE,8),eq,1,then
                        K(EE,9)=1.000
                *elseif,K(EE,8),eq,2,then
                        K(EE,9)=1.289
                *elseif,K(EE,8),eq,3,then
                        K(EE,9)=2.182
                *elseif,K(EE,8),eq,4,then
                        K(EE,9)=2.667
                *elseif,K(EE,8),eq,5,then
                        K(EE,9)=2.805
                *elseif,K(EE,8),eq,6,then
                        K(EE,9)=2.949
                *endif
        *enddo

        !--------------- Corrosion process-------------------------------------------
        esel,s,live
        esel,r,type,,1
        nsle,r
        nsel,r,ext
        nsel,u,,,allbcnode
        esln,r                                    ! Select external elems for corrosion

        *do,EE,1,J
                *get,ESS,elem,EE,esel          ! Get elem selection status (ESS)

                *if,ESS,eq,1,then
                        *get,ELS,elem,EE,attr,live        ! Element life status
                *endif


                *if,ESS,eq,1,and,ELS,eq,1,then
                        Phi=mult1(CES(EE),y)            ! Set Phi from mult1 array
                        De1(EE,I)=De1(EE,I-1)+((DeDt*Phi*K(EE,9))/L_e(EE))
                *else
                        De1(EE,I)=De1(EE,I-1)
                *endif

                !------- Change material model number or kill element ------
                *if,De1(EE,I),ge,0,and,De1(EE,I),le,0.1,then
                                /wait,0
                        *elseif,De1(EE,I),ge,0.1,and,De1(EE,I),lt,0.2,then
```

```
                        MPCHG,2,EE
              *elseif,De1(EE,I),ge,0.2,and,De1(EE,I),lt,0.3,then
                        MPCHG,3,EE
              *elseif,De1(EE,I),ge,0.3,and,De1(EE,I),lt,0.4,then
                        MPCHG,4,EE
              *elseif,De1(EE,I),ge,0.4,and,De1(EE,I),lt,0.5,then
                        MPCHG,5,EE
              *elseif,De1(EE,I),ge,0.5,and,De1(EE,I),lt,0.6,then
                        MPCHG,6,EE
              *elseif,De1(EE,I),ge,0.6,and,De1(EE,I),lt,0.7,then
                        MPCHG,7,EE
              *elseif,De1(EE,I),ge,0.7,and,De1(EE,I),lt,0.8,then
                        MPCHG,8,EE
              *elseif,De1(EE,I),ge,0.8,and,De1(EE,I),lt,0.9,then
                        MPCHG,9,EE
              *elseif,De1(EE,I),ge,0.9,and,De1(EE,I),lt,0.999,then
                        MPCHG,10,EE
              *elseif,De1(EE,I),ge,0.999,then
                        De1(EE,I)=1
                        ekill,EE         ! If D>1 then kill element
                        RDM(EE,I)=1      ! Record element death in RDM array
        *endif

        DES(EE)=De1(EE,I)                ! Update DES array for mass loss
*enddo                                   ! calculation


!-------------- Update Results Array -------------------------------------------------
esel,s,live
esel,r,type,,1
*get,NoE,elem,0,count                    ! Get the number of live elements
*vscfun,DESSUM,sum,DES(1)   ! Sum Damage (D) for all elements

MML(I,1)=CT                              ! Iteration
MML(I,2)=Delta_t*(CT)                    ! Solution time (hr)
MML(I,3)=NoE                             ! Number of live elements
MML(I,4)=100*(DESSUM/J)                  ! % Mass loss based on D

solve                                    ! *** SOLVE ***
save

finish                                   ! Finish solution
/post1                                   ! Enter postprocessor
set,last
rsys,1                                   ! Cylindrical results co-ord system


!-------------- Update CES array -------------------------------------------
esel,s,type,,1
etable,eps,eppl,1                        ! Set up etable 'eps' for
*do,EE,1,J                               ! 1st principal plastic strain
        *get,pps,elem,EE,etab,eps        ! Write plastic strains to CES
CES(EE)=pps                              ! array
*enddo


!-------------- Update MMN array -------------------------------------------
*do,EE,1,J
*get, EMMN, elem, EE, attr, mat
        MMN(EE)=EMMN
*enddo


!-------------- Get stent outer diameter --------------------------------------
```

```
            cmsel,s,stentouter
            nsort,u,x
            *get,uxmax%I%,sort, ,max
            alls


            !--------------- Corrosion plot----------------------------------------------------
            esel,s,type,,1
            /cont,1,20,0,0.1,1                          ! Set values for contour plot
            etable,CVPH,s,x                             ! Set sx as corrosion value
            *vput,De1(1,I),elem,1,etab,CVPH             ! placeholder
            esel,s,live                                  ! Select live elements
            esel,r,type,,1
            /efacet,1
            /title,Corrosion %MML(I,2)%[hr] (Delta_t=%Delta_t%[hr])
            pletab,CVPH                                 ! Plot element table
            /view,1,1,1,1
            /ang,1
            /auto,1
            /rep,fast
            /input,0plots,txt
            alls

            parsav, all, params%I%, ,                   ! Save scalar parameters
            finish
            /solu

            antype,,restart,,,continue                  ! Restart analysis
            parres, new, scalparams,,                   ! Read scalar parameters
            parres, new, params%I%, ,

            *do,EE,1,J
                    *if,RDM(EE,I),eq,1,then             ! Remove killed elements
                            ekill,EE
                    *endif
            *enddo

            I=I+1
            parsav, all, params%I%, ,                   ! Save scalar parameters
            parsav,scalar,scalparams,,
*enddo

*mwrite,MML,filenam1,tsv,,jik,5,ItNum,1                 ! Write results to .tsv file
(5F12.6)

*msg,ui
**Solution completed**                                 ! Send message to GUI
finish
/out                                                    ! Alert user by email
/mail, --,emmet.galvin3@mail.dcu.ie,0plots,txt
finish
/eof                                                    ! End of file
```

A.4 Corrosion Model Convergence Studies

A.4.1 Dogbone Specimen Model

Owing to the simplicity of the dogbone specimen model geometry and the deformation induced by the uniaxial load, it was found that the predicted nodal displacement, element stress and element strain results were all converged even when a relatively large L_e was used. Therefore, a mesh sensitivity study was performed, as shown in Figure A.2(a), in which the predicted mass loss results were converged to within approximately 3% when using $L_e = 0.012$ mm. Using this L_e value, a suitable time step of 1 hour was identified in a similar iterative process, as shown in Figure A.2(b).
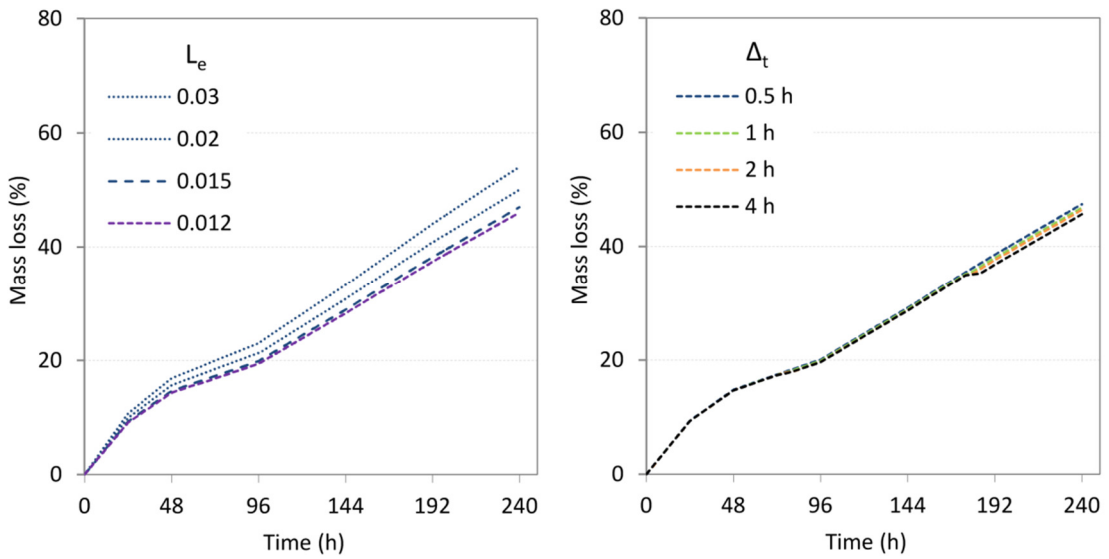

Figure A.2 (a) Plot of predicted dogbone specimen mass loss over time for varying average element size (L_e) values, (b) Plot of predicted dogbone specimen mass loss over time for varying time step (Δ_t) values

A.4.2 Stent Model

For the RUC stent model, predicted nodal displacement, element stress and strain and radial stiffness results were all found to have converged within 2% when using

$L_e = 0.015$. Therefore, based on the results of the convergence study shown in Figure A.3, L_e and Δ_t values of 0.012 mm and 1 hour were selected, respectively.

Figure A.3 (a) Plot of predicted stent mass loss over time for varying average element size (L_e) values, (b) Plot of predicted stent mass loss over time for varying time step (Δ_t) values